Een generiek proces voor impregnatie en additieve productie
van continuvezelversterkte thermoplastische composieten

A Generic Process for Impregnation and Additive Manufacturing
of Endless Fibre-Reinforced Thermoplastic Composites

Willem Van De Steene

Promotoren: prof. dr. ing. L. Cardon, prof. dr. ing. K. Ragaert
Proefschrift ingediend tot het behalen van de graad van
Doctor in de industriële wetenschappen: elektromechanica

UNIVERSITEIT
GENT

Vakgroep Materialen, Textiel en Chemische Proceskunde
Voorzitter: prof. dr. P. Kiekens
Faculteit Ingenieurswetenschappen en Architectuur
Academiejaar 2019 - 2020

ISBN 978-94-6355-374-2
NUR 971, 978
Wettelijk depot: D/2020/10.500/51

PROMOTORS

Prof. dr. ing. Ludwig Cardon
Ghent University
Faculty of Engineering and Architecture
Department of Materials, Textiles and Chemical Engineering

Prof. dr. ing. Kim Ragaert
Ghent University
Faculty of Engineering and Architecture
Department of Materials, Textiles and Chemical Engineering

EXAMINATION COMMITTEE

Prof. Luc Taerwe	(chair)	Ghent University, Belgium
Prof. Gerald Pinter		Montanuniversität Leoben, Austria
Prof. Peter Ragaert		Ghent University, Belgium
Prof. Paul Van Steenberge	(secretary)	Ghent University, Belgium
Prof. Dagmar D'hooge		Ghent University, Belgium
Prof. Kim Ragaert	(promotor)	Ghent University, Belgium
Prof. Ludwig Cardon	(promotor)	Ghent University, Belgium

RESEARCH INSTITUTE

Ghent University
Department of Materials, Textiles and Chemical Engineering
Tech Lane Ghent Science Park - Campus A
Technologiepark 130
B-9052 Zwijnaarde
Willem.vandesteene@ugent.be

ACKNOWLEDGEMENTS

About six years ago we boarded a ship to make this Odyssean journey, there was only one certainty: we had no idea where all our wanderings would bring us. We crossed oceans, stranded on inhabitable and deserted lands, lost a couple of souls deep in the water, were rammed by technical challenges, committed a healthy dose of mutiny, but above all, discovered some breath-taking pearly white beaches, smelling like fresh coconut water and the finest golden rum.

Captain professor Ludwig Cardon gathered himself a good crew on his ship, allowing him to plough through the water faster and faster, never forgetting he started his own career as a common sailor too, paddling against the tide. As it befits a good captain, Ludwig puts his faith in the people surrounding him, instead of threatening to keelhaul them. Always being creative coping with his rationed supply of gold, Ludwig succeeds in giving his crew the right oars to row together towards the rising sun. Putting the spin-off jokes and 'patent-pendingness' aside (some of them became - against all odds - reality), he was the captain that sailed me towards Athens (GR), Bologna (I), Birmingham (GB), Bradford (GB), Chengdu (CN), Dresden (DE), Düsseldorf (DE), Eindhoven (NL), Ghent (B), Guimarães (PT), Izmir (TR), London (GB), Marseille (F), Porto (PT), Serraing (B), Stade (DE) and Veldhoven (NL), which allowed me to disseminate and valorise the knowledge we created.

In nautical legends it is described that having a woman on board of a ship, other than the bare-chested figurehead on its prow, brings misfortune and despair. However, this myth can now be debunked for good. Due to the clear view of first navigator professor Kim Ragaert we avoided ice bergs and violent weather during our journey, her compass always pinpointing the exact direction to go, pursuing accurate and useful science. To the people ashore, Kim is mostly seen as determined, strict and focused, which is true, and those characteristics are the perfect things to have in a navigator. To her peers, Kim

turns out to be an extraordinary righteous and empathic person, willing to fight for the well-being of her cubs. That is why I felt extremely honoured when tensile testing goddess Kim proposed to co-author a book on material sciences together with her and Laurens. Of the record, Kim: I left a double space somewhere in this manuscript, you will know what to do now…

Together with us, boatswain professor Joris Degrieck embarked the ship, and gave us exquisite sails to catch the inspiration we needed to keep us propelled. Joris always succeeds in inciting people's creativity with his untempered enthusiasm, so it was a sad day when we had to leave you behind in a French harbour amidst our journey. However, I am sure your stream of thought will hit like a tsunami when you read this manuscript, thinking of possible applications for our research.

Joris worked in symbiosis with dr. Ives De Baere, our boatsman, who is always prepared to roll up his sleeves to hoist some sails and lift the heavy anchors. I thank you for your insights in composite testing the way you prefer it: concise and straightforward.

I feel the time has come to put an end to this ridiculous and far-stretched 'adventurous explorer' analogy, so allow me to continue my narrative with a Latin quote, as it behoves archaic ivory tower academics and dusty politicians who claim to have made a somewhat (or seemingly) important contribution to the prosperity of humankind. Once an erudite old man told me the phrase *"Amore, more, ore, res, nascuntur amicitiae"*, which paraphrases into *"through all the things you do and experience with the people surrounding you, a friendship sprouts"*. And that is exactly what happened with my colleagues in Zwijnaarde Technology Park, with whom I found myself not only collaborating but also barbecuing, winning the Ghent University football competition (hail FC Plastiek!), playing Highland games, organising a beer pong contest, getting to the final of Solvay Additive Manufacturing Cup 218 and 2019, doing awkward dances when no students were around, playing board games and tasting whiskey, and all that even during holidays (and nights), when there

was no obligatory reason whatsoever to spend our free time together. Special thanks to Amir, Andrea, Assia, Astrid, Dahang, Daniel, Dashan, Ellen², Els, Flavio, Gianni, Ives, Joachim, Karen, Kerstin, Kim, Kurt, Laurens, Line, Lingyan, Ludwig, Maja, Marcel, Marie, Martin, Mustafa, Nan, Nicolas², Pascal, Ruben², Rudinei, Sara, Sisi, Stefaan, Tom², Veerle, Wim and Zhenmin.

Warm regards to my close colleagues of campus Schoonmeersen: Anthony, Antoine, Bart, Charles, Frank, Geert, Gieljan, Guy, Hicham, Ingrid, Jan², Jens, Kathleen, Katrien, Leen, Marc, Nele, Peter, Ruddy, Tim, Tom,… , to former thesis students Anton, Arne, Axel, Baptiste, Henri, Jan, Jasper, Jelle, Josef, Olivier, Robin, Sanne, Tom, Wesley and all other 1573 students I tutored so far at Ghent University.

From a financial perspective, I am extremely grateful to Ghent University for having made this research possible, as well as to all companies that contributed and/or showed their interest. I cannot mention you all, but you know who you are, cheers! To the consortium members of the European Project 'Repair3D': it is an honour to collaborate with you and to hear your vision on additive manufacturing, repurposing and upcycling of composites. Special thanks to our academic partners Bradford University, Montanuniversität Leoben, Sichuan University and University of Minho, especially to Phil, Michael, Clemens, Martin and Jose for your hospitality and your interest in our research.

To my fellow high school friends Alexandra, Aurelia, Elisa, Gilles, Jan-Frederik, Joachim, Jonas, Kevin, Klaas, Lara, Lennart, Linde, Marieke, Mariolein, Marjolein, Michiel, Nicky, Steffen, Tom, Wout, etc.: thank you for walking this walk together with me. Alex, remember the days we were those odd, insecure teens… But hey, look at us now! Thank you Ann-Sophie, Ben, Bram², Bruno, David, Hélène, Jelle, Jolien, Kenny, Jorge², Lynn, Michiel, Nick, Niels, Soraya, Stefaan, Theresa, Tom³, Yoshi, and others for those epic student dorm get togethers, pizza nights and spare rib sessions during and after our Industrial

Engineering studies. Warm regards to my ice cream parlour friends in Westende: Ian, Jasper, Karel, Laura and Pierre.

Many thanks to Verkeerd Geparkeerd and its diverse spectrum of members, giving the world that extra bit of colour it desperately needs. Aäron, Bart, Cedric, Femke, Gijs, Ilias, Jan, Joakim, Jonathan, Kevin, Lorenzo², Marieke, Michiel, Rani, Thibaut, Valérie, Wouter, Yoram,... we were not only volunteers working together, we also cheered, cried and lived together, grew up and became assertive, critically thinking and proud people, wanting to make and - without any doubt - have made a difference. Also you were always there: Adriano, Addie, Andreas, Ben, Clément, Django, Dorina, Hannes, Ineke, Jan, Jens, Jonathan, Koen², Laure, Lieven³, Mattijs, Matthias, Nico, Rosalie, Simon, Vik, etc.

Lots of love and roars to my fellow Roundabout 30 tigers and friends Benjamin, Evy, Gertjan, Kim, Koenraad, Laurens, Leen, Lore, Michiel, Quinten, Sofie and others. On to the next ten years? Shout-out to Arlena, Dries, Fleur, Ismien, Jens, Judith, Jurgen, Michiel, Neji, Sammy, Sem, Sophie, Sven and friends from Casa Rosa, çavaria and WJNH. It must have been 8 years ago since I started volunteering in your communication team or doing bar shifts during Gentse Feesten. Without any doubt: you give me more energy than any power plant can provide.

Aäron, Alexandra, Arno, Bart, Cedric, David, Diego, Jan, Jolien, Marieke, Rosalie, Thomas and Vincent, it was impossible to fit you into just one of the above categories, probably because our lives are or were intertwined at a certain point of time, we have travelled the same route or we just get along quite well. Together we discussed our darkest secrets and if I would go on a trip to conquer the world, I would love to have you by my side. I remember us discovering Amsterdam, London, Madrid, Prague, etc., cooking together, our Monday night sports sessions, the numerous pizza nights, the cappuccino moments, those cosy times at Lokerse Feesten, the ukulele sessions and midnight drinks in Baudeloo Park or on Graslei, and our domination of Plansjee's dance floor. Lots of thanks to my (former) housemates Alexander,

Fien, Leen, Lore and Marijn, who could handle living with me and dealing with my - sometimes unconventional - schedules. I will always remember us having drinks at the campfire, barbecuing and organising Christmas parties.

Finally, I would like to thank my parents, Karel, Valérie and the rest of my family for their unconditional love and support. You helped making me, layer-by-layer, the person I am today.

Willem
6 December 2019

LIST OF PUBLICATIONS

A1

An evaluation of three different techniques for melt impregnation of glass fiber bundles with polyamide 12, Willem Van De Steene, Jan Verstockt, Joris Degrieck, Kim Ragaert and Ludwig Cardon, (2018) Polymer Engineering and Science. 58(4). p.601-608.

Mechanical properties of polymeric implant materials produced by extrusion-based additive manufacturing, Florian Arbeiter, Sandra Petersmann, Martin Spoerk, Willem Van de Steene, Muammer Uecal, Johannes Wiener, Gerald Pinter, (2020), Journal of the Mechanical Behavior of Biomedical Materials. 104. 103611.

Influence of machine type and consecutive closed-loop recycling on macroscopic properties for fused filament fabrication of acrylonitrile-butadyene-styrene parts, Pierandrea Dal Fabbro, Andrea La Gala, Willem Van De Steene, Dagmar R. D'hooge, Giovanni Lucchetta, Ludwig Cardon, Rudinei Fiorio, (submitted, 2020), Rapid Prototyping Journal.

Patents

WO 2019/141606 A1, An extruder with axial displacement, Ludwig Cardon, Dagmar D'hooge, Kim Ragaert, Willem Van De Steene, Mustafa Erkoç, Marcel Moerman, (2019) World Intellectual Property Organisation.

B1

Materialen. Basis materiaalkunde voor ingenieurs, Kim Ragaert, Willem Van De Steene, Laurens Delva, (under review) Acco, Leuven, Belgium.

C1

Process development of continuous fiber additive manufacturing with in-line impregnated thermoplastic composites, Willem Van De Steene, Kim Ragaert, Jozef Martens and Ludwig Cardon, (2018) International Conference on Polymers and Moulds Innovations - PMI 2018, Guimarães, Portugal.

Methodology for Continuous Fibre Additive Manufacturing with In-Line Impregnated Thermoplastic Composites, Willem Van De Steene, Tom Van Waeleghem, Kim Ragaert, Ludwig Cardon, (2019) Autex 2019: Conference proceedings, Ghent, Belgium.

Use of an active impregnation pin in a polyamide 12 melt impregnation process for continuous glass fibre bundles, Willem Van De Steene, Jan Verstockt, Joris Degrieck , Kim Ragaert and Ludwig Cardon, (2016) PMI 2016: Conference proceedings. p.34-39, Ghent, Belgium.

C3

3D printed CFRPs and micro-composite products by design from recycled resources, Tanja Kosanovic Milickovic, Willem Van De Steene, Ludwig Cardon, Costas Charitidis, (2019) EASN conference, Abstracts p.214-215, Athens, Greece.

Additively manufactured continuous fibre composites, really taking off? Willem Van De Steene, Tom Van Waeleghem, Kim Ragaert and Ludwig Cardon, (2019) FEARS 2019 : book of abstracts. p.136-137, Ghent, Belgium.

A novel process for tailored stiffness and strength in extrusion-based additive manufacturing, Willem Van De Steene, Kim Ragaert and Ludwig Cardon, (2017) Proceedings of the 2017 Polymer Processing Society Europe Africa Conference. p.11-11, Dresden, Germany.

Composite processing through extrusion-based additive manufacturing, Willem Van De Steene, Joris Degrieck, Kim Ragaert, Ludwig Cardon, (2014) FEA Research Symposium 2014, Ghent, Belgium.

Continuous fibre additive manufacturing with in-line impregnated thermoplastic composites, Willem Van De Steene, Kim Ragaert, Ludwig Cardon, (2018) International symposium Hybrid Additive Manufacturing with Polymers, Centexbel, Ghent, Belgium.

Experimental and numerical optimization of processing parameters for hybrid injection moulds, Willem Van De Steene, Stef Boden, Tom Wieme and Ludwig Cardon, (2019) International SimaTec Usermeeting 2019 : presentations, Düsseldorf, Germany.

Future perspectives of (continuous fibre reinforced) composite additive manufacturing, Willem Van De Steene, Tom Van Waeleghem, Sisi Wang, Dagmar D'Hooge and Ludwig Cardon, (2019) 11th UK-China AMRI Research Workshop, Abstract book. p. F17-F17.

Optimisation of a continuous fibre reinforced additive manufacturing process, Willem Van De Steene, Kim Rageart, Ludwig Cardon, (2019), International Conference of the Polymer Processing Society, Izmir, Turkey.

Optimisation of interlayer cohesion in additively manufactured continuous fibre composites, Willem Van De Steene, Tom Van Waeleghem, Kim Ragaert, Ludwig Cardon, (2019) PPE 2019, Bradford, United Kingdom.

Thermoplastic composites: glass fibre bundle impregnation modelling, Willem Van De Steene (UGent) , Joris Degrieck , Kim Ragaert and Ludwig Cardon, (2015) FEA Research Symposium 2015, Abstracts. p.1-1, Ghent, Belgium.

LIST OF SYMBOLS AND ABBREVIATIONS

ABS	Acrylonitrile butadiene styrene
AFP	Automated fibre placement
AM	Additive manufacturing
ATL	Automated tape laying
a_1	Maximal acceleration of the composite strand
α	Angular acceleration of the puller wheel, contact angle
α_i	Contact angle of spreader pin i
α_X	Contact angle, measured from 0 to location X
c	Coefficient of rolling friction between puller wheels and composite strand
c_{cb}	Cubic packing correction factor
c_{hcp}	Hexagonal close packed correction factor
c_i	Correction factor i
C_i	Integration constant
CFD	Computational fluid dynamics
CNT	Carbon nanotubes
d_b	Equivalent bearing diameter
d_d	Diameter of a pultrusion die

d_f	Average diameter of a single fibre
d_i	Fibre inlet diameter
$d_{i,min}$	Minimal fibre inlet diameter
$d_{i,j}$	Inter-fibre distance between fibre i and fibre j
$\frac{dP}{dx}$	Pressure gradient in direction x
$\frac{du}{dy}$	(Average) shear rate
d_w	Pultrusion wheel diameter
d_2	Diameter of the deposition nozzle
D_i	Degree of impregnation
DSC	Differential scanning calorimetry
DMA	Dynamic mechanical analysis
EAM	Extrusion-based additive manufacturing
ECR-glass	Glass fibre with electrical/chemical resistance
EFAM	Endless fibre additive manufacturing
E	Young's modulus/ activation energy
E_f	Young's modulus of a fibre material
E_{flex}	Flexural modulus
E''	Loss modulus
ε_{flex}	Strain at flexural strength

η	Apparent/dynamic viscosity of a fluid
η_{tr}	Efficiency of the drive train
η_0	Dynamic viscosity of a fluid, measured at T_0
η_1	Dynamic viscosity of a fluid, measured at T_1
$f_{b,s}$	Equivalent dynamic coefficient of friction of the pultrusion wheel bearings
$f_{c,w}$	Dynamic coefficient of friction between the composite strand and puller wheels
FEAM	Fiber encapsulation additive manufacturing
FEA	Finite element analysis
FFF	Fused filament fabrication
FDM	Fused deposition modeling
f or f_i	Dynamic friction coefficient
F	Fibre bundle tension
F_c	Clamping force
F_{cent}	Centrifugal force
$F_{d,i}$	Drag force number i
F_f	Frictional force
F_{fl}	Force resulting in a flexural stress
F_i	Tensile force number i

F_N	Normal force
$F_{pul,N}$	Pultrusion force for a N-pin impregnation system
F_t	Force resulting in a tensile stress
F_X	Tensile force at location X
GPC	Gel permeation chromatography
$G_{1,2}, G_{1,3}$	Shear moduli in a plane parallel to fibre direction in a uniaxially reinforced composite
h	Thickness of a thin layer of material
I_f	Second moment of inertia of the fibre cross-section
J	Moment of inertia of all rotating components in the EFAM system, reduced to the puller wheel shaft
k	Consistency index/ Kozeny constant
K	Darcy permeability
K_0	Shape factor of a fibre bed
K_l	Tortuosity of a fibre structure
l	Length
l_c	Critical fibre length
l_f	Fibre length
l_i	Fibre inlet length
L	Distance

L_e	Effective fluid travel length
m	Total mass of the linearly accelerating objects
m_c	Mass of a composite material in a composite
m_f	Mass of a fibre material in a composite
m_i	Mass of a component i in a composite
m_m	Mass of a matrix material in a composite
m_v	Mass of the voids in a composite
M_f	Mass fraction of fibres in a composite
MFI	Melt flow index
M_{fl}	Bending moment
$M_{fl,max}$	Maximal bending moment
M_i	Mass fraction of component i in a composite
M_m	Mass fraction of matrix in a composite
$M_{m,max}$	Maximum obtainable matrix mass fraction in a composite
M_v	Mass fraction of voids in a composite
μ_d	Dynamic friction coefficient
n	Flow behaviour index
N	Amount of specimens
N_f	Fibre count
p_X	Pressure at location x

p_0	Externally applied pressure
PA6	Polyamide 6
PA12	Polyamide 12
PEEK	Polyether ether ketone
PEI	Polyetherimide
PET-G	Polyethylene terephthalate, glycol-modified
PI	Polyimide
PLA	Polylactic acid
P_{min}	Minimal required power
φ_i	Polar angle of fibre i
φ_j	Polar angle of fibre j
r_i	Polar radius of fibre i
r_j	Polar radius of fibre j
r_f	Fibre radius
R	Gas constant
R_f	Bending radius of a fibre
$R_{f,min}$	Minimal bending radius of a fibre
R_n	Radius of an EFAM deposition nozzle
R_p	Radius of a spreader/impregnation pin
ρ_c	Density of a composite material

ρ_f	Density of a fibre material
ρ_i	Density of material i
ρ_{lin}	Linear density of a fibre bundle
ρ_m	Density of a matrix material
ρ_v	Density of a void
s	Inter-path distance
s_{min}	Minimal inter-path distance
SEM	Scanning electron microscopy
SEI	Secondary electron imaging
SDG	Sustainable development goals
$\sigma_{c,f}$	Compressive strength of a fibre material
σ_{fl}	Flexural stress (applied on a fibre)
σ_{flex}	Flexural strength
σ_t	Tensile stress (applied on a fibre)
$\sigma_{t,f}$	Tensile strength of a fibre material
t_{av}	Average thickness (of a liquid polymer film)
TGA	Thermogravimetric analysis
T_b	Temperature of a build platform
T_g	Glass transition temperature of a polymer
T_{min}	Minimal required torque

T_n	Temperature of an EFAM nozzle
T_0	Temperature at moment 0
T_1	Temperature at moment 1
T_p	Temperature of an impregnation pin
$T_{s,i}$	Temperature of the extruder at location i
τ_c	Critical shear strength
τ_i	Shear strength at a composite's interface
τ_m	Shear strength of a matrix material
τ_{xy}	XY shear stress in a fluid
θ	Contact angle, central angle
θ_X	Contact angle at location X
UD	Unidirectional
v, v_1, v_2, v_3	Linear pultrusion/mean propagation velocity
$v_{1,FFF}$,$v_{2,FFF}$, $v_{3,FFF}$	Linear velocity in an FFF process
v_c	Volume of the composite material
v_f	Volume of the fibre material
v_i	Volume of component i
v_m	Volume of the matrix material
v_v	Volume of the voids
V_f	Volume fraction of fibres in a composite

V_i	Volume fraction of component i in a composite
V_m	Volume fraction of matrix in a composite
V_v	Volume fraction of voids in a composites
$V_{v,mac}$	Macroscopic void volume fraction in an EFAM composite
$V_{v,mic}$	Microscopic void volume fraction in an EFAM composite
$V_{v,tot}$	Total void volume fraction in an EFAM composite
w	Track width of a deposited composite strand
w_f	Width of a spread fibre bundle
WD	Working distance
ω_w	Angular velocity of a pultrusion wheel
x or X	Location X
y'	Angular rotation of a fibre
y''	Derivative of angular rotation of a fibre
ξ	Macroscopic void filling factor
ζ	Ratio of layer thickness versus track width

ENGLISH ABSTRACT

The main purpose of this research was the development of an automated process for producing three-dimensional composite parts, existing of a thermoplastic matrix material, reinforced with endless fibres. This process, called Endless Fibre Additive Manufacturing (EFAM), can be seen as a series of three distinctive sub-processes. The first stage consists of the impregnation of an endless fibre bundle with a thermoplastic polymer in the liquid phase. The second stage pulls the newly formed composite strand through the wipe-off die of the impregnation stage and feeds it to the third and final stage: a heated deposition nozzle, which liquifies the matrix material within the composite strand and deposits it in an additive manufacturing (AM) process, laying-up the composite selectively and layer-by-layer into a three dimensional object.

Different from currently available technologies for automated lay-up of composite strands, the EFAM process has two separate inputs, being the dry fibre bundle and a thermoplastic polymer. This makes the production process more flexible: it allows the processing of a wide range of different matrix and fibre material combinations and enables designers to control the volume fractions of both. The combination of impregnation and deposition in one continuous and serial process has potentially structural, economic and environmental advantages.

In composite industry, there is a tendency to replace thermoset composites by their thermoplastic counterparts, when possible. An important reason for this is the larger ductility and impact strength of thermoplastic matrices, which can be explained by the different molecular structure. Thermosets have cross-linked polymeric structures, which makes them strong and stiff but also significantly more brittle because individual polymer chains cannot slip relatively to each other without chain scission, taking place during impact loads. Sufficient cooling after their processing cause thermoplastic materials to solidify and regain their strength immediately, which makes them ideal to be used in fast, continuous production processes. However, the processing of thermoplastics in composites brings other difficulties compared to thermoset resins. A major disadvantage of thermoplastic polymers is their high viscosity during final processing compared to thermoset prepolymers, which restricts the polymer flow through the voids in between an endless fibre

bundle. In other words, high matrix viscosities hamper the impregnation process of the fibre bundle.

This research assessed the impregnation quality of composite materials produced with three different 'melt' impregnation techniques. Therefore, three material samples were produced. A first material was produced using a standard pultrusion process 'Pultrusion'. A second material was processed using a passive impregnation pin technique 'PassivePin' and a third material using the in-house developed active impregnation pin technique 'ActivePin', which injects liquid polymer between a fibre bundle and a cylindrical friction surface to enhance the impregnation quality. There was aimed at a fibre volume fraction V_f of around 50 vol%. The matrix mass fractions M_m of the three different composite samples were determined as an estimator for degree of impregnation. Process 'Pultrusion' resulted in a M_m of 0.217 ± 0.0255 g/g, 'PassivePin' in 0.269 ± 0.0241 g/g and the 'ActivePin' process in 0.285 ± 0.0241 g/g, where the theoretical maximum value for M_m was 0.291 g/g. It was concluded that both the PassivePin and ActivePin techniques perform significantly better than Pultrusion. Also, the ActivePin process outperforms PassivePin in impregnation degree. Further, a stochastic method for quantifying the fibre distribution and dispersion during optical microscopy was proposed. When the findings of the morphology and fracture analyses were compared, it was clear that all results of each analysis support the conclusions made. Pultrusion material has an overall poor impregnation degree and fibre distribution and dispersion, the specimens lack mechanical strength and show fibre pull-out due to the excessive axial voids in the matrix. PassivePin material has a higher impregnation degree and a better fibre distribution, which results in less voids in the matrix and a limited fibre pull-out. Finally, the ActivePin material scores significantly higher in impregnation degree and shows an excellent fibre distribution. As a consequence, very limited voids are observed and an even fracture surface without fibre pull-out was obtained. Through the course of this study, there was a strong focus on the ActivePin technique due to its decent performance.

A fully automated impregnation device was mounted on an AM platform to be able to perform automated lay-up of thermoplastic composite material. This research discusses the main characteristics of this platform and all necessary conditions of both hard- and software to successfully perform the second stage, i.e. to pull the

composite through the first stage, to push it through the heated nozzle and to deposit it during the third stage. Important technical difficulties which were encountered during the process development during this research were documented. Solutions and possible ways for process optimisation were proposed, and in different cases also implemented and tested.

The goal of the deposition tests was to verify the 'printability' of a 40 vol% glass fibre – polyamide 12 unidirectional composite. By the successful and consistent printing of several triple layer test specimens, it was proven that the adhesion of the composite strands on the build platform was adequate and that the cohesion between the different printed tracks and layers was sufficient to make a specimen behave as one. By fine-tuning processing parameters such as layer thickness and inter-path distance, the void fraction in the composite material could be reduced to a minimum. An optical microscopy study shows the effects of the processing parameters on the composite's morphology and the similarities and differences of the morphology of an EFAM produced composite compared to a theoretical composite with a perfectly homogeneous fibre distribution and dispersion. The influence of the deposition stage on the fibre distribution and dispersion was mapped using the developed stochastic model for fibre distribution and dispersion.

The effect of processing parameters such as the nozzle temperature, layer thickness and inter-path distance on the flexural properties of the resulting composite was tested. It was found that sample production with a 0.6 mm layer thickness resulted in a higher flexural modulus, strain and strength and a more consistent failure behaviour than production with a 0.7 mm layer thickness and an identical material density. The effect of a nozzle temperature increase from 225°C to 235°C was found to be insignificant on the flexural modulus, strain and strength, but played an important role in the specimens' failure modes. Deposition at a higher nozzle temperature shifted the predominant failure mechanism from pure delamination by interlaminar shear, towards a complete break of the specimen. There were no significant interactional effects of simultaneous changes in layer thickness and nozzle temperature.

In summary, it can be said that this research succeeded in producing unidirectional, endless fibre reinforced thermoplastic composite objects, starting from a dry fibre bundle and thermoplastic polymer. The obtained material properties were

repeatable and the resulting EFAM composites proved to be having a high strength and modulus, however, their failure mechanisms are different from conventionally produced composites, e.g. using hot pressing processes. Techniques to mitigate or eliminate these differences were proposed but these differences should not necessarily be regarded as a disadvantage. Even more, these new properties could lead to a range of new applications (e.g. in health-care, sports, transportation, applications for energy absorption and controlled deformation through crumple zones) and are an interesting base for further research.

NEDERLANDSTALIG ABSTRACT

De hoofddoelstelling van deze studie is het ontwikkelen van een geautomatiseerd proces voor het produceren van driedimensionale onderdelen uit een composietmateriaal, bestaande uit een thermoplastische matrix met continuvezelversterking. Dit proces, 'Endless Fibre Additive Manufacturing' (EFAM), kan als een seriële opeenvolging van drie deelprocessen beschouwd worden. Het eerste deelproces bestaat uit het impregneren van een continuvezelbundel met een thermoplastisch polymeer in de vloeibare fase. Het tweede deelproces trekt de net gevormde composietstreng door de pultrusiekaliber van het impregnatieproces en transporteert de streng naar het derde deelproces: een verwarmde spuitkop die het matrixmateriaal in de composietstreng terug in een vloeibare toestand brengt alvorens de streng uit te smeren in een additief productieproces. In dit proces wordt het composietmateriaal selectief en laag per laag uitgesmeerd en gestapeld tot een driedimensionaal object.

Anders dan reeds bestaande, vergelijkbare technologieën voor het geautomatiseerd verwerken van composietmaterialen, start het EFAM-proces met de aanvoer van een droog vezelmateriaal en thermoplastische kunststofkorrels als twee gescheiden componenten. Hierdoor wordt het productieproces op twee manieren flexibeler: enerzijds laat dit proces toe om een uiteenlopende reeks van verschillende matrix- en vezelcombinaties te verwerken, anderzijds wordt het mogelijk om de onderlinge volumeverhouding van het matrix- en vezelmateriaal te controleren. Bovendien wordt dankzij het serieel combineren van de impregnatiestap en de vormgeving van het composiet, het bestaan van twee discrete processen vermeden, wat potentieel economische en ecologische voordelen met zich meebrengt.

In de composietindustrie is er de tendens om thermohardergebaseerde composieten - waar mogelijk - te vervangen door composieten met een thermoplastische matrix. Een belangrijke reden hiervoor is hun grotere ductiliteit en impactbestendigheid, die te verklaren valt door het verschil in moleculaire structuur. Thermoharders zijn omwille van hun driedimensionaal vernette structuren doorgaans stijver en sterker, maar ook significant brosser omdat de ketens niet ten opzichte van elkaar kunnen glijden zonder bindingen te verbreken tijdens een impactbelasting. Daarnaast zijn de snelle verwerkingstijden voor thermoplasten een voordeel: bij voldoende

afkoeling net na hun vormgeving worden onmiddellijk de finale mechanische eigenschappen verkregen. Hierdoor wordt het mogelijk om thermoplasten in snelle en continue processen te verwerken. Toch brengt het verwerken van thermoplasten in composieten ook extra complexiteit met zich mee. Een belangrijk nadeel van thermoplastische polymeren ten opzichte van thermohardende prepolymeren is hun hoge viscositeit tijdens verwerking. Dit bemoeilijkt de vloei van thermoplasten doorheen de holtes tussen individuele vezels, kortom: de impregnatie.

Tijdens dit onderzoek werden drie verschillende impregnatiemethodes getest die, gestoeld op fysische en empirische wetten, tot doel hebben om een glasvezelbundel te impregneren met het thermoplastische polyamide 12. Daartoe werden drie verschillende materiaalsamples geproduceerd. Een eerste materiaal werd gemaakt met behulp van een standaard pultrusieproces 'Pultrusion'. Een tweede materiaal werd verwerkt met een passieve impregnatiepintechniek 'PassivePin'. Een derde materiaal werd geproduceerd door middel van 'ActivePin', die vloeibaar polymeer tussen een vezelbundel en een cilindrisch wrijvingsoppervlak injecteert om de impregnatiekwaliteit te verbeteren. Een vezelvolumefractie V_f van 50 vol% werd als streefdoel vooropgesteld. De matrixmassafracties M_m van de drie verschillende composietsamples werden bepaald als een schatter voor hun impregnatiegraad. Het proces 'Pultrusion' resulteerde in een M_m van 0,217 ± 0,0255 g/g, 'PassivePin' in 0,269 ± 0,0241 g/g en het proces 'ActivePin' in een waarde van 0,285 ± 0,0241 g/g, waar de hoogst mogelijke waarde voor M_m 0,291 g/g bedraagt. Er werd geconcludeerd dat zowel de 'PassivePin' en 'ActivePin'-techniek significant beter presteren dan de techniek 'Pultrusion'. Ook presteert het proces 'ActivePin' beduidend beter dan 'PassivePin' op vlak van impregnatiegraad. Verder werd een stochastisch model voorgesteld dat toelaat om met behulp van optische microscopie de vezeldistributie en -dispersie in composietstrengen te kwantificeren. Bij vergelijking van de bevindingen uit de morfologische en breukanalyse is het duidelijk dat alle resultaten dezelfde eindconclusie ondersteunen. Het materiaal 'Pultrusion' heeft een lage impregnatiegraad en vertoont ondermaatse vezeldistributie en -dispersie, de specimens hebben een beperkte mechanische sterkte en vertonen vezel 'pull-out', dit is het lostrekken van vezels uit het matrixmateriaal, omwille van de overmatig aanwezige axiale holtes in het matrixmateriaal. Het 'PassivePin'-materiaal heeft een betere vezeldistributie en een hogere impregnatiegraad, wat leidt tot minder holtes in de matrix en een beperkte

vezelpull-out. Tot slot scoort het materiaal 'ActivePin' significant beter op vlak van impregnatiegraad en toont een goede vezeldistributie. Bijgevolg werd slechts een beperkte hoeveelheid holtes waargenomen en werd er een vlak breukoppervlak zonder pull-out verkregen. Omwille van zijn goede werking werd er verder in dit onderzoek gefocust op de 'ActivePin'-techniek.

Een volledig geautomatiseerd impregnatietoestel werd in een additief productieplatform, ook wel een '3D-printer' genoemd, gemonteerd om het composietmateriaal geautomatiseerd te kunnen uitsmeren. In dit werk worden de belangrijkste kenmerken van dit platform en alle nodige voorwaarden voor zowel hard- als software besproken om te slagen in het tweede en derde EFAM-sub-proces, i.e. het composietmateriaal doorheen de eerste fase trekken en het doorheen de verwarmde spuitkop duwen en uitsmeren. Technische moeilijkheden en beperkingen die aan het licht kwamen tijdens de ontwikkeling van het gehele proces werden gedocumenteerd. Oplossingen en mogelijkheden voor optimalisatie werden voorgesteld en in verschillende gevallen ook doorgevoerd en getest.

Het doel van de uitsmeertesten is de "printbaarheid" van een unidirectioneel composiet bestaande uit een polyamide 12 met 40 vol% glasvezelversterking na te gaan. Door het succesvol en consistent printen van verscheidene testspecimens van drie lagen dik werd enerzijds aangetoond dat de adhesie van het composietmateriaal op het bouwplatform voldoende was om succesvol meerdere lagen te printen. Anderzijds werd aangetoond dat de cohesie tussen de verschillende geprinte strengen en lagen van dusdanige aard was dat de specimens zich als één solide geheel gedroegen. Door het afregelen van procesparameters zoals laagdikte en inter-padafstand kon de ongewenste holtefractie tot een minimum beperkt worden. Een optische microscopiestudie maakte de effecten van de procesparameters op de composietmorfologie duidelijk. Daarnaast werden morfologische gelijkenissen en verschillen tussen een EFAM-composiet en een geïdealiseerd composiet in kaart gebracht. Bovendien brengt de gelijkenissen en verschillen tussen een door middel van EFAM geproduceerd en een theoretisch composiet met een perfect homogene vulling, vezeldistributie en -dispersie in kaart. Ook de invloed van het uitsmeerproces op de vezeldistributie en -dispersie werd nagegaan.

Het effect van verwerkingsparameters zoals de spuitkoptemperatuur, de laagdikte en de inter-padafstand op de buigeigenschappen van het resulterende composiet werd getest. Er werd besloten dat de productie van samples met een laagdikte van 0,6 mm tot een hogere buigmodulus, buigsterkte en buigrek en een meer consistent faalgedrag leidde dan productie met een laagdikte van 0,7 mm en eenzelfde densiteit. Het effect van een temperatuursverhoging van de spuitkop van 225°C naar 235°C bleek insignificant voor buigmodulus, buigsterkte en buigrek, maar speelt een belangrijke rol in de faalmodi van de samples. Uitsmeren van het composietmateriaal op hogere temperaturen wijzigt het voornamelijk falen door delaminatie, veroorzaakt door afschuiving tussen de geprinte lagen onderling, naar een complete specimenbreuk. Verder werden er geen significante interactie-effecten tussen laagdikte en spuitkoptemperatuur waargenomen.

Samenvattend kan gesteld worden dat dit onderzoek erin geslaagd is om op geautomatiseerde wijze objecten te produceren in een unidirectioneel continuvezelcomposiet met thermoplastische matrix. De behaalde materiaaleigenschappen waren in hoge mate herhaalbaar en het resulterende EFAM-composiet bleek over een hoge sterkte en modulus te beschikken. De breukmechanismen van dit geproduceerde composiet wijken echter af van mechanismes bij conventioneel geproduceerde composieten. Technieken om deze verschillen tot een minimum terug te brengen werden voorgesteld, maar de aangehaalde verschillen moeten an sich niet als een nadeel beschouwd worden. Sterker nog, deze nieuwe materiaaleigenschappen kunnen leiden tot nieuwe toepassingen (bijvoorbeeld in de gezondheidszorg, sport, transportsector, toepassingen voor energieabsorptie en gecontroleerde vervorming met behulp van kreukelzones) en vormen een interessante basis voor verder onderzoek.

TABLE OF CONTENTS

1 SCOPE OF THE RESEARCH

1.1 INTRODUCTION

This chapter commences by introducing some key concepts and terminology that will be important throughout the complete course of this study and that are necessary for a proper understanding of this study's narrative. In the second part of this chapter, different currently existing techniques for automated composite production will be mapped and their performance will be compared. The composite production technique which was developed during this research will be conceptually introduced and compared to emerging and currently existing (automated) composite lay-up technologies. The innovative aspects, envisaged advantages and possible disadvantages of this new technique, compared to its competitors will be reviewed and the technology will be situated in current manufacturing chains and the targeted markets. The principal aims and objectives of this research will be discussed, mainly from a material science perspective, but also from a more general, ecological, economical, and societal point of view. This chapter ends with an overview of the complete dissertation.

1.2 KEY CONCEPTS AND TERMINOLOGY

1.2.1 Additive Manufacturing

Additive Manufacturing (AM), often referred to as '**3D printing**', is a production technique following a completely different paradigm than the traditional, **subtractive manufacturing**. Rather than removing the unwanted material from a billet of material, hence the name 'subtractive', additive manufacturing produces objects starting from a base material in the form of powder, pellets, liquid resin, gel or filament which is brought in a processable state and subsequently selectively deposited point-by-point and layer-by-layer to build up an object. AM reduces limitations in traditional manufacturing techniques, improves design freedom and

possibly also part performance. Depending on the part design and additive technology used, AM can potentially reduce the material usage during part production [1], [2]. The use of AM excels where customized, light-weight, high-performance parts are pursued. Within this work, the focus will be on extrusion-based AM technologies (EAM). Two widespread examples of EAM are Fused Deposition Modeling (FDM) and its open-source equivalent Fused Filament Fabrication (FFF). Both techniques use a thermoplastic filament as their feedstock and selectively deposit it after liquefying it in a heated nozzle. Particles and short fibres can be added to these filaments to alter the final product's mechanical properties.

1.2.2 Composite material

A composite material, or 'composite' in short, is a structural combination of at least two different materials, often - but not necessarily - from different material classes (being metals, polymers and ceramics, e.g. glass). Unlike metal alloys, where mixing happens through solid solutions or intermetallic bonds, the different materials remain as separate phases in composites, whether that be on the macro, micro or nanoscale. Material properties of the composite will be a combination of the components' properties, synergistic effects between the constituents are often pursued. The continuous phase of a composite is called the **matrix** (Figure 1.1, white), while the dispersed phase is called the **filler** or **reinforcement** (Figure 1.1, blue). The contact zone between matrix and filler is the **interface** (Figure 1.1, yellow) and is of major importance for stress transfer during mechanical or thermal loading of the composite. Between matrix and filler, an artificial coating or **sizing** might be present in order to alter the filler-matrix interaction. Generally, the purpose of a sizing is to increase the interfacial adhesion, but there are known applications where the possibility for slip between matrix and filler is aimed at. A list of important polymers, fillers (fibres) and their relevant (mechanical) properties is given in Appendix 1 and 2.

The majority of industrial composites have a polymer matrix, e.g. a polyamide-glass fibre composite, which typically consists of a polyamide matrix and a reinforcement of silane coated glass fibres. All constituents of such a composite can be distinguished in Figure 1.2.

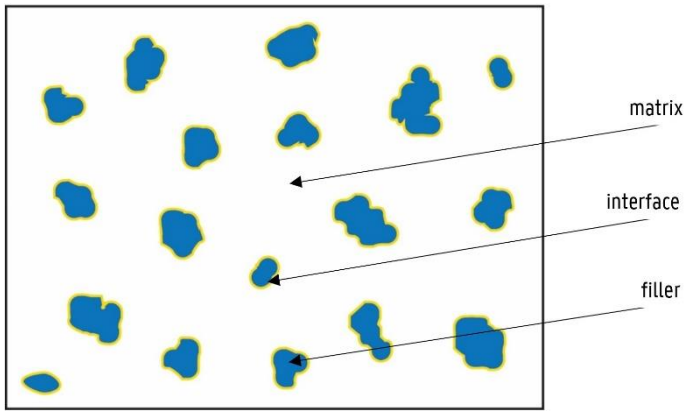

Figure 1.1: Schematic representation of a composite material. Matrix material (white), filler (blue) and interface (yellow).

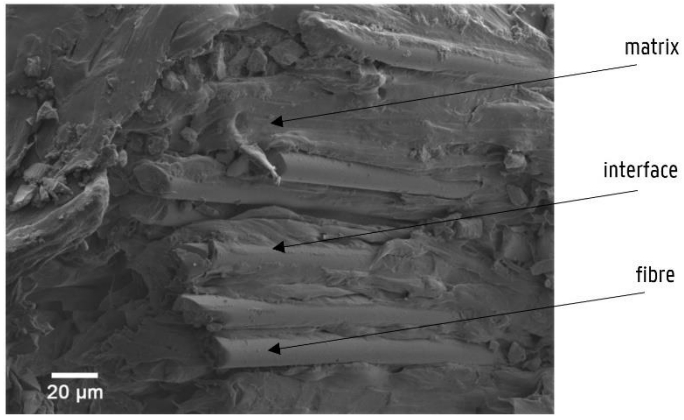

Figure 1.2: Fracture surface of a polyamide - glass fibre composite.

1.2.3 Filler aspect ratio and critical filler dimension

The filler or dispersed phase of a composite can take different sizes and shapes. Fillers can be nanosized particles such as carbon nanotubes or platelets to macro sized gravel in concrete. The shape of a filler is independent of its size and is often described by its **aspect ratio**, which is the ratio of the filler's maximal dimension (11 in Figure 1.3) and its minimal dimension, measured orthogonally to the axis of maximal dimension (22 or 33 in Figure 1.3). Particles having similar dimensions in all three orthogonal dimensions are **equi-axial** and have an aspect ratio close to unity.

An example of equi-axial particles are the glass beads being used in dental filling composite.

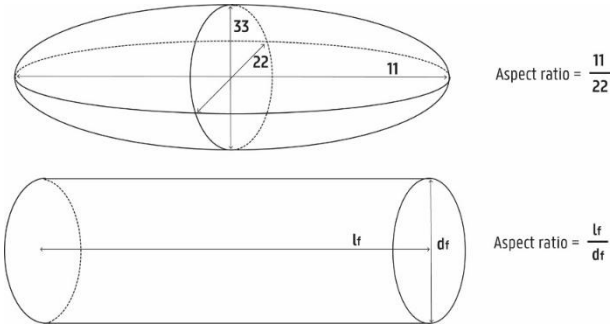

Figure 1.3: Idealised ellipsoidal particle with dimensions measured in three orthogonal axes (11 being the principal direction, 22 and 33, being orthogonal directions which do not necessarily have the same dimensions) (upper sketch), idealised fibre with length l_f and diameter d_f (lower sketch).

Fibre fillers can be used in a great range of aspect ratios, depending on the production process being used. **Short fibres** with a length of up to several millimetres can be compounded together with thermoplastic polymers to be used in an injection moulding process, where they have a moderately strengthening and stiffening effect on the properties of the final product. Fibres are considered to be **continuous fibres** when their length is at least 15 times longer than their **critical fibre length** l_c [3], which is defined in Equation 1.1. l_c is an indicator for stress transfer between matrix and fibre [4]: the larger the fibres' tensile strength $\sigma_{t,f}$ and diameter d_f are, the longer a fibre needs to be to successfully reinforce a composite. Large critical shear strengths τ_c, i.e. the maximum of the shear strength of the matrix and the matrix-fibre interface, reduce l_c. This implicates that smaller fibres succeed in reinforcing a composite in the case of a strong interface.

$$\begin{cases} l_c = \dfrac{\sigma_{t,f}\, d_f}{2\,\tau_c} \\ \tau_c = \min(\tau_i, \tau_m) \end{cases} \tag{1.1}$$

d_f	Single fibre diameter	[mm]
$\sigma_{t,f}$	Tensile strength of the fibre	[MPa]
τ_c	Critical shear strength	[MPa]
τ_i	Shear strength of the interface	[MPa]
τ_m	Shear strength of the matrix	[MPa]

As the average fibre length in a composite increases, a larger proportion of the fibres can be loaded up to the fibre material's tensile strength, which makes the reinforcement more efficient. High-end **composite laminates** typically exist of **endless fibre**, which are longer than 'continuous' fibres and can span a significant amount of a composite part (up to several metres), either in unidirectional (UD) or in woven fibre laminae.

1.2.4 Dispersion and distribution of a filler in a matrix

The distribution and dispersion of a filler in a matrix are of great importance for the mechanical performance of a composite. **Distribution** can be defined as the evenness of being spaced out – or distributed – of a filler material throughout a complete composite part. A filler is well-distributed if the amount of filler is similar in both halves when you cut a part in half, in any possible direction (Figure 1.4, right composites). **Dispersion** is a measure of to what extent the bonding between coagulated filler is broken, and consequently how good the mixing on the smallest level occurred (Figure 1.4, lower composites). The bottom right composite on Figure 1.4 has the best distribution and dispersion of the filler material and will generally outperform the other parts when it comes to stress transfer, stress redistribution and fatigue strength.

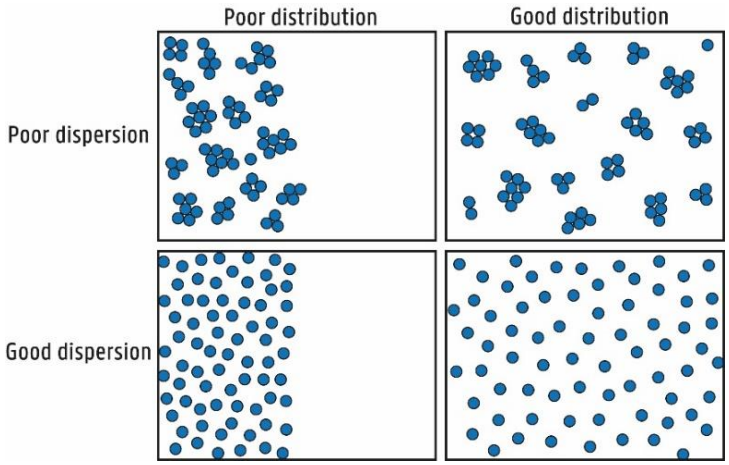

Figure 1.4: Schematic representation of composite materials with poor and good filler distribution and dispersion in the matrix.

1.2.5 Apparent viscosity

Consider a fluid between two parallel plates at a constant distance h from each other (Figure 1.5). The lower plate is fixed in space, the upper plate is moving at a constant linear velocity v. The fluid will deform under the applied shear rate and will induce a one-dimensional flow parallel to the movement of the upper plate, a so-called Couette flow. Depending on the type of fluid, the relation between applied shear rate and the shear stresses in the fluid will be different. A general form of this relation is the **power law model** (Equation 1.2), in which η is the **apparent viscosity** (Equation 1.3). From these equations, one can deduct that an increase in shear-rate will result in a higher shear-rate within the fluid. Lowering the shear stress under a constant shear-rate is only possible by lowering the fluid's viscosity.

$$\tau_{xy} = \eta \frac{dv}{dy} \tag{1.2}$$

$$\eta = k \left|\frac{dv}{dy}\right|^{n-1} \tag{1.3}$$

$\frac{dv}{dy}$	Shear rate	[1/s]
k	Consistency index	[/]
n	Flow behaviour index	[/]
η	Apparent viscosity	[Pa s]
τ_{xy}	Shear stress	[MPa]

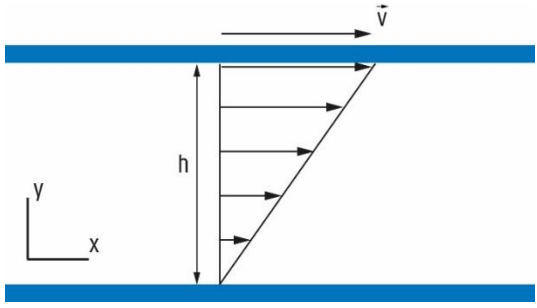

Figure 1.5: Couette flow between two parallel plates, moving upper plate and stationary lower plate.

For a n-value of 1, η becomes independent of the applied shear rate (Equation 1.3), this is the specific case for Newtonian fluids (Figure 1.6). When n is smaller than 1, the fluid is **shear-thinning** or **pseudo-plastic**. This property is typical for thermoplastics in the liquid phase. n-values larger than 1 indicate a **shear-thickening** or **dilatant** fluid.

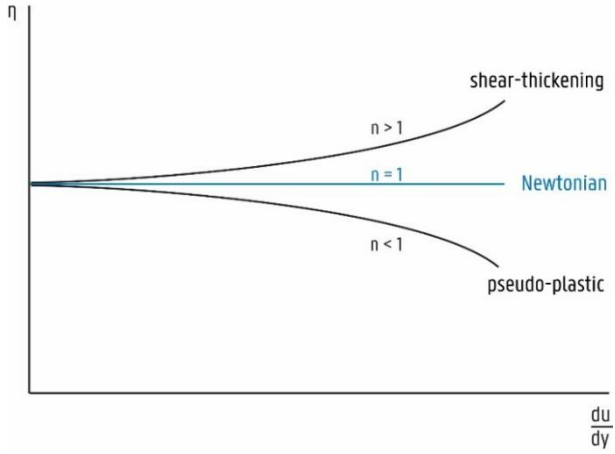

Figure 1.6: Apparent viscosity for different fluid types as a function of applied shear-rate.

1.3 GENERAL SCOPE OF THE DISSERTATION

This dissertation focuses on the improvement of currently existing AM materials by the introduction of endless fibres within matrices in extrusion-based AM. A technique to successfully incorporate these endless fibre within a liquified matrix material and to deposit the newly formed composite subsequently into three-dimensional objects will be developed and named Endless Fibre Additive Manufacturing (EFAM). Although EFAM could be capable of processing thermosets or vitrimers as a matrix material, this work will only focus on thermoplastic matrices.

This work will highlight important mechanical construction and machine control aspects during the design, testing and optimisation of the EFAM equipment and process. These considerations are necessary to have a fully automated EFAM process, capable of manufacturing three-dimensional composite objects. Further, the EFAM-

produced composites will be looked at from a material science point of view. Linking processing parameters to composite morphology and mechanical properties will be key in this.

In Section 1.4, an overview of the current state-of-the-art research within this domain is given. This will form the necessary information for further discussion of the innovative aspects of AM with endless fibres in general and especially when comparing EFAM to other AM techniques, incorporating endless fibres, as will be discussed in Section 1.5. Clear aims and objectives for this research will be set in Section 1.6. Lastly, Section 1.7 will give an overview of the complete dissertation.

1.4 STATE-OF-THE-ART: AM WITH ENDLESS FIBRES

Extrusion-based Additive Manufacturing (EAM) techniques for thermoplastics have been mainly developed during the last three decades. However, optimisations of this type of manufacturing processes were often limited to machine and software developments. In order to improve the limited mechanical properties such as strength, stiffness and thermal stability of additively manufactured products compared to their injection moulded counterparts, short fibre filled AM materials have been introduced more recently [5], [6]. This was seen in the work of Tekinalp [7], Ning [8], Compton [9], Ferreira [10], Raney [11], Kishore [12], Brenken [13], Karsli [14], Zhong [15] and Zhang et al. [16]. Depending on the volume fraction of the added fibres V_f, these composites are often more brittle than the unfilled polymer material [17]–[20].

To further expand the possibilities of extrusion-based AM materials, different processes which incorporate endless fibres into polymers were developed recently. However, this approach requires an important adaptation of regular EAM processes. Four main types of extrusion-based production techniques for endless fibre composites are currently being researched. An overview of those techniques can be found in Figure 1.7.

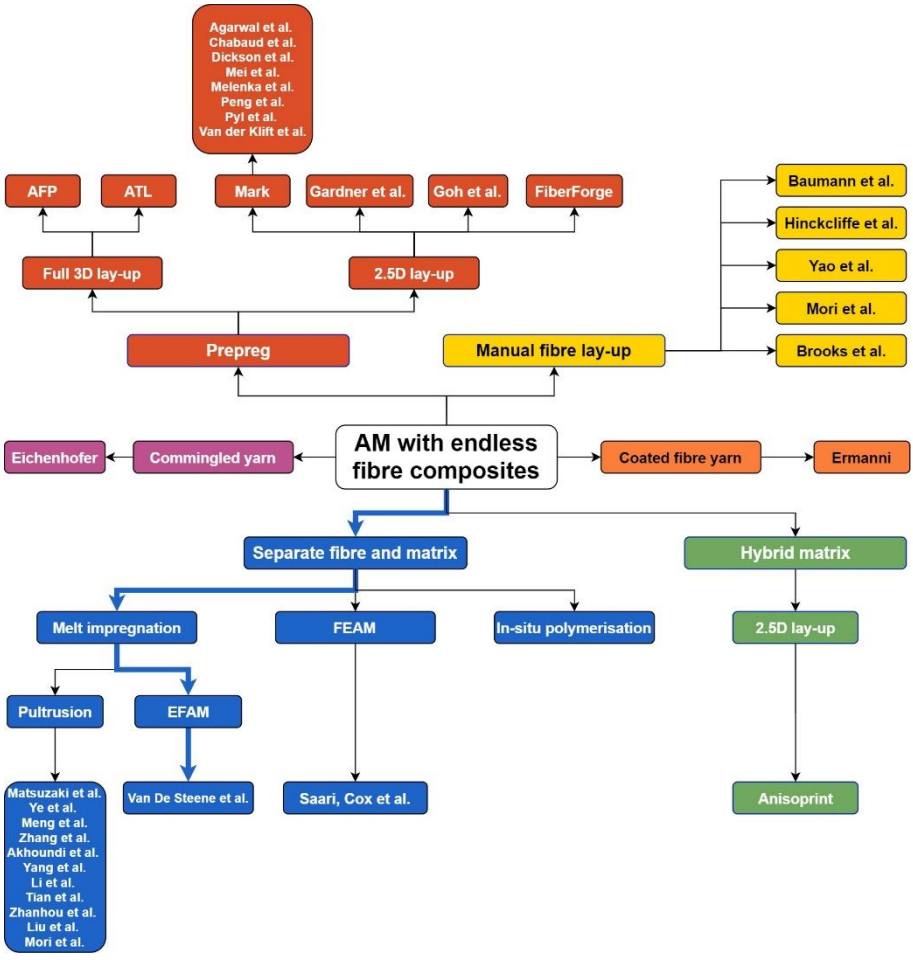

Figure 1.7: Overview of important AM methods using endless fibres.

1.4.1 Prepreg-based endless fibre AM

A first category of methods ('Prepreg' branch on Figure 1.7, red) deposits a fibre bundle, pre-impregnated with a thermoplastic polymer (often referred to as 'prepreg'), after the latter was liquified in a heated nozzle. This technique can be considered as a small-scale version of the existing technologies Automated Tape Laying (ATL) and Automated Fibre Placement (AFP), which were thoroughly reviewed by Lukaszewicz et al. [21] and Qureshi et al. [22]. The small-scale prepreg deposition technique was previously patented by Jang et al. [23] and Mark et al. [24]. The latter patent resulted in a commercially available device for 2.5-dimensional composite

lay-up, i.e. deposition in planar layers. Typical ATL and AFP processes on the other hand, allow full three-dimensional lay-up, this is deposition of mere prepreg material onto (double-)curved moulds with small to moderate curvature. Mark's composite 3D printer is equipped with a second extruder for thermoplastic filaments, which enables the local deposition of neat matrix material, lowering the object's global V_f. Goh et al. [25] used Mark's proprietary prepreg material to produce flexural specimens (i.e. for testing under a bending or flexural load), without the addition of extra matrix material, which resulted in a 35 vol% glass fibre – polyamide 6 (PA6) and a 41 vol% carbon fibre – PA6 unidirectional composite. Composite material produced by Mark's device was extensively researched. Important contributions with respect to tensile [25]–[33], flexural [25], [34], compressive [34] and impact properties [35], interlaminar bonding performance [36], creep [37], fatigue [37], open-hole strength [38], morphology [25], [27], [32], [39], [40] and failure behaviour [29], [31], [33], [36], [37] were made during the last few years. Another commercial technique by FiberForge performs 2.5D prepreg tape lay-up and a subsequent hot pressing step to consolidate the composite material and form objects with three-dimensionally oriented endless fibres [41], [42]. Furthermore, Gardner et al. researched the 2.5D deposition of endless carbon nanotube (CNT) yarn [43], infused with a solution of polyetherimide (PEI), combined with the possibility for separate extrusion of neat polyetherimide. This approach is analogous to Mark's technique and enables production of a polymer object with local fibre reinforcement or conductive tracks, where required. Important material characteristics of composites produced during abovementioned researches are listed in Table 1.1. It can be noticed there is a strong variability in the reported mechanical properties, this is due to difference in constituents, fibre volume fractions V_f and fibre orientations used in the composite material. The obtained fibre volume fractions are rather low compared to typical volume fractions of ~ 55 to 65% for unidirectional AFP and ATL produced material [2], [44], [45] or ~ 60 to 80% for conventionally compression moulded unidirectional composites [46]. Especially the works of Goh et al. and Dickson et al. will be useful for use as a benchmark in this study since they reported relevant mechanical data such as tensile and flexural data for a composite material very similar to the one that will be studied in this work.

Table 1.1: Overview of recently researched prepreg unidirectional composite AM materials and their fibre volume fractions. Standard deviations for V_f and mechanical properties were not shown since most data were unavailable.

Research	Fibre	Matrix	V_f [vol%]	Tensile strength [MPa]	Young's modulus [GPa]	Flexural strength [MPa]	Flexural modulus [GPa]
Agarwal et al. [30]	glass	PA6	50[a]	284	8.9	/	/
Chabaud et al. [27]	carbon	PA6	30.0	480[b]	50.0[b]	/	/
Chabaud et al. [27]	glass	PA6	33.1	380[b]	22.5[b]	/	/
Chabaud et al. [27]	carbon	PA6	35.0[c]	534[c]	60.0[c]	/	/
Chabaud et al. [27]	glass	PA6	39.0[c]	265[c]	23.5[c]	/	/
Dickson et al. [31]	carbon	PA6	11	198	8.5	250	13.0
Dickson et al. [31]	glass	PA6	10	212	4.9	197	4.2
Dickson et al. [31]	glass	PA6	33	440[b]	/	/	/
Dickson et al. [31]	aramid	PA6	10	161	4.8	126	6.7
Gardner et al. [31]	CNT	PEI	/	115[b]	2.5[b]	/	/
Goh et al. [25]	carbon	PA6	41.0	600	13.0	430	38.0
Goh et al. [25]	glass	PA6	35.0	450	7.2	149	14.7
Mei et al. [29]	carbon	PA6	9.0[d]	106[d]	4.3[d]	/	/
Melenka et al. [28]	aramid	PA6	10.1	83[b]	9.0	/	/
Peng et al. [33]	carbon	PA6	41.0	516	39.0	/	/
Pyl et al. [38]	carbon	PA6	± 27	719	58.1	/	/
Van Der Klift et al. [26]	carbon	PA6	34.5	464	35.7	/	/

[a] it is assumed that the prepreg volume fraction instead of the fibre volume fraction was mentioned
[b] values interpolated from graphs
[c] values after manual removal of a pure matrix specimen shell
[d] measured on a $[0°/45°/90°]_2$ composite material

1.4.2 In-printhead melt impregnation endless fibre AM

A second category of methods incorporates both composite production and deposition in a single process ('Separate fibre and matrix' branch on Figure 1.7, blue). These methods start from a dry fibre bundle and polymer as two separate components, which are - in most cases - combined inside an impregnation device right before the deposition step by submersion or pultrusion of the fibre bundle in a liquid matrix medium i.e. a polymer 'melt', a polymer solution or a monomer precursor. Although this method is called melt impregnation, it can also be used with amorphous thermoplastics, which do not show a melting region. This in-situ melt

impregnation approach requires a proper fibre bundle impregnation technique to be able to obtain a mechanically stiff and strong material, as described by Huang [47], with no or limited voids [48]. This methodology is currently being researched by Bettini [49], Matsuzaki [50], Ye [51], Meng [52], Zhang [53], Akhoundi [54], Yang [55], Li [56], Tian [57], Zhanhou [58] and Liu [59]. The fibre volume fractions of the composites created in these researches is ranging from less than 1 vol% up to around 50 vol%, with strongly varying void content and fibre distribution and dispersion. Another method within this category was used by Saari et al. [60] and Cox [61] et al. They incorporated a single copper wire in unfilled thermoplastic materials, downstream of an extruder for deposition of unfilled thermoplastic polymers and called their method 'Fiber encapsulation additive manufacturing' (FEAM). Luan et al. impregnated a carbon fibre bundle with polylactic acid (PLA), starting from a filament material, to use as strain gauges, incorporated in 3D-printed PLA parts [62]. Important material characteristics of composites produced in these researches are listed in Table 1.2. It can be noticed that there is a strong variability in the reported mechanical properties, this is due to difference in materials, fibre volume fractions and fibre orientations used in the research. In contrast with the prepreg-based methods, there is a strong emphasis on typical FFF materials such as PLA and acrylonitrile butadiene styrene (ABS) as a matrix material. Also the use of the engineering polymers polyether ether ketone (PEEK) [52] and polyimide (PI) [51] as a matrix was researched. In Figure 1.7, an extra branch 'In-situ polymerisation' was added, however research on this topic is limited to non-existent, especially for thermoplastic polymers.

Table 1.2: Overview of recently researched unidirectional composite AM materials produced by in-line melt impregnation and their fibre volume fractions. Standard deviations for V_f and mechanical properties were not shown since most data were unavailable.

Research	Fibre	Matrix	V_f [vol%]	Tensile strength [MPa]	Young's modulus [GPa]	Flexural strength [MPa]	Flexural modulus [GPa]
Akhoundi et al. [54]	glass	PLA	49.3	479	29.4	/	/
Bettini et al. [49]	aramid	PLA	8.6	203	9.3	/	/
Heidari-Rarani et al. [63]	carbon	PLA	28.2	61	8.3	152	13.4
Li et al. [56]	carbon	PLA	34	91	/	156	/
Matsuzaki et al. [50]	carbon	PLA	6.6	185	19.5	133	5.9
Matsuzaki et al. [50]	jute	PLA	6.1	57	5.1	/	/

Meng et al. [52]	carbon	PEEK	/	/	/	480	37.0
Mori et al. [64]	carbon	ABS	0.2 - 1.6[a]	43[a]	/	/	/
Tian et al. [57]	carbon	PLA	27	/	/	335	30.0
Yang et al. [55]	carbon	ABS	6.5	147	4.2	127	7.7
Ye et al. [51]	carbon	PI	/	64[b]	/	83[b]	/
Zhanghou et al. [58]	carbon	PLA	11.5	/	/	/	/

[a] a combination of unidirectional layers and ±45° layers was used

[b] values interpolated from graphs

1.4.3 Hybrid matrix endless fibre AM

A third method consists of coating a thermoset-based prepreg strand with thermoplastic polymer just before its deposition, creating a composite consisting of a hybrid thermoset-thermoplastic matrix ('Hybrid matrix' branch on Figure 1.7, green) [65]. This technique was made commercially available by Anisoprint. Commercial materials are carbon or basalt fibres in a proprietary thermoset epoxy-based prepreg, which can be combined with polyethylene terephthalate (glycol-modified) (PET-G) as a matrix material. A major advantage of this technique is the good intra-fibre bundle impregnation with the low viscosity thermoset prepolymer, while the higher viscosity thermoplastic material is concentrated mainly between the different composite strands [65]. A possible disadvantage of this technology is the unpredictable adhesion quality between both thermoplastic and thermoset matrix components, since its occurrence is not well-studied and raises concerns with regard to e.g. interfacial adhesion, differences in stiffness, thermal expansion coefficients, stress concentration, aging effects, etc. within the matrix. Compared to a single-phase matrix composite, a different failing behaviour is to be expected. Important material characteristics of composites produced using this technique are listed in Table 1.3.

Table 1.3: Overview of recently researched unidirectional composite AM materials with a hybrid matrix and their fibre volume fractions.

Research	Fibre	Matrix	V_f [vol%]	Tensile strength [MPa]	Young's modulus [GPa]	Flexural strength [MPa]	Flexural modulus [GPa]
Azarov et al. [65]	carbon	PET-G	25	860	64.0	520	/
Azarov et al. [65]	basalt	PET-G	25	430[a]	32.0[a]	/	/

[a] preliminary results, further research needed for accurate values

1.4.4 AM with manual fibre insertion

A fourth method consists of manual insertion of fibre bundles into a (thermoplastic) matrix, during or subsequently to an EAM process ('Manual fibre lay-up' branch on Figure 1.7, yellow). Baumann et al. tested three different processes to manually incorporate 0.6 vol% ECR-glass and 0.3 vol% carbon fibre into ABS based tensile specimens [66]. In a first process, they directly overprinted a dry fibre bundle. In a second process, a heated hypodermic needle was used to guide the fibre bundle and deposit it on a partially liquified ABS layer. In a third process, the ABS substrate was partially solved using acetone before manual lay-up of fibre bundles. It was concluded that the use of fibres increased the Young's modulus of all specimens. Only the incorporation of glass fibres was successful to increase the specimens' tensile strength. Further, the direct overprinting process outperformed the other processes. In a preliminary research, Baumann et al. showed that the printing of 6 vol% carbon fibre in an ABS matrix was successful. Yao et al. manually reinforced PLA based tensile and flexural specimens with a thermoset based carbon fibre prepreg strand and reported a 70% increase in tensile strength and a 18.7% increase in flexural strength of the specimens compared to non-reinforced specimens [67]. Hinckcliffe et al. inserted endless jute flax fibres into channels within finished additively manufactured objects and post-tensioned the fibre material to enhance the mechanical properties of the object [68]. Hinckcliffe et al. showed that it is possible to increase the specific tensile and flexural mechanical properties of tensile and flexural specimens. However, the resulting structure cannot be said to be a composite since there is no physical interface between polymer and fibre, other than the two anchor points at the specimens' both ends. Mori et al. compared three processes, being manual insertion of a dry carbon fibre bundle during an EAM process, whether or not followed by a "thermal bonding step" and an in-line melt impregnation process, combining a ABS filament with endless carbon fibres [69], [64]. They found that without the thermal post-treatment, carbon fibres were pulled out of the matrix during a tensile test and were unable to significantly increase the tensile strength of a specimen. Specimens that were thermally post-treated had roughly twice the tensile strength compared to the untreated specimens. Also, a significant increase in tensile and flexural fatigue strength was found after this thermal treatment. After in-line addition of a carbon fibre bundle in the EAM process, an increase of around 300% in tensile strength was achieved, compared to the pure

matrix specimens. This indicates a major advantage of direct in-line impregnation before deposition compared to manual insertion of a (dry) fibre bundle as reinforcement. Brooks et al. demonstrated the advantages of inserting different fibre materials into some well-chosen additively manufactured demonstrator parts [70]. A strength increase up to 4000% and a stiffness increase of 200% were achieved. Material characteristics of composites produced in these researches are listed in Table 1.4. It can be noticed that the obtained fibre volume fractions are rather low, thus the reinforcing effect is less pronounced than in previously described methods.

Table 1.4: Overview of recently researched unidirectional composite AM materials with manual fibre insertion and their fibre volume fractions. Standard deviations for V_f and mechanical properties were not shown since most data were unavailable.

Research	Fibre	Matrix	V_f [vol%]	Tensile strength [MPa]	Young's modulus [GPa]	Flexural strength [MPa]	Flexural modulus [GPa]
Baumann et al. [66]	carbon	ABS	0.30	41	2.0	/	/
Baumann et al. [66]	carbon	ABS	6.00	/	/	/	/
Baumann et al. [66]	E-CR glass	ABS	0.60	49	2.1	/	/
Brooks et al. [70]	carbon	ABS	/	/	/	/	/
Brooks et al. [70]	carbon	PLA	/	/	/	/	/
Mori et al. [64]	carbon	ABS	1.45	30	/	/	/
Yao et al. [67]	carbon	PLA	/	33	/	68	/

1.4.5 Other methods for endless fibre AM

Two other methods which are currently not widespread are the deposition of commingled yarns ('Commingled yarn' branch on Figure 1.7, purple), as described by Eichenhofer et al. [71] and the deposition of glass fibre bundles in which each individual fibre was spray coated with a thermoplastic polymer in a prior process ('Coated fibre yarn' branch on Figure 1.7, orange). Although this paradigm requires an additional and expensive coating step after production of a single fibre, this method strongly reduces the necessary travel length of the liquified polymer during an impregnation process. This technique was previously described by Ermanni [71], but to the author's knowledge, no elaborate process description, nor test results regarding composite production with this semi-impregnated or 'semipreg' material have been published so far.

Within this doctoral dissertation, the second methodology for in-line impregnation of a dry fibre bundle with a thermoplastic polymer and the consecutive deposition of this composite material was used and named Endless Fibre Additive Manufacturing (EFAM), (Figure 1.7). Compared to abovementioned researches within its branch of processes, EFAM uses additional measures to improve fibre distribution and dispersion in a thermoplastic matrix, as will be discussed in Section 1.5. Further, the matrix material can be supplied in the industrially accepted form of pellets, rather than in filament form, which is the current standard for FFF processes.

1.5 INNOVATIVE ASPECTS

This paragraph will discuss relevant innovative aspects of AM with endless fibre composites in general and the innovation this dissertation brings compared to other in-printhead melt impregnation endless fibre AM. The EFAM composite production technique which was developed during this research will be conceptually introduced. Further, the envisaged advantages and possible disadvantages of this new technique will be reviewed and the technology will be situated in current manufacturing chains and the targeted markets.

1.5.1 Conventional versus automated composite lay-up

The classical lamination theory for composites shows that the fibre orientation angles and lay-up sequence determine the stiffness and strength of a composite material. The composite material will will often be highly anisotropic, meaning that strength and stiffness can be highly dependent on the testing orientation. In conventional composite lay-up, each lamina can be represented by its stiffness matrix. The strength and stiffness of a complete laminate can be tailored by choosing the orientation and stacking sequences of the individual laminae. For a composite part in which the expected loads are well-known, the fibre orientation can be chosen so that it coincides with the occurring stresses where possible. Conventional lamina usually exist out of unidirectional or woven endless fibre material, so the smallest unit to which extent a conventional composite part can be optimised is one lamina. This limitation can be mitigated by automated lay-up technologies which can deposit composite tapes or strands along complexly curved

trajectories within a non-planar lamina. Fibre orientation can be tailored so that it coincides with the occurring maximum principal stress trajectories, as demonstrated by Zhang et al. [53]. They succeeded in reducing stress concentration in both fibre and matrix of an open-hole lamina significantly and increased its stiffness. Dickson et al. came to a similar conclusion for an additively woven open-hole laminate with optimized fibre orientation around an open-hole in tensile mode [72]. Pyl et al. added a concentric fibre reinforcement round an open-hole, rather than an optimised fibre orientation [38] and found a negative effect on the part's tensile strength, when being compared with drilled holes.

Additive manufacturing technologies often bring the added benefit of more design freedom, since they can produce complex shapes such as light-weight lattice structures [59], [71], hollow and topology-optimised structures [53], [70], [72], [73], etc. that are hard or impossible to produce using traditional production technologies. This often leads to new applications, integrated new functionalities, a reduction in part count and/or mass. A mass reduction is especially interesting for the transportation sector, where there is a strong link between mass, fuel consumption and the emission of greenhouse gases. Further, producing 'nearly net shape objects' through AM results in significantly less wastage during production and in a cost reduction compared to conventional composite production techniques, as described by Lukaszewicz et al. [2]. Depending on the additive technology used, the 'buy-to-fly ratio', i.e. the ratio of the base material's mass to the final product's mass can approach unity. In this regard, AM contrasts sharply with subtractive techniques, where buy-to-fly ratios of 15 to 20 are not uncommon.

In conclusion, it can be said that the highly automated, additive manufacturing techniques for composites have the potential to create smart, light-weight, strong and stiff objects. The following, hypothetical example illustrates the possible benefits of the use of AM techniques during composite processing. Consider a GE90 (General Electric) jet engine fan blade (Figure 1.8), which is built-up out of around 1700 complexly shaped lamina of carbon fibre prepreg, all of which are laid-up and compacted manually onto a complexly shaped mould. The complete production process takes approximately 300 hours, and is very intensive in manual labour. Automating this lay-up process would take away the human factor, would lead to a more efficient material use and could possibly lead to more design freedom,

continued optimisation and a mass reduction of the fan blade, resulting in a higher fuel economy of the jet engine.

Figure 1.8: General Electric GE90 jet engine, with its 18 fan blades.

These ideas, assumptions and findings strongly relate to the 2030 Agenda for Sustainable Development, adopted by all United Nations Member States in 2015, which provides a shared blueprint for peace and prosperity for people and the planet, now and into the future. The relation to Sustainable development goals (SDG) 9, 11, 12 and 13 is trivial (Figure 1.9). However, less evident relations with other SDG's are present, e.g. the aforementioned higher degree of automation in industry can shift a job market which previously required a large quantity of low-skilled jobs towards a market where highly-skilled specialists are valued higher. Such societal effects are hard to predict, but it is a part of the broader SGD transition idea to contemplate these effects in order to shift towards a more sustainable future.

Figure 1.9: Summary of the 17 Sustainable Development Goals (Source: United Nations, 2015).

1.5.1 Use of composites versus traditional materials

Composites enable creation of light-weight structures compared to traditional metal based construction, due to the typically low densities of common matrix and filler materials (Appendix 1 and 2). This leads to lower mass and inertia of the final product, enabling dynamic systems with higher acceleration an deceleration values, less friction losses and fuel emissions in for example transportation. The good formability of composites leads to increased ergonomic properties of final composite parts. Therefore, composites are often used in health-care, where tailored, light-weight, stiff and strong orthosis are required.

1.5.2 Concept of EFAM within this work

Endless Fibre Additive Manufacturing is an AM process in which a composite strand is selectively deposited track by track and layer by layer in order to produce a three dimensional object. This technique uses a dry fibre bundle (Figure 1.10, 1) and polymer pellets (Figure 1.10, 2) as its inputs. The pellets being used are typically thermoplastic polymers but can also be thermosetting prepolymers or vitrimers, which are being compressed, liquified and blended inside a micro extruder (Figure 1.10, 3). The extruder feeds the liquified resin into a chamber (Figure 1.10, 4), through which the fibre bundle is pulled by a puller mechanism (Figure 1. 10, 6) in order to impregnate it with the polymer. This impregnation process can be assisted through the use of passive or active impregnation pins (Figure 1. 10, 5), which will be elaborately discussed in Chapter 2. Polymer flow is restricted by a pultrusion die (also called stripper die or wipe-off die, Figure 1. 10, 6) when the formed composite strand exits the polymer chamber. Subsequently, the puller mechanism (Figure 1. 10, 7) feeds the composite strand through a heated nozzle (Figure 1. 10, 8), ready for deposition on a build platform (Figure 1. 10, 9) in order to form a three-dimensional object. The EFAM process will be segmented into three different stages throughout the course of this dissertation. In the first stage, impregnation takes place, the second stage pulls the fibre bundle through the liquid polymer chamber and the pushes it towards a heated nozzle. The third stage comprises the deposition of the composite strand, using the heated nozzle.

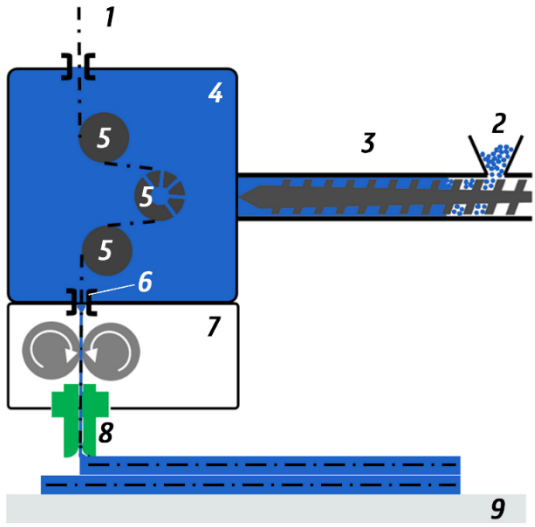

Figure 1.10: Schematic representation of the Endless fibre additive manufacturing process.

1.5.3 EFAM deposition technique compared to similar technologies

When a comparison is made between EFAM and prepreg based technologies such as ATL or AFP, or more recent technologies like Mark's method, the major difference is that the EFAM-process does not start from prepreg composite material, which gives more flexibility when it comes to matrix and fibre material selection. Also, by changing the diameter of the pultrusion die, the composite 's fibre volume fraction can be altered.

The advantage of combining impregnation and deposition in one process, compared to two discrete processes in ATL, AFP and Mark's technique, is threefold. Firstly, avoiding an extra production step has an economical advantage. Also, melt impregnation is a more economical way of producing composite strands or tapes, since it does not need the costly powder infiltration step, typically used during the production of prepreg tapes, as described by Marissen et al. [6]. Melt impregnation uses readily available polymer pellets as its input.

Secondly, there is potentially also an ecological advantage to the use of EFAM compared to prepreg-based techniques, since the EFAM composite strand needs only limited reheating between the subsequent impregnation and deposition processes.

This residual thermal energy is lost when prepregs are produced separately. However, the ecological impact of this assumption was not quantified.

Thirdly, due to beforementioned residual heat during EFAM production, the composite strand is subjected to smaller temperature changes in time, which will result in a more even temperature distribution over the cross-section of the impregnated fibre bundle during the deposition process. This minimizes thermally induced stresses and deformations upon solidification of the deposited composite material. In prepreg-based deposition techniques, a fast heating of the prepreg from ambient temperature to a processable state is performed by for example a high-power laser, a stream of hot air or nitrogen. This sudden heating induces local temperature overshoot and thermal degradation at the tape's surface [74].

Two possible disadvantages of the EFAM process compared to processes starting from prepreg material is a possible lower quality of the produced composite tape or strand, affecting the final (mechanical) properties of the composite. Further, the velocity at which the impregnation process takes place is equal to the deposition velocity in an EFAM process. Depending on the dynamics of the AM platform during deposition, accelerations of the composite strand could - but not necessarily would - have an effect on the impregnation process.

Compared with other in-printhead melt impregnation techniques (cf. Paragraph 1.4.2), EFAM uses impregnation pins, which will be elaborately discussed in Chapter 2. These pins improve the impregnation quality of the composite strand and improve fibre distribution and dispersion within the matrix material. Also the prepreg-based technique by Mark et al. suffers from limited impregnation quality, as seen in the work by Lozada et al. [39]. Additionally, the matrix material in EFAM can be supplied in the industrially accepted form of pellets, rather than the filament form in most other emerging melt impregnation technologies.

Further, this research focusses on engineering materials as a matrix material, such as PA12. The majority of the techniques mentioned in Table 1.2 use PLA as a matrix material, which only has a limited relevance in composite industry. Also, the reported fibre volume fractions are often low compared to the value of 40 vol% that will be pursued in EFAM (cf. Section 1.7).

For research purposes, the EFAM technology was only tested in 2.5D deposition, at this moment. However, the adaptation to full 3D deposition could be easily made by means of robotic arms with an EFAM deposition head mounted as its end effector. This full 3D approach is currently being used in the industry-adopted ATL and AFP techniques.

1.6 AIM AND OBJECTIVES

The scope of this research is the development of a complete process for in-line melt impregnation of an endless fibre bundle with a thermoplastic polymer and subsequent additive manufacturing process, laying-up the composite strand into a three dimensional object. All necessary boundary conditions enabling this, will be set throughout this work. Important relationships between processing parameters, the composite's morphology and its mechanical properties will be mapped and explained. Similarities and differences in the behaviour of additively manufactured composites and their conventionally produced or idealised counterparts will be analysed.

The complete research can be divided into three main challenges:

i) **Impregnation of a fibre bundle with a relevant linear density in order to obtain a composite strand, preferably having a fibre volume fraction of at least 40 vol% and a satisfactory fibre distribution and dispersion in the matrix;**

ii) **Handling of a composite strand without excessive fibre failure and its deposition in a fully automated AM process;**

iii) **Deposition of multiple layers with sufficient intra- and inter-layer adhesion and limited void fraction, in order to produce three-dimensional composite parts with good repeatability and decent mechanical properties.**

As will be discussed more in detail in Section 1.7, these three main challenges will be countered in Chapter 2, 3 and 4. All technical difficulties which were encountered during the complete process development within this research are documented, solutions and possible ways for process optimisation are proposed, and were in several cases also implemented and tested.

To give an indication of the technological maturity of the EFAM technology, being under development, 'Technology readiness levels' (TRL) can be used. These were introduced by the National Aeronautics and Space Administration (NASA, Washington D.C., United States of America). In this, a TRL 1 corresponds with the initial conceptualisation of a technology. The technology 's maturity can increase up to TRL 9, indicating a fully operational technology (Figure 1.11). A complete 'technology readiness assessment' (TRA) is not within the scope of this work, but it can be said that the aimed TRL is to conduct a **feasibility study of the EFAM process** (TRL 3) **and further development for the process** so that a simple demonstrator part can be produced (TRL 5).

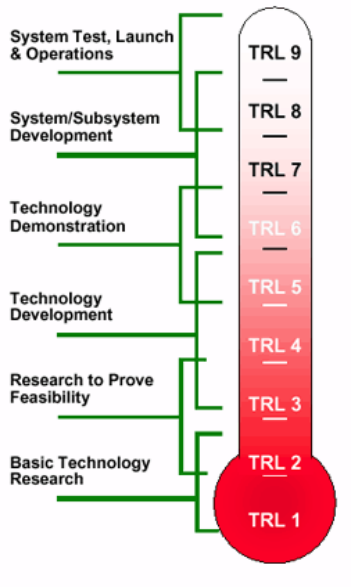

Figure 1.11: Indicator for technology readiness level by National Aeronautics and Space Administration (Washington D.C, United States of America).

1.7 OVERVIEW OF THE MANUSCRIPT

In Chapter 1, an overview of different processes for additive manufacturing of endless fibre composites was given and their performance was compared. Further, the workflow of the complete EFAM process was introduced as a three stage process within the EFAM deposition head. The innovative aspects, envisaged advantages and possible disadvantages of this new technique were reviewed and the technology was compared to currently emerging and existing (automated) composite lay-up technologies. The main aims and objectives of this research were discussed, mainly from a material science perspective, but also from a more general, ecological, economical, and societal point of view.

Chapter 2 will focus on the first stage of the EFAM process, i.e. the impregnation procedure (Figure 2.12). Impregnation behaviour is approached from a theoretical point of view and all parameters influencing it will be mapped and taken into account in the design of an automated impregnation device. Pultrusion forces, attainable shear rates on the polymer, etc. will be modelled. Three methods for melt-impregnation of endless fibre bundles with a thermoplastic polymer will be proposed and evaluated for impregnation quality, morphology and fracture mechanisms.

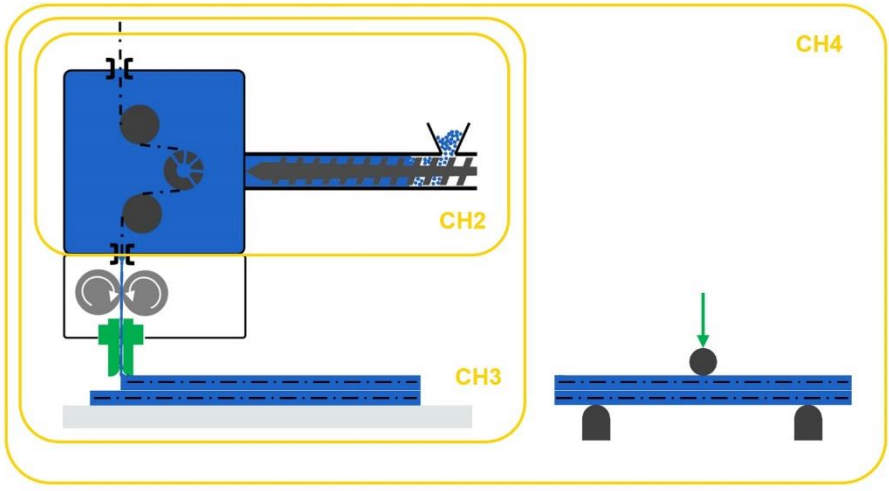

Figure 1.12: Schematic representation of the main focus of Chapters 2 to 4.

An impregnation device, as described in Chapter 2, can be mounted on an AM platform to be able to perform automated lay-up of thermoplastic composite material. Chapter 3 will briefly discuss the main characteristics of this platform, which was developed in-house through the course of this research. Further in Chapter 3, all necessary conditions of both hard- and software to successfully perform the second stage, i.e. to pull the composite through the pultrusion die and to push it through the heated nozzle, and the third stage: to deposit the composite, will be discussed (Figure 2.12). There will be a strong focus on the link between processing parameters and the morphology of the resulting composite specimens. The main goal of Chapter 3 is to find the optimal settings to deposit multiple layers of composite material with a limited amount of voids and a decent fibre distribution and dispersion.

Chapter 4 will discuss the relation between the processing parameters layer thickness and nozzle temperature, their effect on composite morphology and on mechanical properties such as flexural properties and fracture mechanisms. The obtained materials and their properties will be compared to composites produced using different emerging technologies.

Chapter 5 will summarise all important findings of this research and will check to which extend all aims and objectives were met. To end with, necessary means to increase the technology readiness level for the EFAM technique will be proposed and interesting topics for future research, such as the optimisation of interlayer adhesion, full 3D deposition of composite material, advanced software for optimising part manufacturing and tool-path generation will be briefly described.

1.8 REFERENCES

[1] I. Gibson, D. W. Rosen, and B. Stucker, *Additive Manufacturing Technologies, Springer (2010)*. 2014.

[2] D. H. J. A. Lukaszewicz and K. D. Potter, "The internal structure and conformation of prepreg with respect to reliable automated processing," *Compos. Part A Appl. Sci. Manuf.*, vol. 42, no. 3, pp. 283–292, 2011.

[3] W. D. Callister and D. G. Rethwisch, *Materials Science and Engineering 9th Edition*. 2014.

[4] L. Monette, M. P. Anderson, and G. S. Grest, "The meaning of the critical length concept in composites: Study of matrix viscosity and strain rate on the average fiber fragmentation length in short-fiber polymer composites," *Polym. Compos.*, vol. 14, no. 2, pp. 101–115, 1993.

[5] T. M. Llewellyn-Jones, B. W. Drinkwater, and R. S. Trask, "3D printed components with ultrasonically arranged microscale structure," *Smart Mater. Struct.*, vol. 25, no. 2, p. 02LT01, 2016.

[6] R. Marissen, L. T. Van Der Drift, and J. Sterk, "Technology for rapid impregnation of fibre bundles with a molten thermoplastic polymer," *Compos. Sci. Technol.*, vol. 60, no. 10, pp. 2029–2034, 2000.

[7] H. L. Tekinalp *et al.*, "Highly oriented carbon fiber-polymer composites via additive manufacturing," *Compos. Sci. Technol.*, vol. 105, pp. 144–150, 2014.

[8] F. Ning, W. Cong, Y. Hu, and H. Wang, "Additive manufacturing of carbon fiber-reinforced plastic composites using fused deposition modeling: Effects of process parameters on tensile properties," *J. Compos. Mater.*, 2016.

[9] B. G. Compton, B. K. Post, C. E. Duty, L. Love, and V. Kunc, "Thermal analysis of additive manufacturing of large-scale thermoplastic polymer composites," *Addit. Manuf.*, vol. 17, pp. 77–86, 2017.

[10] R. T. L. Ferreira, I. C. Amatte, T. A. Dutra, and D. Bürger, "Experimental characterization and micrography of 3D printed PLA and PLA reinforced with short carbon fibers," *Compos. Part B Eng.*, vol. 124, pp. 88–100, 2017.

[11] J. R. Raney, B. G. Compton, J. Mueller, T. J. Ober, K. Shea, and J. A. Lewis, "Rotational 3D printing of damage-tolerant composites with programmable mechanics," *Proc. Natl. Acad. Sci. U. S. A.*, vol. 115, no. 6, pp. 1198–1203, 2018.

[12] V. Kishore *et al.*, "Infrared preheating to improve interlayer strength of big area additive manufacturing (BAAM) components," *Addit. Manuf.*, vol. 14, pp. 7–12, 2017.

[13] B. Brenken, E. Barocio, A. Favaloro, V. Kunc, and R. B. Pipes, "Fused filament fabrication of fiber-reinforced polymers: A review," *Addit. Manuf.*, vol. 21, no. October 2017, pp. 1–16, 2018.

[14] N. G. Karsli and A. Aytac, "Tensile and thermomechanical properties of short carbon fiber reinforced polyamide 6 composites," *Compos. Part B Eng.*, vol. 51, pp. 270–275, 2013.

[15] W. Zhong, F. Li, Z. Zhang, L. Song, and Z. Li, "Short fiber reinforced composites for fused deposition modeling," *Mater. Sci. Eng. A301*, vol. 301, pp. 125–130, 2001.

[16] W. Zhang *et al.*, "Interfacial bonding strength of short carbon fiber/acrylonitrile-butadiene-styrene composites fabricated by fused deposition modeling," *Compos. Part B Eng.*, vol. 137, no. October 2017, pp. 51–59, 2018.

[17] S.-Y. Fu, B. Lauke, E. Mäder, C.-Y. Yue, and X. Hu, "Tensile properties of short-glass-fiber-and short-carbon-fiber-reinforced polypropylene composites," *Compos. Part A Appl. Sci. Manuf.*, vol. 31, no. 10, pp. 1117–1125, 2000.

[18] B. G. Compton and J. A. Lewis, "3D-printing of lightweight cellular composites," *Adv. Mater.*, vol. 26, no. 34, pp. 5930–5935, 2014.

[19] H. Bijsterbosch and R. J. Gaymans, "Impregnation of glass rovings with a polyamide melt. Part 2: Wipe-off die," *Compos. Manuf.*, vol. 4, no. 3, pp. 133–137, 1993.

[20] S. Kumar and J. P. Kruth, "Composites by rapid prototyping technology," *Mater. Des.*, vol. 31, no. 2, pp. 850–856, 2010.

[21] D. H. J. A. Lukaszewicz, C. Ward, and K. D. Potter, "The engineering aspects of automated prepreg layup: History, present and future," *Compos. Part B Eng.*,

vol. 43, no. 3, pp. 997–1009, 2012.

[22] Z. Qureshi, T. Swait, R. Scaife, and H. M. El-Dessouky, “In situ consolidation of thermoplastic prepreg tape using automated tape placement technology: Potential and possibilities,” *Compos. Part B Eng.*, vol. 66, pp. 255–267, 2014.

[23] B. Z. Jang, E. Ma, and C. J. Wang, “Apparatus and Process for Producing Fiber Reinforced Composite Objects,” no. 19, 1999.

[24] Mark, “US20150266243A1.pdf,” 2015.

[25] G. D. Goh *et al.*, “Characterization of mechanical properties and fracture mode of additively manufactured carbon fiber and glass fiber reinforced thermoplastics,” *Mater. Des.*, vol. 137, pp. 79–89, 2018.

[26] F. Van Der Klift, Y. Koga, A. Todoroki, M. Ueda, and Y. Hirano, “3D Printing of Continuous Carbon Fibre Reinforced Thermo-Plastic (CFRTP) Tensile Test Specimens,” *Open J. Compos. Mater.*, vol. 6, no. January, pp. 18–27, 2016.

[27] G. Chabaud, M. Castro, C. Denoual, and A. Le Duigou, “Hygromechanical properties of 3D printed continuous carbon and glass fibre reinforced polyamide composite for outdoor structural applications,” *Addit. Manuf.*, vol. 26, no. January, pp. 94–105, 2019.

[28] G. W. Melenka, B. K. O. Cheung, J. S. Schofield, M. R. Dawson, and J. P. Carey, “Evaluation and prediction of the tensile properties of continuous fiber-reinforced 3D printed structures,” *Compos. Struct.*, vol. 153, pp. 866–875, 2016.

[29] H. Mei, Z. Ali, Y. Yan, I. Ali, and L. Cheng, “Influence of mixed isotropic fiber angles and hot press on the mechanical properties of 3D printed composites,” *Addit. Manuf.*, vol. 27, no. March, pp. 150–158, 2019.

[30] K. Agarwal, S. K. Kuchipudi, B. Girard, and M. Houser, “Mechanical properties of fiber reinforced polymer composites: A comparative study of conventional and additive manufacturing methods,” *J. Compos. Mater.*, vol. 52, no. 23, pp. 3173–3181, 2018.

[31] A. N. Dickson, J. N. Barry, K. A. McDonnell, and D. P. Dowling, “Fabrication of continuous carbon, glass and Kevlar fibre reinforced polymer composites using additive manufacturing,” *Addit. Manuf.*, vol. 16, pp. 146–152, 2017.

[32] L. Pyl, K. A. Kalteremidou, and D. Van Hemelrijck, “Exploration of specimen geometry and tab configuration for tensile testing exploiting the potential of 3D printing freeform shape continuous carbon fibre-reinforced nylon matrix composites,” *Polym. Test.*, vol. 71, no. September, pp. 318–328, 2018.

[33] Y. Peng, Y. Wu, K. Wang, G. Gao, and S. Ahzi, “Synergistic reinforcement of polyamide-based composites by combination of short and continuous carbon fibers via fused filament fabrication,” *Compos. Struct.*, vol. 207, no. September 2018, pp. 232–239, 2019.

[34] M. Araya-Calvo *et al.*, “Evaluation of compressive and flexural properties of continuous fiber fabrication additive manufacturing technology,” *Addit. Manuf.*, vol. 22, no. May, pp. 157–164, 2018.

[35] M. A. Caminero, J. M. Chacón, I. García-Moreno, and G. P. Rodríguez, “Impact damage resistance of 3D printed continuous fibre reinforced thermoplastic composites using fused deposition modelling,” *Compos. Part B Eng.*, vol. 148, no. April, pp. 93–103, 2018.

[36] M. A. Caminero, J. M. Chacón, I. García-Moreno, and J. M. Reverte, “Interlaminar bonding performance of 3D printed continuous fibre reinforced thermoplastic composites using fused deposition modelling,” *Polym. Test.*, vol. 68, no. April, pp. 415–423, 2018.

[37] M. Mohammadizadeh, A. Imeri, I. Fidan, and M. Elkelany, “3D printed fiber reinforced polymer composites - Structural analysis,” *Compos. Part B Eng.*, vol. 175, no. April, p. 107112, 2019.

[38] L. Pyl, K. A. Kalteremidou, and D. Van Hemelrijck, “Exploration of the design freedom of 3D printed continuous fibre-reinforced polymers in open-hole tensile strength tests,” *Compos. Sci. Technol.*, vol. 171, no. November 2018, pp. 135–151, 2019.

[39] J. Naranjo-Lozada, H. Ahuett-Garza, P. Orta-Castañón, W. M. H. Verbeeten, and D. Sáiz-González, “Tensile properties and failure behavior of chopped and continuous carbon fiber composites produced by additive manufacturing,” *Addit. Manuf.*, vol. 26, no. January, pp. 227–241, 2019.

[40] N. van de Werken, J. Hurley, P. Khanbolouki, A. N. Sarvestani, A. Y. Tamijani, and M. Tehrani, “Design considerations and modeling of fiber reinforced 3D

printed parts," *Compos. Part B Eng.*, vol. 160, pp. 684–692, Mar. 2019.

[41] J. Frketic, T. Dickens, and S. Ramakrishnan, "Automated manufacturing and processing of fiber-reinforced polymer (FRP) composites: An additive review of contemporary and modern techniques for advanced materials manufacturing," *Addit. Manuf.*, vol. 14, pp. 69–86, 2017.

[42] S. T. Jespersen, M. D. Wakeman, V. Michaud, D. Cramer, and J. A. E. Månson, "Film stacking impregnation model for a novel net shape thermoplastic composite preforming process," *Compos. Sci. Technol.*, vol. 68, no. 7–8, pp. 1822–1830, 2008.

[43] J. M. Gardner *et al.*, "3-D printing of multifunctional carbon nanotube yarn reinforced components," *Addit. Manuf.*, vol. 12, pp. 38–44, 2016.

[44] A. J. Comer *et al.*, "Mechanical characterisation of carbon fibre-PEEK manufactured by laser-assisted automated-tape-placement and autoclave," *Compos. Part A Appl. Sci. Manuf.*, vol. 69, pp. 10–20, 2015.

[45] C. M. Stokes-Griffin and P. Compston, "Optical characterisation and modelling for oblique near-infrared laser heating of carbon fibre reinforced thermoplastic composites," *Opt. Lasers Eng.*, vol. 72, pp. 1–11, 2015.

[46] D. M. Corbridge, L. T. Harper, D. S. A. De Focatiis, and N. A. Warrior, "Compression moulding of composites with hybrid fibre architectures," *Compos. Part A Appl. Sci. Manuf.*, vol. 95, pp. 87–99, 2017.

[47] H. Huang and R. Talreja, "Effects of void geometry on elastic properties of unidirectional fiber reinforced composites," *Compos. Sci. Technol.*, vol. 65, no. 13, pp. 1964–1981, 2005.

[48] H. Bijsterbosch and R. J. Gaymans, "Polyamide 6 - long glass fiber injection moldings," *Polym. Compos.*, vol. 16, no. 5, pp. 363–369, 1995.

[49] P. Bettini, G. Alitta, G. Sala, and L. Di Landro, "Fused Deposition Technique for Continuous Fiber Reinforced Thermoplastic," *J. Mater. Eng. Perform.*, vol. 26, no. 2, pp. 843–848, 2017.

[50] R. Matsuzaki *et al.*, "Three-dimensional printing of continuous-fiber composites by in-nozzle impregnation.," *Sci. Rep.*, vol. 6, no. February, p. 23058, 2016.

[51] W. Ye *et al.*, "Separated 3D printing of continuous carbon fiber reinforced thermoplastic polyimide," *Compos. Part A Appl. Sci. Manuf.*, vol. 121, no. April, pp. 457–464, 2019.

[52] M. Luo, X. Tian, J. Shang, W. Zhu, D. Li, and Y. Qin, "Impregnation and interlayer bonding behaviours of 3D-printed continuous carbon-fiber-reinforced poly-ether-ether-ketone composites," *Compos. Part A Appl. Sci. Manuf.*, vol. 121, no. March, pp. 130–138, 2019.

[53] H. Zhang, D. Yang, and Y. Sheng, "Performance-driven 3D printing of continuous curved carbon fibre reinforced polymer composites: A preliminary numerical study," *Compos. Part B Eng.*, vol. 151, no. June, pp. 256–264, 2018.

[54] B. Akhoundi, A. H. Behravesh, and A. Bagheri Saed, "Improving mechanical properties of continuous fiber-reinforced thermoplastic composites produced by FDM 3D printer," *J. Reinf. Plast. Compos.*, vol. 38, no. 3, pp. 99–116, 2019.

[55] C. Yang, X. Tian, T. Liu, Y. Cao, and D. Li, "3D printing for continuous fiber reinforced thermoplastic composites: Mechanism and performance," *Rapid Prototyp. J.*, vol. 23, no. 1, pp. 209–215, 2017.

[56] N. Li, Y. Li, and S. Liu, "Rapid prototyping of continuous carbon fiber reinforced polylactic acid composites by 3D printing," *J. Mater. Process. Technol.*, vol. 238, pp. 218–225, 2016.

[57] X. Tian, T. Liu, C. Yang, Q. Wang, and D. Li, "Interface and performance of 3D printed continuous carbon fiber reinforced PLA composites," *Compos. Part A Appl. Sci. Manuf.*, vol. 88, pp. 198–205, 2016.

[58] Z. Hou, X. Tian, J. Zhang, and D. Li, "3D printed continuous fibre reinforced composite corrugated structure," *Compos. Struct.*, vol. 184, no. October 2017, pp. 1005–1010, 2018.

[59] S. Liu, Y. Li, and N. Li, "A novel free-hanging 3D printing method for continuous carbon fiber reinforced thermoplastic lattice truss core structures," *Mater. Des.*, vol. 137, pp. 235–244, 2018.

[60] M. Saari, B. Cox, E. Richer, P. S. Krueger, and A. L. Cohen, "Fiber encapsulation additive manufacturing: An enabling technology for 3D printing of

electromechanical devices and robotic components," *3D Print. Addit. Manuf.*, vol. 2, no. 1, pp. 32–39, 2015.

[61] B. Cox, M. Saari, B. Xia, E. Richer, P. S. Krueger, and A. L. Cohen, "Fiber Encapsulation Additive Manufacturing: Technology and Applications Update," vol. 00, no. 00, pp. 3–6, 2016.

[62] C. Luan, X. Yao, C. Liu, L. Lan, and J. Fu, "Self-monitoring continuous carbon fiber reinforced thermoplastic based on dual-material three-dimensional printing integration process," *Carbon N. Y.*, vol. 140, pp. 100–111, 2018.

[63] M. Heidari-Rarani, M. Rafiee-Afarani, and A. M. Zahedi, "Mechanical characterization of FDM 3D printing of continuous carbon fiber reinforced PLA composites," *Compos. Part B Eng.*, vol. 175, no. June, p. 107147, 2019.

[64] K.-I. Mori, T. Maeno, and Y. Nakagawa, "Dieless forming of carbon fibre reinforced plastic parts using 3D printer," *Procedia Eng.*, vol. 81, no. October, pp. 1595–1600, 2014.

[65] A. V. Azarov *et al.*, "Development of a two-matrix composite material fabricated by 3D printing," *Polym. Sci. - Ser. D*, vol. 10, no. 1, pp. 87–90, 2017.

[66] F. Baumann, J. Scholz, and J. Fleischer, "Investigation of a New Approach for Additively Manufactured Continuous Fiber-reinforced Polymers," *Procedia CIRP*, vol. 66, pp. 323–328, 2017.

[67] X. Yao, C. Luan, D. Zhang, L. Lan, and J. Fu, "Evaluation of carbon fiber-embedded 3D printed structures for strengthening and structural-health monitoring," *Mater. Des.*, vol. 114, pp. 424–432, 2017.

[68] S. A. Hinchcliffe, K. M. Hess, and W. V. Srubar, "Experimental and theoretical investigation of prestressed natural fiber-reinforced polylactic acid (PLA) composite materials," *Compos. Part B Eng.*, vol. 95, pp. 346–354, 2016.

[69] Y. Nakagawa, K. ichiro Mori, and T. Maeno, "3D printing of carbon fibre-reinforced plastic parts," *Int. J. Adv. Manuf. Technol.*, vol. 91, no. 5–8, pp. 2811–2817, 2017.

[70] H. Brooks and S. Molony, "Design and evaluation of additively manufactured parts with three dimensional continuous fi bre reinforcement," *JMADE*, vol. 90, pp. 276–283, 2016.

[71] M. Eichenhofer, J. C. H. Wong, and P. Ermanni, "Continuous lattice fabrication of ultra-lightweight composite structures," *Addit. Manuf.*, vol. 18, pp. 48–57, 2017.

[72] A. N. Dickson and D. P. Dowling, "Enhancing the bearing strength of woven carbon fibre thermoplastic composites through additive manufacturing," *Compos. Struct.*, vol. 212, no. January, pp. 381–388, 2019.

[73] N. Li *et al.*, "Path-designed 3D printing for topological optimized continuous carbon fibre reinforced composite structures," *Compos. Part B*, vol. 182, no. July 2019, p. 107612, 2020.

[74] F. O. Sonmez and M. Akbulut, "Process optimization of tape placement for thermoplastic composites," *Compos. Part A Appl. Sci. Manuf.*, vol. 38, no. 9, pp. 2013–2023, 2007.

2 MODELLING AND CHARACTERISATION OF MELT IMPREGNATION

2.1 INTRODUCTION

In this chapter, the phenomenon 'impregnation', i.e. the propagation of a fluid through a porous medium, is approached from a theoretical point of view and all influencing parameters are mapped. To this end, a mathematical definition of fibre volume fraction V_f is defined first (Paragraph 2.2). A major inhibitor during impregnation processes with thermoplastics is their high melt viscosity compared to thermosets. For this reason, the impregnation of endless fibre bundles (Figure 2.1, 1) with thermoplastics (Figure 2.1, 0) in conventional composite processing processes occurs at elevated temperature and under high pressure, e.g. through compression moulding. In Paragraph 2.7, it will become clear that with the aid of 'spreader pins', also called 'impregnation pins' (Figure 2.1, 3) in a liquid polymer chamber (Figure 2.1, 4), a local high pressure can be generated in a low-pressure environment. This can eliminate the need for high strength and heavy tooling and allows for a continuous impregnation process, suited for use in the first stage of an EFAM process.

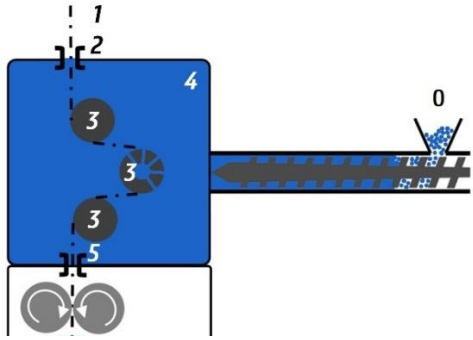

Figure 2.1: Schematic representation of the pultrusion process. Fibre bundle (1), fibre inlet (2), impregnation pins (3), liquid polymer chamber (4) and fibre outlet (5).

The necessary machine parameters of such an impregnation device, being the diameter of the fibre inlet (Figure 2.1, 2) and outlet (Figure 2.1, 5) are calculated in Paragraph 2.4 and 2.6, based on the definition of V_f. The boundary condition of the

minimal applicable fibre bending radius to avoid fibre failure throughout the complete process is determined in Paragraph 2.5. Pultrusion forces, pressures and attainable shear rates in the polymer, etc. are modelled in Paragraphs 2.7 and 2.8. In Paragraph 2.9, three different techniques for melt impregnation are tested and assessed for impregnation quality, morphology and fracture mechanisms. These results were partially published in 'Polymer Engineering & Science' [1]. Finally, the fully automated impregnation device, which was conceived, designed, produced, tested and optimised within this research, is presented in Paragraph 2.10.

2.2 COMPOSITE VOLUME AND MASS FRACTIONS

There is a proportional trend between the volume fraction of a filler (endless fibres throughout the course of this research) and the mechanical properties of a composite (cf. Chapter 4). Generally, the volume fraction of each component can be defined as the ratio of the individual component's volume v_i to the composite's volume v_c. The sum of all n components' volume fractions V_i in a composite is equal to unity (Equation 2.1). In a single matrix and fibre composite, the fibre volume fraction is specified as V_f. Except for a small void volume fraction V_v, the remaining volume is taken by the matrix, specified as the matrix volume fraction V_m. These three volume fractions can be calculated as the ratio of their respective volumes v_f, v_m, v_v and the composite's total volume v_c (Equation 2.2).

$$\begin{cases} V_i = \dfrac{v_i}{v_c} \\ \displaystyle\sum_{i=1}^{n} V_i = 1 \end{cases} \tag{2.1}$$

$$\begin{cases} V_f = \dfrac{v_f}{v_c} \\ V_m = \dfrac{v_m}{v_c} \\ V_v = \dfrac{v_v}{v_c} \\ V_f + V_m + V_v = 1 \end{cases} \tag{2.2}$$

v_c	Composite volume	[m³]
v_f	Filler volume	[m³]
v_i	Volume of component i	[m³]
v_m	Matrix volume	[m³]
v_v	Void volume	[m³]
V_f	Filler volume fraction	[/]
V_i	Volume fraction of component i	[/]
V_m	Matrix volume fraction	[/]
V_v	Void volume fraction	[/]

Although it is more intuitive to design a composite for strength and stiffness using volume fractions, a more practical manner is to work with mass fractions, since those are easier to measure during production and quality control. Analogous to volume fraction calculations, mass fractions can be calculated using Equations 2.3 and 2.4:

$$\begin{cases} M_i = \dfrac{m_i}{m_c} \\ \displaystyle\sum_{i=1}^{n} M_i = 1 \end{cases} \tag{2.3}$$

$$\begin{cases} M_f = \dfrac{m_f}{m_c} \\ M_m = \dfrac{m_m}{m_c} \\ M_v = \dfrac{m_v}{m_c} \\ M_f + M_m + M_v = 1 \end{cases} \tag{2.4}$$

m_c	Composite mass	[kg]
m_f	Filler mass	[kg]
m_i	Mass of component i	[kg]
m_m	Matrix mass	[kg]
m_v	Void mass	[kg]
M_f	Filler mass fraction	[/]
M_i	Mass fraction of component i	[/]
M_m	Matrix mass fraction	[/]
M_v	Void mass fraction	[/]

In order to keep the intuitiveness of the use of volume fractions and the ease of mass fractions, mass fractions obtained in matrix incineration/dissolving experiments (Equation 2.4) can be transformed into volume fractions. Filling in the density law (Equation 2.5) in Equation 2.4 (M_f) yields Equation 2.6:

$$m_i = v_i \, \rho_i \tag{2.5}$$

$$M_f = \frac{m_f}{m_c} = \frac{v_f}{v_c} \frac{\rho_f}{\rho_c} = V_f \frac{\rho_f}{\rho_c} \tag{2.6}$$

m_i	Mass of component i	[kg]
ρ_c	Density of the composite	[kg/m³]
ρ_i	Density of component i	[kg/m³]
v_i	Volume of component i	[m³]

The composite's density ρ_c can be written as a volume fraction-weighted average of its components' densities:

$$\rho_c = V_f \, \rho_f + V_m \, \rho_m + V_v \, \rho_v \tag{2.7}$$

Equations 2.2, 2.6 and 2.7 can be combined to form Equation 2.8:

$$M_f = V_f \, \frac{\rho_f}{V_f \, \rho_f + (1 - V_f - V_v) \, \rho_m + V_v \, \rho_v} \tag{2.8}$$

Solving Equation 2.8 for V_f yields:

$$V_f = \frac{\rho_m \, M_f \, (1 - V_v) + \rho_v \, V_v \, M_f}{\rho_f \, + \, M_f \, (\rho_m \, - \, \rho_f)} \tag{2.9}$$

V_v can be measured by optical microscopy on a composite cross-section or by using micro-tomography, as reviewed by Du Plessis et al. [2] and performed in previous research on AM produced samples [3]. The term '$\rho_v \, V_v$' in Equations 2.7 to 2.9 can usually be neglected since ρ_v is typically a factor 10^{-3} smaller than ρ_f and ρ_m, and typical values for V_v are less than 10^{-2}. In practice (assuming a composite with

limited V_v), Equation 2.10 is an accurate approximation of V_f and can be determined by basic incineration/dissolving experiments and mass and density measurements.

$$\begin{cases} M_f = \dfrac{m_f}{m_c} \\ V_f = \dfrac{\rho_m \, M_f}{\rho_f \, + \, M_f \left(\rho_m \, - \, \rho_f\right)} \end{cases} \tag{2.10}$$

m_c	Composite mass	[kg]
m_f	Filler mass	[kg]
M_f	Filler mass fraction	[/]
ρ_f	Filler density	[kg/m³]
ρ_m	Matrix density	[kg/m³]
V_f	Filler volume fraction	[/]

2.3 IMPREGNATION OF UNIDIRECTIONAL FIBRES

The one-dimensional propagation of a Newtonian fluid through a porous medium was modelled by Darcy and can be used to describe a flow through aligned fibres [4], [5]. The permeability number K in this model was empirically determined by Darcy and is highly dependent of the porous medium (Equation 2.11). From this equation it can be deduced that the mean propagation velocity of the fluid is proportional to the permeability of the medium and the pressure gradient applied on the system. On the other hand, a higher viscosity will result in a slower flow through the medium.

$$v = -\frac{K}{\eta} \frac{dP}{dx} \tag{2.11}$$

K	Darcy permeability	[m²]
η	Dynamic viscosity of the polymer	[Pas]
v	Mean propagation velocity of the fluid through a medium	[m/s]
$\frac{dP}{dx}$	Pressure gradient in the flow direction	[Pa/m]

Kozeny and Carman further refined the definition of the permeability number by incorporating the Kozeny constant k (Equation 2.12), which takes into account the tortuosity K_t and the non-uniformity of the pores K_0 [6], however only for isotropic porous structures. The tortuosity K_t is the ratio of the actual travel length L_e of a fluid through the medium and the distance along the flow direction L (Equation 2.12, Figure 2.2). Gutowski et al. and Nygard et al. extended this model for structures with highly anisotropic pores, such as aligned fibres, and took the fibres' elasticity into account [7], [8]. For a flow parallel to the fibre direction, the tortuosity approaches unity due to the straight, prismatic cavities present in between the individual fibres. This results in a maximal permeability and fluid propagation for a longitudinal flow. The tortuosity is larger for a perpendicular flow, consequently, permeability and fluid propagation velocity are lower. The tortuosity of a porous medium is highly dependent on the fibre stacking and on the fibre volume fraction [6]. As a consequence, Kozeny "constants" were proven not to be constant with varying fibre volume fractions, especially for low and high values of V_f [9]. In recent research, Kozeny constants are often determined empirically or by numeric analyses [5], [6], [9]–[14]. Also, Williams et al. showed that actual flow rates were higher than predicted in models with square or hexagonal close packed fibre distribution, due to non-uniform distribution of fibres during experiments [15]. These non-uniformities can be partly attributed to the occurrence of fibre twist in commercially available fibre materials.

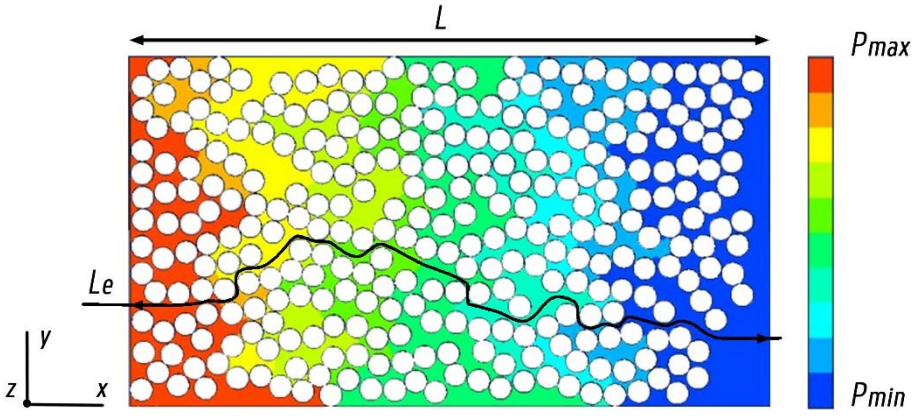

Figure 2.2: Pressure gradient applied onto a PA12 polymer melt, impregnating a fibre bundle. Cross-section perpendicular to the fibre direction.

$$\begin{cases} K = \dfrac{r_f^2}{4k}\,\dfrac{(1-V_f)^3}{V_f^2} \\ k = K_0 K_l^2 \\ K_l = \dfrac{L_e}{L} \end{cases} \tag{2.12}$$

k	Kozeny constant	[/]
K	Darcy permeability	[m²]
K_0	Shape factor	[/]
K_l	Tortuosity of the packing structure	[/]
L	Shortest distance along flow direction	[m]
L_e	Effective fluid travel length	[m]
r_f	Fibre radius	[m]
V_f	Fibre volume fraction	[/]

In Equation 2.11, the viscosity is considered to be independent of the fluid velocity, which is only a conservative approximation for thermoplastic flows, due to their shear-thinning properties [16]. Pascal and co-workers empirically adapted Darcy's law for application with power-law fluids, e.g. liquid polymers [13], [17]–[19] (Equation 2.13). Note that the local velocity of the liquid material in between the fibres can be much higher than the propagation velocity.

$$v = -\left(\frac{K}{\eta}\,\frac{dP}{dx}\right)^{\frac{1}{n}} \tag{2.13}$$

K	Darcy permeability	[m²]
η	Dynamic viscosity of the polymer	[Pa.s^n]
n	Consistency index	[/]
v	superficial velocity of the fluid	[m/s]
$\frac{dP}{dx}$	Pressure gradient in the flow direction	[Pa/m]

Throughout this study, the polymer's shear viscosity will be of paramount importance since it will impede a polymer from flowing through a fibre bundle. The

polymer's shear viscosity is reduced at elevated temperature as a consequence of the polymer's inverse viscosity-temperature dependence, described by an Arrhenius equation (Equation 2.14) [20]. By using externally heated spreader pins, it is possible to locally reduce the polymer's shear viscosity to improve impregnation. As an additional advantage, these spreader pins also spread out the fibre bundle, reducing the impregnation distance (Figure 2.3).

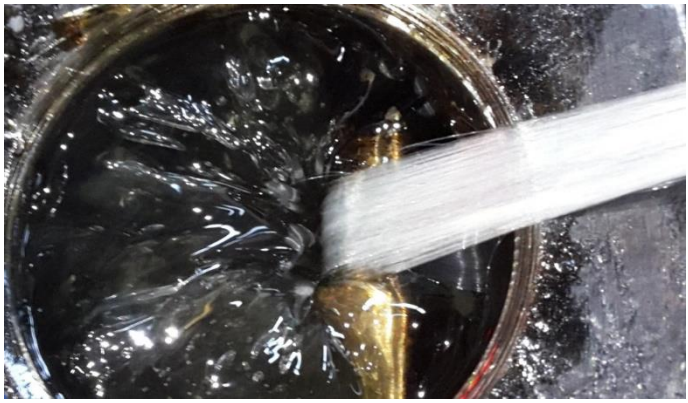

Figure 2.3: A fibre bundle is spread thanks to the spreader pin or impregnation pin.

$$\eta_1 = \eta_0 \, e^{\frac{E}{R}\left(\frac{1}{T_1} - \frac{1}{T_0}\right)} \tag{2.14}$$

E	Activation energy	[J/mol]
η_0	Dynamic viscosity of the polymer measured at T_0	[Pa.s]
η_1	Dynamic viscosity of the polymer measured at T_1	[Pa.s]
R	Gas constant	[J/mol.K]
T_0	Fluid temperature 0	[K]
T_1	Fluid temperature 1	[K]

Michaud et al. described capillary phenomena during an impregnation process, which are caused by physical and chemical interactions between the matrix, filler and atmosphere. For polymeric matrices, capillary drop values tend to be low (in the kPa range) compared to for example metallic matrices (up to 1 MPa), since polymers

exhibit lower surface tensions than metals [16]. Similar results were found by Koubaa et al., who impregnated unidirectional E-glass fibres with low viscosity fluids [21]. It can be concluded that capillary drop is of limited importance for systems with polymeric matrices. Williams et al. postulated that capillary effects do affect the flow rate, however the effect showed to be small [15].

It must be noted that the translation of empirical equations such as Darcy's law into another field comes with challenges and caution must be exercised before drawing conclusions. Darcy's experiments used Newtonian fluids and took place in an environment with a fixed temperature. In the context of an impregnation process however, fibres which were not preheated before entering a liquid polymer chamber will cause the flowing matrix material to cool down, and consequently will affect the matrix's viscosity, leading to a transient impregnation process along the fibre bundle's path through the liquid polymer chamber. As an example of the process' complexity, Figure 2.4 and 2.5 show respectively glass and steel fibre bundles with a similar single fibre diameter and fibre count, impregnated with the same matrix material (PA12), under identical pressure and temperature conditions. The abovementioned higher capillary drop for metallic materials would suggest a lower impregnation degree in the steel composite. However, the void fraction in the resulting glass fibre composite is clearly higher than in the steel-based composite. This effect is possibly caused by the difference in thermal conductivity of the fibre materials.

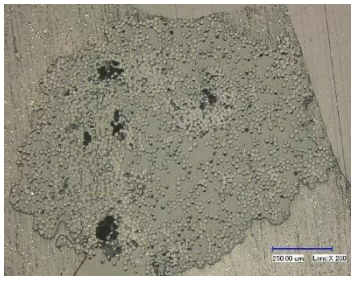

Figure 2.4: Cross-section of a glass fibre reinforced PA12.

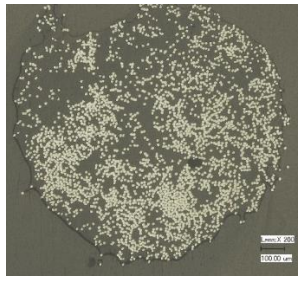

Figure 2.5: cross-section of a steel fibre reinforced PA12.

Further, pultrusion velocity might vary in the EFAM-technique, depending on the permissible velocity and acceleration rates of the AM platform. Due to this temperature and velocity field dependency, the most accurate way of predicting the impregnation flow would be by conducting coupled computational fluid dynamics

(CFD) and (thermo)mechanical finite element analyses (FEA). These iterative calculations of shear-thinning polymer flow behaviour through a deformable elastic fibre bed are computationally very intensive and have - to the author's knowledge - not yet been performed to model (spreader pin-assisted) impregnation processes.

2.4 MINIMAL DIAMETER OF FIBRE BUNDLE INLET

The fibre bundle inlet of a liquid polymer chamber is generally a circular channel with a diameter d_i and length l_i. In practice, l_i needs to be long and d_i small to realise an adequate pressure drop, more particularly to avoid polymer leakage due to impregnation pressures higher than atmospheric pressure within the liquid polymer chamber. On the other hand, d_i must be large enough to allow the fibre bundle to be pulled through the inlet without damaging the individual fibres. The minimal inlet diameter $d_{i,min}$ required to fit a fibre bundle containing N_f fibres with a mean individual fibre diameter d_f can be calculated using Equation 2.15. As an alternative for defining a bundle by N_f and d_f, it can be defined by its linear density ρ_{lin}. This is the mass of a fibre bundle per unit length and can also be used to calculate $d_{i,min}$ (Equation 2.16).

Depending on the fibre packing, a correction factor c_i should be applied. A hexagonal close packing (Figure 2.6) of the fibres will result in the densest packing c_{hcp}, and thus offer the lowest matrix/void fraction possible after impregnation. A cubic packing c_{cb} (Figure 2.7) will result in a less efficient packing and consequently in a lower fibre volume fraction and a higher matrix/void fraction. In the calculation of $d_{i,min}$, c_{hcp} should be used. In practice, the fibre bundle inlet diameter is chosen slightly larger than $d_{i,min}$ to prevent fibre failure.

$$d_{i,min} = \sqrt{\frac{N_f \, d_f^2}{c_i}} \tag{2.15}$$

$$d_{i,min} = \sqrt{\frac{4 \, \rho_{lin}}{\pi \, \rho_f \, c_i}} \tag{2.16}$$

c_i	Correction factor for packing	[/]
d_f	Single fibre diameter	[m]
$d_{i,min}$	Equivalent diameter	[m]
N_f	Fibre count	[/]
ρ_{lin}	Linear density of fibre bundle	[kg/m]
ρ_f	Density of fibre material	[kg/m³]

As shown in Figures 2.6 and 2.7, c_{hcp} and c_{cb} can be calculated as the ratio of the fibre material (blue) to the area of a unit cell (hexagonal for c_{hcp}, square for c_{cb}):

$$c_{hcp} = \frac{\frac{\pi\, d_f^2}{2}}{\sqrt{3}\, d_f^2} = \frac{\pi\sqrt{3}}{6} \approx 0.9069 \tag{2.17}$$

$$c_{cb} = \frac{\frac{\pi\, d_f^2}{4}}{d_f^2} = \frac{\pi}{4} \approx 0.7854 \tag{2.18}$$

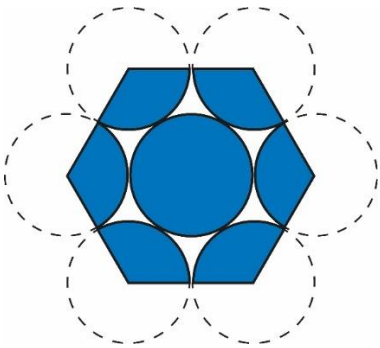

Figure 2.6: Unit cell of a hexagonal closed packing in a fibre bundle, perpendicular cross-section.

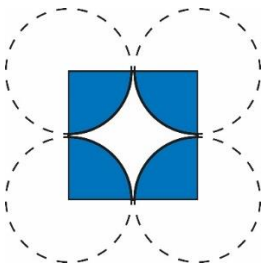

Figure 2.7: Unit cell of a square packing in a fibre bundle, perpendicular cross-section.

2.5 MINIMAL BENDING RADIUS OF A FIBRE

Consider a fibre bundle which is tensioned over a cylindrical surface and being pulled at a constant velocity, causing stresses in every individual fibre of the bundle, similar to the load case of a pultrusion process using impregnation pins. No friction between fibre and pin is assumed. Consider a single fibre which is in contact with the impregnation pin with radius R_p, and is tensioned by force F_t and bent by force F_{fl}. F_t results in a normal tensile stress σ_t, acting on the cross-section of the fibre. The force F_{fl} flexes the fibre with a bending radius R_f, causing flexural stresses σ_{fl} in the fibre. The smallest bending radius a fibre made out of an isotropic material (such as glass or annealed steel) can be subjected to without failing, will be estimated using a stress based criterion. A strain based criterion for composites subjected to a pure flexural load was proposed by Ishi et al. [22].

Tensioning the fibre will result in a pure tensile stress (+), which is constant over the complete fibre cross-section (Figure 2.8, blue). This tensile stress is calculated in Paragraph 2.5.1. Bending the fibre will result in a flexural stress (Figure 2.8, green), which comprises a tensile stress (+) in the outer part of the fibre (above dashed line on Figure 2.8) and a compressive stress (-) in the inner part (below dashed line on Figure 2.8).

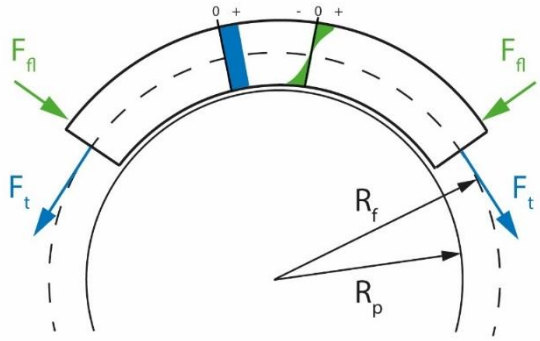

Figure 2.8: Tensile (blue) and flexural stresses (green) in a single fibre, tensioned over a pin with radius R_p.

The maximal flexural stresses are determined in Paragraph 2.5.2. Superposition of both tensile/compressive and flexural stresses will visualise the critically loaded parts in the fibre. The outer side of the fibre will always be in tension, since the total stress is the sum of positive tensile and flexural stresses at this location. The inner

side of the fibre might be subjected to tension or compression, depending on the relative magnitude of the flexural and tensile stresses, since the resulting stress is the sum of two stresses having the same direction but different orientation. The maximal allowable stress in both cases will be calculated in Paragraph 2.5.3.

2.5.1 Determination of tensile stresses in a fibre

Tensile force F_t results in a tensile stress σ_t acting on the cross-section of a fibre with diameter d_f, and can be calculated as:

$$\sigma_t = \frac{4F_t}{\pi\, d_f^2} \tag{2.19}$$

d_f	Single fibre diameter	[mm]
σ_t	tensile stress on a fibre	[MPa]
F_t	Tensile force on a fibre	[N]

2.5.2 Determination of maximal flexural stresses in a bent fibre

Consider an infinitesimally short fibre element with diameter d_f and length δl, which is loaded by a force F_{fl} in cantilever bending mode in order to wrap it around an inelastic pin with radius R_p (Figure 2.9). The bending moment M_{fl} and fibre angular rotation y' at every location x along the fibre's main axis can be calculated using the strength of materials laws in Equations 2.20 and 2.21. The second moment of area of the circular fibre cross-section I_f is given by Equation 2.22.

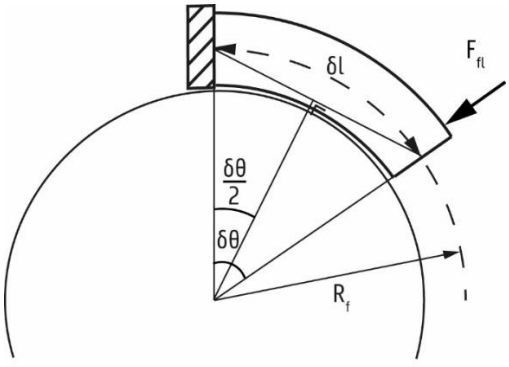

Figure 2.9: Fibre piece, bent around an inelastic pin.

$$M_{fl} = y'' \, E_f \, I_f = F_{fl} \, \delta l - F_{fl} \, x \tag{2.20}$$

$$y' \, E_f \, I_f = F_{fl} \, \delta l \, x - \frac{F_{fl} \, x^2}{2} + C_1 \tag{2.21}$$

$$I_f = \frac{\pi \, d_f^4}{64} \tag{2.22}$$

C_1	Integration constant	[Nmm²rad]
δl	Length of the fibre element	[mm]
E_f	Young's modulus of the fibre material	[N/mm²]
F_{fl}	Force acting perpendicularly on fibre end	[N]
I_f	Second moment of area of the fibre cross-section	[mm⁴]
M_{fl}	Bending moment on the fibre	[Nmm]
x	Location along fibre	[mm]
y''	Derivative of angular rotation of the fibre	[rad/mm]
y'	Angular rotation of the fibre	[rad]

At the cantilever location $x = 0$, the angular rotation of the fibre is zero, yielding:

$$y' \, (x = 0) = C_1 = 0 \Rightarrow \, C_1 = 0 \tag{2.23}$$

The fibre's angular rotation at position $x = \delta l \, /2$ is equal to $\delta\theta/2$ (Figure 2.9) and can be calculated using Equations 2.21 and 2.23:

$$y' \, (x = \frac{\delta l}{2}) = \frac{3 \, F_{fl} \, (\delta l)^2}{8 \, E_f \, I_f} \tag{2.24}$$

On Figure 2.9, one can deduce that the following relations are valid:

$$\delta l \approx \delta\theta \, R_f \tag{2.25}$$

$$\frac{\delta l}{2} \approx \frac{\delta\theta}{2} R_f \tag{2.26}$$

δl	Arc length	[mm]
R_f	Bending radius of the fibre	[mm]
$\delta\theta$	Central angle	[rad]

Combining Equations 2.24 and 2.26 yields:

$$\frac{\delta\theta}{2} \approx \frac{\delta l}{2\,R_f} \approx \frac{3\,F_{fl}\,(\delta l)^2}{8\,E_f\,I_f} \tag{2.27}$$

$$F_{fl} \approx \frac{4\,E_f\,I_f}{3\,R_f\,\delta l} \tag{2.28}$$

It can be derived from Equation 2.20, that the maximal bending moment $M_{fl,max}$ is located at the location $x = 0$ in the fibre and has a value of $F_{fl}\,\delta l$. Combining this with Equation 2.28:

$$M_{fl,max} \approx F_{fl}\,\delta l \approx \frac{4\,E_f\,I_f}{3\,R_f} \tag{2.29}$$

The flexural stress σ_{fl} in the fibre can be calculated using the bending theory:

$$\sigma_{fl} = \frac{M_{fl,max}\,d_f}{2\,I_f} \approx \frac{2\,E_f\,d_f}{3\,R_f} \tag{2.30}$$

d_f	Single fibre diameter	[mm]
E_f	Young's modulus of the fibre material	[MPa]
I_f	Second moment of area	[mm^4]
$M_{fl,max}$	Maximal bending moment	[Nmm]
R_f	Bending radius of the fibre	[mm]
σ_{fl}	Flexural stress	[MPa]

2.5.3 Determination of the minimal bending radius of a fibre

Depending on the magnitude of fibre stresses σ_t and σ_{fl}, three situations may occur. In the case that $\boldsymbol{\sigma_{fl} < \sigma_t}$, the complete fibre cross-section is subjected to tensile stresses. The outer side of a tensioned and bent fibre will be subjected to the largest equivalent normal stress, thus will be critical in the determination of $R_{f,min}$. For this load case, the tensile and flexural stress components have the same orientation and their sum should be smaller than the tensile stress of the fibre material (Equation 2.31) resulting in a minimal bending radius given in Equation 2.32.

$$\sigma_{fl} + \sigma_t < \sigma_{t,f} \tag{2.31}$$

$$R_{f,min} > \frac{2\ E_f\ d_f}{3\ (\sigma_{t,f} - \sigma_t)} \tag{2.32}$$

d_f	Single fibre diameter	[mm]
E_f	Young's modulus of the fibre material	[MPa]
$R_{f,min}$	Minimum bending radius	[mm]
σ_{fl}	Flexural stress	[MPa]
σ_t	Tensile stress applied on the fibre	[MPa]
$\sigma_{t,f}$	Tensile strength of the fibre material	[MPa]

For the load case that $\boldsymbol{\sigma_{fl} = \sigma_t}$, tensile and flexural stresses cancel each other out at the inner fibre side. At the outer fibre side, tensile and flexural stresses have the same orientation and magnitude, so Equation 2.31 is valid. The applied radius should be chosen so that σ_{fl} is less than half the fibre's tensile stress to avoid failure:

$$R_{f,min} > \frac{4\ E_f\ d_f}{3\ \sigma_{t,f}} \tag{2.33}$$

When $\boldsymbol{\sigma_{fl} > \sigma_t}$, the inner fibre side is under compression while the outer side is under tension. The tensile and compression strength of a fibre material are often dissimilar. Generally, the fibres' compression strength $\sigma_{c,f}$ is lower than their tensile strength $\sigma_{t,f}$. This is taken into account in the maximal allowable stress in the minimal bending radius estimation, so two critical conditions must be checked. At the outer fibre side, Equation 2.31 is valid. At the inner side, resulting stress must remain below $\sigma_{c,f}$ (Equation 2.34). The most stringent of these two requirements will determine $R_{f,min}$ (Equation 2.35).

$$\sigma_{fl} - \sigma_t < \sigma_{c,f} \tag{2.34}$$

$$R_{f,min} > \max\left(\frac{2\ E_f\ d_f}{3\ (\sigma_{t,f} - \sigma_t)}, \frac{2\ E_f\ d_f}{3\ (\sigma_{c,f} + \sigma_t)}\right) \tag{2.35}$$

A summary of all load cases and their critical requirements for both the inner and outer fibre side can be found in Table 2.1.

Table 2.1: Critical requirements to avoid fibre failure for three different load cases.

	$\boldsymbol{\sigma_{fl} < \sigma_t}$	$\boldsymbol{\sigma_{fl} = \sigma_t}$	$\boldsymbol{\sigma_{fl} > \sigma_t}$
Inner fibre side	$\sigma_{fl} < \sigma_{t,f} + \sigma_t$	/	$\sigma_{fl} < \sigma_{c,f} + \sigma_t$
Outer fibre side	$\sigma_{fl} < \sigma_{t,f} - \sigma_t$	$\sigma_{fl} < \frac{\sigma_{t,f}}{2}$	$\sigma_{fl} < \sigma_{t,f} - \sigma_t$

2.6 DIAMETER OF THE MELT CHAMBER OUTLET

The diameter of the melt chamber outlet d_d (also called pultrusion die, stripper die or wipe-off die) and its relation to the fibre volume fraction can be modelled as Equation 2.36:

$$d_d = \sqrt{\frac{4\,\rho_{lin}}{\pi\,\rho_f V_f}} \tag{2.36}$$

d_d	Pultrusion die diameter	[m]
ρ_{lin}	Linear density of fibre bundle	[kg/m]
ρ_f	Density of fibre material	[kg/m³]
V_f	Fibre volume fraction	[/]

The choice of pultrusion die's diameter will determine V_f and is therefore a critical parameter in the design of the impregnation device. The actual V_f may slightly deviate from the targeted value due to shear thinning effects within a polymer matrix, as discussed in Paragraph 2.9. Note that a fibre volume fraction V_f larger than the previously calculated value of c_{hcp} (Equation 2.17) is mathematically possible but has no physical relevance.

2.7 FRICTION-BASED MODEL FOR PULTRUSION FORCE AND PRESSURE

2.7.1 Force equilibrium on a fibre bundle in contact with a spreader pin

A fibre bundle, being pulled over a spreader pin in an environment of liquified polymer could be described as a frictional contact between the fibres and a cylinder. To find the relation between fibre tension, friction of the fibre bundle sliding over the cylinder at a constant velocity and the generated pressure, all forces acting on a piece of fibre with infinitesimally small length δl are shown in Figure 2.10. Fibre bundle tensions F and $F + \delta F$ result in a normal force F_N, which causes a frictional force F_f between the fibre bundle and the cylinder. The dynamic friction coefficient between these two materials is represented by f and strongly depends on the presence of liquid polymer between the fibre bundle and the cylinder. Since the constant circumferential velocity v_1 of the fibre bundle in this application is low (order 0,01 m/s), centrifugal forces F_{cent} are considered negligible.

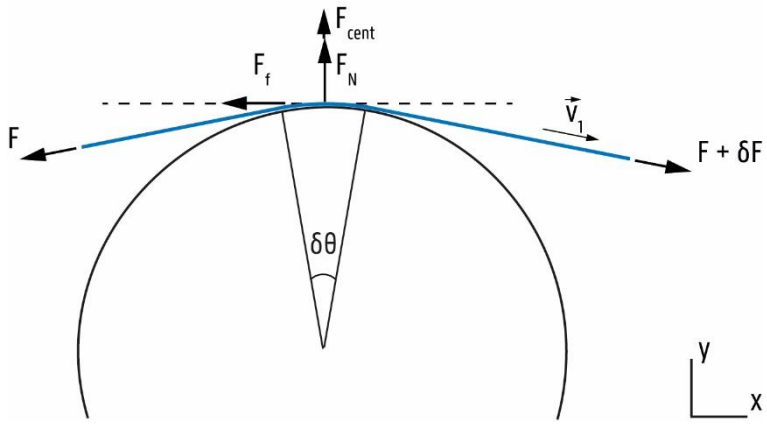

Figure 2.10: Forces acting on a fibre bundle sliding over a spreader pin.

x-axis and y-axis force equilibrium equations for this static case can be written as:

$$\begin{cases} \sum F_x = 0 \Leftrightarrow F_f = F_N f = (F + \delta F)\cos\dfrac{\delta\theta}{2} - F\cos\dfrac{\delta\theta}{2} \\ \sum F_y = 0 \Leftrightarrow F_N = F\sin\dfrac{\delta\theta}{2} + (F + \delta F)\sin\dfrac{\delta\theta}{2} \end{cases} \quad (2.37)$$

$$\begin{cases} F_N\, f = \delta F \cos\dfrac{\delta\theta}{2} \\ F_N = 2\sin\dfrac{\delta\theta}{2} F + \delta F \sin\dfrac{\delta\theta}{2} \end{cases} \tag{2.38}$$

With $\cos\frac{\delta\theta}{2} \approx 1, \sin\frac{\delta\theta}{2} \approx \frac{\delta\theta}{2}$ and $\delta F \sin\frac{\delta\theta}{2} \approx 0$ for small values of $\frac{\delta\theta}{2}$:

$$\begin{cases} F_N\, f = \delta F \\ F_N = \delta\theta\, F \end{cases} \Rightarrow \delta F = f\, \delta\theta\, F \tag{2.39}$$

$\delta\theta$	Central angle of the piece of fibre bundle	[rad]
f	Dynamic coefficient of friction between a fibre and the cylinder	[/]
F	Tensile force acting on a fibre bundle end	[N]
$F + \delta F$	Tensile force acting on a fibre bundle end	[N]
F_{cent}	Centrifugal force, acting on a fibre bundle	[N]
F_N	Normal force	[N]
R_p	Radius of the cylinder	[m]
v_1	Linear velocity of the fibre bundle	[m/s]

The differential equation (Equation 2.39) can be solved after separation of variables:

$$\frac{\delta F}{F} = f\, \delta\theta \tag{2.40}$$

Integration over a finite contact angle α, starting from F_1 to F_2 yields:

$$\int_{F_1}^{F_2} \frac{\delta F}{F} = \int_0^{\alpha} f\, \delta\theta \tag{2.41}$$

$$\ln\frac{F_2}{F_1} = f\, \alpha \tag{2.42}$$

$$F_2 = F_1 \, e^{f \, \alpha} \tag{2.43}$$

α	Contact angle of the fibre bundle around the cylinder	[rad]
f	Dynamic coefficient of friction between a fibre bundle and the cylinder	[/]
F_1	Tensile force acting on a fibre bundle end	[N]
F_2	Tensile force, acting on a fibre bundle end $F_2 > F_1$	[N]

The occurrence of drag forces (Figure 2.11) on the fibre bundles being pulled through a liquid polymer chamber can be implemented in Equation 2.43 to obtain a more realistic model:

$$F_2 = (F_1 + F_{d,1}) \, e^{f \, \alpha} + F_{d,2} \tag{2.44}$$

$F_{d,1}$	Drag force	[N]
$F_{d,2}$	Drag force	[N]

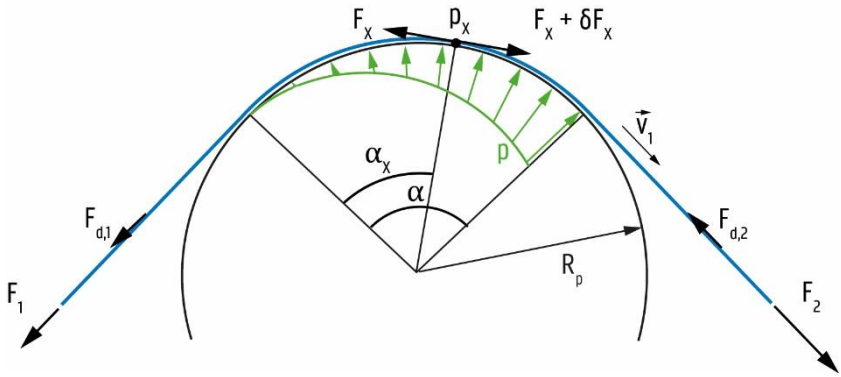

Figure 2.11: Fibre bundle (blue) wrapped around a spreader pin and pressure gradient within the thin polymer film between fibre and spreader pin.

2.7.2 Pressure build-up with spreader pins

By wrapping a tensioned fibre bundle (blue line on Figure 2.11) over a spreader pin for a certain contact angle α, a normal force is generated between both surfaces, which results in a pressure p_X at location X in between the fibre bundle and the

pin's surface. When the fibre bundle is pulled over the spreader pin, a continuous flow of polymer is drawn in between the fibre bundle and spreader pin. The pressure build-up will induce an outward radial flow of liquid polymer through the fibre bundle, as described by Darcy's law (Paragraph 2.3). The local pressure p_x in the polymer film can be calculated as the ratio of the normal forces acting on an infinitesimally small flow surface and the surface area (Figure 2.11). p_x can be calculated using Equation 2.45, in which p_0 is an externally applied pressure within the polymer film:

$$p_X = \lim_{\alpha \to 0} \frac{(2F_X + \delta F_X) \sin\left(\frac{\alpha}{2}\right)}{2\, R_p\, w\, \sin\left(\frac{\alpha}{2}\right)} + p_0 \tag{2.45}$$

For a constant pultrusion velocity v_1, the fibre bundle tension at location X, F_X can be seen as a special case of Equation 2.44 and is defined as follows:

$$F_X = (F_1 + F_{d,1})\, e^{f\, \alpha_X} \tag{2.46}$$

Since $\lim_{\alpha \to 0} \delta F_X = 0$, Equation 2.45 can be rewritten as:

$$p_X = \frac{\mathrm{F}_X}{\mathrm{R}_p\, w_f} + p_0 = \frac{(F_1 + F_{d,1})\, e^{f\, \alpha_x}}{R_p\, w_f} + p_0 \tag{2.47}$$

F_1	Tensile force acting on a fibre end	[N]
$F_{d,2}$	Drag force	[N]
p_0	Externally applied pressure	[MPa]
p_X	Local pressure in the polymer melt film	[MPa]
R_p	Radius of the spreader pin	[mm]
w_f	Width of the spread fibre bundle	[mm]

High pressures will promote the flow of polymer between the individual fibres. Yet, at too high pressures, fibres will be forced into their close packed configuration, which strongly reduces the permeability K of the bundle (cf. Paragraph 2.3). The fastest impregnation of the fibre bundle will occur when the exerted pressure reaches an optimum.

2.7.3 The use of multiple spreader pins

A common problem reported in fibre bundle impregnation literature is the formation of a 'dry' contact zone between fibre and spreader pin for large contact angles [23]. This phenomenon can be explained as follows: due to the polymer melt drag flow around the fibre bundle, a thin polymer film is formed between the fibre bundle and pin. The induced pressure will cause the melt film to migrate through the fibre bundle. For high pressures or long contact angles, this polymer film could get depleted before the end of the contact, so there will be no extra gain in impregnation quality when exceeding a certain contact angle. Therefore, it can be useful to create a cascade of different spreader pins that have lower individual contact angles. In this way, the fibre bundle can be recoated with polymer in between the different spreader pin contacts (Figure 2.12).

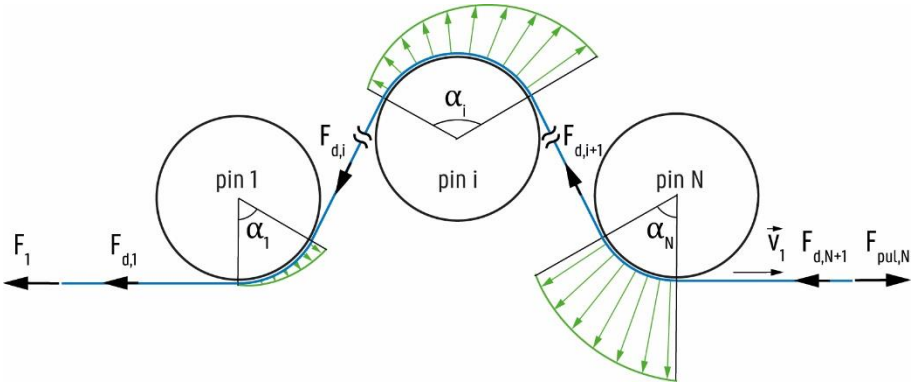

Figure 2.12: Pressure distribution within the polymer melt in a three spreader pin system (N = 3), according to the friction-based model.

The total contact angle in such a system can be calculated as the sum of all contact angles (Equation 2.48). An extra advantage of using multiple cylinders is that the bundle gets recoated with polymer in between the multiple contact zones and impregnation occurs at both sides of the spread fibre bundle (Figure 2.12). The equation for the total fibre bundle tension in this cascade of N spreader pins, assuming no drag forces, can be derived from a tension series caused by single pin:

$$F_{pul,N} = F_1 \prod_{i=1}^{N} e^{f_i \alpha_i} = F_1 \, e^{\sum_{i=1}^{N} f_i \alpha_i} \tag{2.48}$$

In practice, $F_{pul,N}$ will be larger due to drag forces, caused by the fibre bundle being pulled through a chamber filled with an - often - highly viscous liquid polymer (Figure 2.12). These forces are highly dependent on the geometry of the liquid polymer chamber and can be predicted in Computational Fluid Dynamics numerical simulations. For multiple impregnation pins, including drag forces, the total pultrusion force can be calculated by Equation 2.49:

$$F_{pul,N} = F_1 \, e^{\sum_{i=1}^{N} f_i \alpha_i} + \sum_{i=1}^{N+1} F_{d,i} \, e^{\sum_{j=i}^{N} f_j \alpha_j} \tag{2.49}$$

An alternative for one (or more) passive spreader pins is an active impregnation pin, through which liquid polymer is continuously being added in the contact region via small radial holes in the impregnation pin. This prevents the previously mentioned dry contact between the fibre bundle and pin. This design is an in-house developed, advanced version of a design described in US Patent 5,158,608 [24]. The developed device will be discussed in Paragraph 2.9.

2.8 FLOW-BASED CALCULATION OF SHEAR RATE AND SHEAR FORCE

In addition to inducing a pressure gradient over the polymer film and fibre bundle, the spreader pins also cause high shear in the polymer film due to the Couette flow manifesting itself in it [25]–[28]. High shear rates can potentially reduce the shear viscosity of the polymer, since it has shear-thinning characteristics (Paragraph 1.2.5). This effect will also facilitate impregnation [20], [28]. In order to estimate the shear rates being applied in the liquid polymer film between a fibre bundle and a spreader pin, the thickness of this film should be known. Analogous to the calculation of Nygard et al. [8], the average film thickness can be determined as the ratio of the final matrix volume fraction multiplied by the final cross-sectional area, to the fibre bundle width (Equation 2.50) while being pulled over a spreader pin (Figure 2.3). This calculation assumes a purely radial outward polymer flow through the fibre bundle. The occurring shear rates can be calculated using Equation 2.51. The corresponding average shear stress in the polymer film can be derived using Equation 1.2. Next to the radial polymer flow, Wang et al. modelled a flow parallel to

the spreader pin and performed numerical simulations in order to optimise the impregnation depth of this spreader pin-assisted melt impregnation process [29].

$$t_{av} = \frac{\pi \, V_m \, d_d^2}{4 \, w_f} \tag{2.50}$$

$$\frac{du}{dy} = \frac{v_1}{t_{av}} \tag{2.51}$$

d_d	Pultrusion die diameter	[m]
$\frac{du}{dy}$	Average shear rate	[1/s]
t_{av}	Average thickness of the liquid polymer film	[m]
v_1	Linear velocity of the fibre bundle	[m/s]
V_m	Matrix volume fraction	[/]
w_f	Width of the spread fibre bundle	[m]

Using Equation 2.51, it is possible to determine the shear rate interval in which the impregnation stage of a typical spreader pin-assisted EFAM process can operate (Figure 2.13). It can be noted that for higher deposition velocities, the polymer shows shear thinning behaviour. This phenomenon will aid the impregnation process.

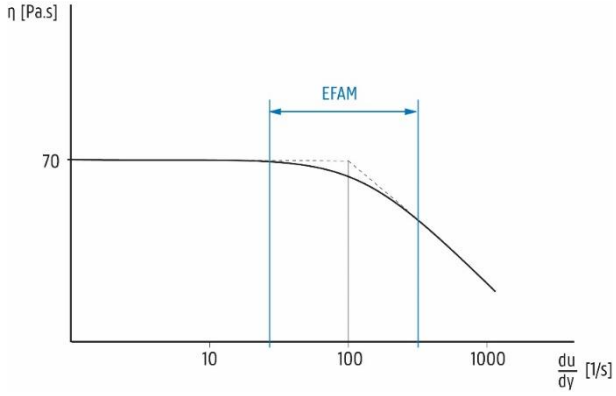

Figure 2.13: Shear rate interval of a typical spreader pin-assisted EFAM process, for a 40 vol% glass fibre - PA12 composite.

2.9 EVALUATION OF THREE TECHNIQUES FOR MELT IMPREGNATION OF GLASS FIBRE BUNDLES WITH PA12

Within this section, the impregnation quality of composite materials produced with three different melt impregnation techniques (**'Pultrusion', 'PassivePin' and 'ActivePin'**) will be compared. For this, matrix material mass fractions M_m of the three different composites will be determined as an estimation for degree of impregnation. Also, Scanning Electron Microscope (SEM) images of the impregnated fibre bundles' fractured cross-sections will be used and a fracture analysis will be performed to get insight into the relation of impregnation quality and observed failure mechanisms. Further, optical microscopy of polished composite cross-sections will not only give the opportunity to study the degree of impregnation, but will also provide information about dispersion and distribution of the fibres in the matrix. The results of different test methods will be compared and will be used to draw some important conclusions.

2.9.1 Materials and methods

2.9.1.1 Matrix and reinforcement material

Rilsamid AMN O TLD from Arkema, a polyamide 12 (PA12), was used as the matrix material for the composite. The Melt Flow Index (MFI) was determined according to ISO 1133-1:2005 with a Zwick 4100 apparatus as 51.61 ± 2.04 g/10 min (confidence level 95%), measured at 230°C, with the standardised weight of 2.16 kg mounted onto the piston. Its density was determined according to ISO 1183 to be 1092 ± 9 kg/m³ (confidence level 95%). Further in this manuscript, when a confidence interval is mentioned, it is given at a 95% confidence level, unless explicitly stated otherwise.

As fibre reinforcement material, a StarRov® LFTplus Direct Roving 853 endless glass fibre from Johns Manville was used. The linear density of the strand was determined according to ISO 1889:2009 and has a value of 1179.29 ± 5.48 g/km. The density of the fibre material is 2540 kg/m³. Mean single fibre diameter was determined on a polished, perpendicular cross-section of an embedded fibre bundle as 16.29 ± 1.75 µm. Using the values for the linear density and the mean single fibre diameter, the amount of single fibres per bundle can be calculated using Equation 2.52 and is for this specific glass fibre bundle about 2225 fibres per bundle. The fibre bundle is

delivered spooled on bobbins with half a twist of twine per metre to enhance its processability during (un)spooling.

$$N = \frac{4\,\rho_{lin}}{\pi\,d_f^2\,\rho_f} \tag{2.52}$$

d_f	Single fibre diameter	[m]
N	Fibre amount per bundle	[/]
ρ_{lin}	Linear density of fibre bundle	[kg/m]
ρ_f	Density of fibre material	[kg/m³]

2.9.1.2 Melt impregnation devices

Within this research, two melt impregnation devices suitable for processing PA12 and glass fibre, were developed. A **regular pultrusion device** for melt impregnation as shown in Figure 2.14, was developed for creating the **Pultrusion** material. The glass fibre bundle (dashed line on Figure 2.14) is pulled through a fibre bundle inlet (Figure 2.14, 1), through the liquid polymer chamber (Figure 2.14, 3) and through the exit die (Figure 2.14, 4). Liquid polymer material is added from a separate channel (Figure 2.14, 2).

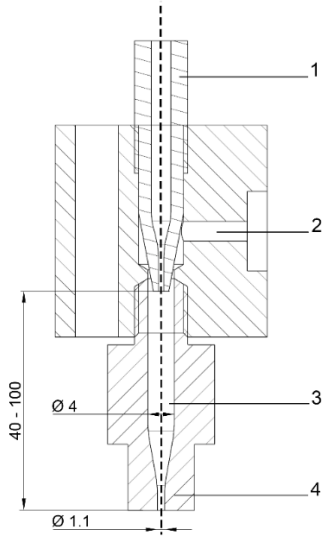

Figure 2.14: Regular pultrusion melt impregnation device, dimensions shown in mm. Fibre bundle inlet die (1), polymer supply channel (2), liquid polymer chamber (3) and exit die (4).

Secondly, a **spreader pin melt impregnation device** for creating of the **PassivePin** and **ActivePin** material was developed (Figure 2.15).

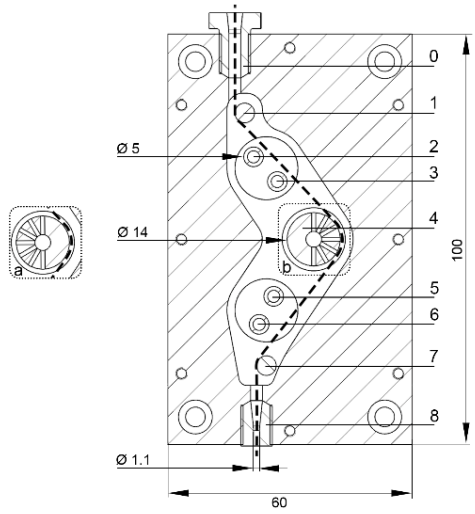

Figure 2.15: Interchangeable passive (situation a) or active (situation b) spreader pin impregnation device, dimensions shown in mm. Fibre bundle inlet die (0), passive spreader pins (1-3), active/passive spreader pin (4), passive spreader pins (5-7) and exit die (8).

The glass fibre bundle (Figure 2.15, dashed line) is pulled through the fibre bundle inlet (Figure 2.15, 0), which prevents the polymer melt from flowing out of the liquid polymer chamber, which is completely filled with the polymer. After being guided by pin 1 on Figure 2.15 to prevent the fibre bundle from contact with the mould wall, the fibre bundle can be guided between or over spreader pins 2 and 3, which are mounted on an rotatable drum to be able to adjust the bundle's contact angle. In Figure 2.15, the drum is rotated so that there is no contact with the fibre bundle. Downstream, there is an active impregnation pin (Figure 2.15, 4, situation b) which can be rotated 180° to position its 7 injection holes away from the fibre bundle to become a passive spreader pin (Figure 2.15, 4, situation a). The holes in pin 4 have a diameter of 1.5 mm and are located at every 30° in the shown cross-section. Through these holes, liquid polymer can be injected. Further downstream, the fibre bundle passes through spreader pins 5 and 6, which have the same functionality as pins 2 and 3. Finally, the bundle is guided over pin 7 (Figure 2.15) before exiting the spreader pin device through the pultrusion die (Figure 2.15, 8), which, in this case, has a diameter of 1.1 mm and wipes the excess PA12 off the pultruded strand. In this

stage of the research, a separate puller system was used downstream of both the regular pultrusion device and the spreader pin melt impregnation device during composite strand production. For the purpose of AM with endless fibre composites, this puller stage should be fully integrated within the EFAM process, as described in Chapter 3.

2.9.1.3 Composite production process

An in house developed extruder with a screw diameter of 10 mm and an L/D ratio of 10 was connected to both impregnation devices and is able to extrude liquid polymer into the melt chamber of both melt impregnation devices. The screw has a compression ratio of 1.8, i.e. the ratio of the cross-sectional area of the polymer flow in the feed zone to the one in the metering zone. The feed zone is the location where polymer pellets enter the extruder through a hopper or funnel (cf. Figure 2.1, 0). The metering zone is the location in the extruder where the polymer is completely liquified and mixed, right before it is extruded into the liquid polymer chamber. The rotational speed of the extruder screw was set at 10 rpm and the barrel has a temperature of 90°C in the feed zone, increasing to 220°C in the metering zone. The temperature of the impregnation devices' chamber wall was set at 220°C. Velocity of the glass fibre pultrusion was set at 600 mm/min.

Three tests were conducted, all starting from the pristine glass fibre bundle described in Paragraph 2.9.1.1:

i) Composite '**Pultrusion'** was produced in the regular pultrusion melt impregnation device as seen on Figure 2.14.

ii) '**PassivePin'** was produced in the spreader pin melt impregnation device as seen on Figure 2.15 with spreader pins 2-3 and 5-6 (Figure 2.15) disabled and with the polymer channels of the active impregnation pin faced away from the fibre bundle (situation a on Figure 2.15).

iii) composite '**ActivePin'** was produced on the spreader pin melt impregnation device with spreader pins 2-3 and 5-6 (Figure 2.15) disabled and with the polymer channels of the active impregnation pin faced to the glass fibre bundle (situation b on Figure 2.15), which allows the active pin to extrude polymer between the surface of the impregnation pin and the fibre bundle.

It should be noted that the path length of the fibre bundle in the regular pultrusion device is chosen identical to the path length of the fibre bundle in PassivePin and ActivePin configurations in the spreader pin device. All other parameters such as temperatures, pultrusion die diameter, fibre bundle tensions, pressures, etc. were kept constant. This also implies that possible excess polymer leakage through the pultrusion die would be equal in all production processes.

2.9.1.4 Quantifying impregnation quality by M_m determination

When the voids in between fibres are filled with matrix material during an impregnation process, the void mass fraction M_v will decrease proportionally. This will result in a larger matrix mass fraction M_m, providing there was no fibre fraction lost during the pultrusion process and there was no polymer leakage through the pultrusion die. Hence, M_m will provide a quantification of the impregnation quality of the produced composite.

Analogous to the calculation of M_f in Equations 2.5 to 2.8, M_m was determined in Equation 2.53. The maximal obtainable matrix mass fraction $M_{m,max}$ of the composite material can be calculated using Equations 2.2, 2.8 and 2.53, after setting $V_v = M_v = 0$ (Equation 2.54). For the setup described in Paragraph 2.9.1, a theoretical $M_{m,max}$ of 0,291 g/g was found, which is equivalent to a V_f of 49.3%. The degree of impregnation D_i can be calculated as the ratio of the actual M_m, determined in incineration experiments and $M_{m,max}$ (Equation 2.55), on the condition there is no polymer leakage between the pultrusion die wall and the wetted fibre bundle. Since there is a slight possibility of polymer leakage in this setup, no formal conclusions are drawn concerning the absolute degree of impregnation. In this research, the obtained data are used to relatively compare the three production methods. An absolute determination of degree of impregnation can be done by calculating the mean value of the void to (void + matrix) area ratio, measured in different cross-sections of a specimen. This methodology can be performed by optical microscopy or micro computed tomography [2].

$$M_m = \frac{m_m}{m_c} = \frac{v_m}{v_c}\frac{\rho_m}{\rho_c} = \frac{\rho_m V_m}{V_f \rho_f + V_m \rho_m + V_v \rho_v} \tag{2.53}$$

$$\begin{cases} V_f = \dfrac{4\,\rho_{lin}}{\pi\,\rho_f\,d_d^2} \\ V_m = 1 - V_f \\ M_{m,max} = \dfrac{V_m\,\rho_m}{V_f\,\rho_f + V_m\,\rho_m} \end{cases} \tag{2.54}$$

$$D_i = \frac{M_m}{M_{m,max}} \tag{2.55}$$

d_d	Pultrusion die diameter	[m]
D_i	Impregnation degree	[/]
m_c	Composite mass	[kg]
m_m	Matrix mass	[kg]
M_m	Matrix mass fraction	[/]
$M_{m,max}$	Maximal matrix mass fraction	[/]
ρ_c	Density of composite material	[kg/m³]
ρ_{lin}	Linear density of fibre bundle	[kg/m]
ρ_m	Density of matrix material	[kg/m³]
ρ_f	Density of fibre material	[kg/m³]
ρ_v	Density of voids	[kg/m³]
v_c	Composite volume	[m³]
v_m	Matrix volume	[m³]
V_f	Filler volume fraction	[/]
V_m	Matrix volume fraction	[/]
V_v	Void volume fraction	[/]

Before material sampling, the first and last 500 mm of the pultruded strands were discarded. In order to get a statistically significant result for the M_m values, for each material sample, 20 composite specimens with a length of 100 ± 1 mm were collected with a distance of 50 ± 1 mm between subsequent specimens on the pultruded strand. Those shorter parts were used during the optical microscopy and SEM analyses. The distance between specimens was kept low on purpose to reduce the possible effect of fibre mass loss due to fibre failure in the pultrusion die. This phenomenon could be falsely interpreted as an increase in M_m, thus would wrongly overestimate impregnation quality. To test the occurrence of fibre failure in the melt chamber during production of the three samples, the content of the liquid polymer

chamber was incinerated after production. In the rare case that fibres were found in the residual fraction, all specimens of that specific production run were discarded and produced anew.

The specimens of the produced composites were dried at 80°C for 8h and were weighed using a Precisa XR 205SM-DR apparatus (Dietikon, Switserland). Then, the specimens were incinerated for 15 minutes at a temperature of 550°C in a Nabertherm P300 oven (Lilienthaal, Germany). Subsequently, the residual mass of the specimens was weighed using previously mentioned Precisa apparatus and corresponds to the fibre mass m_f. The mass loss during incineration corresponds with m_m. M_m was calculated by Equation 2.4, with m_c the initial mass of the composite specimen before incineration. Due to the relatively low density of entrapped gasses in the samples compared to the matrix and fibre density, the mass fraction of the voids M_v was neglected.

To check whether there is a statistically significant influence of the three production techniques on the impregnation quality and thus on M_m, a one way variance analysis was conducted to compare the M_m of composites Pultrusion (produced using a regular pultrusion process), PassivePin (produced with passive spreader pin) and ActivePin (produced with active impregnation pin) at a 95% confidence level.

2.9.1.5 Evaluating of impregnation quality by fracture analysis

A visual evaluation of the fibre bundles' impregnation quality was done using SEM of fractured composite specimens. To this end, three specimens per production technique were fully submersed in liquid nitrogen for 60 s and broken perpendicular to the fibre direction immediately afterwards. It was impossible to obtain fully brittle fracture surfaces due to the ductile behaviour of the PA12 matrix material, even at extremely low temperatures (boiling point of liquid nitrogen is -196°C).

Before imaging, the specimens were gold sputtered during 60 s with a current of 25 mA. An accelerating voltage of 15 kV and working distances (WD) between 11 and 13 mm were used on a Jeol JSM-7600F apparatus (Tokyo, Japan) in secondary electron imaging (SEI) mode for visualizing the fracture surface.

2.9.1.6 Inspecting impregnation quality using optical microscopy

For each of the different production methods, three composite specimens were embedded in a cold curing epoxy Epofix from Struers (Ballerup, Denmark). The

specimens were ground and polished to reveal the cross-section of the impregnated bundle, perpendicular to the fibre direction. The cross-sections of three different composites were visualised using a Keyence VHX-500F Digital optical microscope (Osaka, Japan). Optical microscopy at magnifications of 200 allowed for visualising features such as fibre distribution and dispersion, location of the voids, etc.

2.9.1.7 Quantifying fibre dispersion and distribution in a composite strand

Consider a circular cross-section of a unidirectional fibre composite, perpendicular to the fibre direction (Figure 2.16). The cross-section contains N_f unique fibres, each of these can be represented by its polar coordinates (radius r_i and polar angle φ_i for fibre i) measured at the fibre's centre. The inter-fibre distance $d_{i,j}$ between fibre i and j is defined in Equation 2.56:

$$d_{i,j} = \sqrt{r_i^2 + r_j^2 - 2\, r_i\, r_j \cos(\varphi_i - \varphi_j)} \tag{2.56}$$

$d_{i,j}$	Inter-fibre distance between fibre i and j	[m]
φ_i	Polar angle of fibre i	[rad]
φ_j	Polar angle of fibre j	[rad]
r_i	Polar radius of fibre i	[m]
r_j	Polar radius of fibre j	[m]

All possible pairwise inter-fibre distances are listed in a two-dimensional matrix (Table 2.2). All N_f distances between a fibre and itself are situated on the main diagonal of the matrix and have a zero magnitude. All $\frac{N_f\,(N_f-1)}{2}$ distances $d_{i,j}$ below the main diagonal show symmetry with their mirror elements $d_{j,i}$ above the diagonal, so that the transpose of this matrix is identical to the original matrix. Only the values below the main diagonal are listed and used in further statistical analyses. The fibre distribution and dispersion can be characterised by plotting this dataset in a histogram.

Table 2.2: Matrix with all inter-fibre distances in a composite with N_f fibres.

	1	**2**	**…**	***j***	**…**	N_f
1	$d_{1,1}$	$d_{1,2}$	…	$d_{1,j}$	…	$d_{1,N}$
2	$d_{2,1}$	$d_{2,2}$	…	$d_{2,j}$	…	$d_{2,N}$
…	…	…	…	…	…	…
i	$d_{i,1}$	$d_{i,2}$	…	$d_{i,j}$	…	$d_{i,N}$
…	…	…	…	…	…	…
N_f	$d_{N,1}$	$d_{N,2}$	…	$d_{N,j}$	…	$d_{N,N}$

For an idealised hexagonal close packed fibre distribution (Figure 2.17) or for a random fibre distribution in the circular cross-section, a Bell-shaped histogram is expected. All fibre distribution imperfections in an actual composite cross-section will have a consequence on the shape of the histogram, which can be quantified by parameters such as mean inter-fibre distance, the standard deviation, skewness and (excess) kurtosis values of the distribution. The higher the value of the standard deviation, the better the distribution of the fibres in the cross-section will be, a high value for inter-fibre distance is pursued. Skewness is caused by asymmetry in the distribution, meaning there are proportionally more extremely low or high inter-fibre distances, giving important clues about fibre dispersion. A positive skew relates to a longer, right 'tail', shifting the mass of the distribution left. This relates more extremely small inter-fibre distances, or coagulated fibres. A negative skew shifts the mass of the distribution to the right side and is related to fibre free zones. The kurtosis gives information about the 'tails' of the distribution. In a normal distribution with high kurtosis, there is a low chance for extreme values, resulting in small 'tails', a low kurtosis on the other hand indicates a distribution with pronounced 'tails'.

The actual fibre distribution and dispersion is likely to resemble one (or more) of the idealised scenarios, as shown in Figures 2.17 to 2.21. The actual inter-fibre distance histogram is highly dependent of the processing method and conditions and can be compared to each of these scenarios.

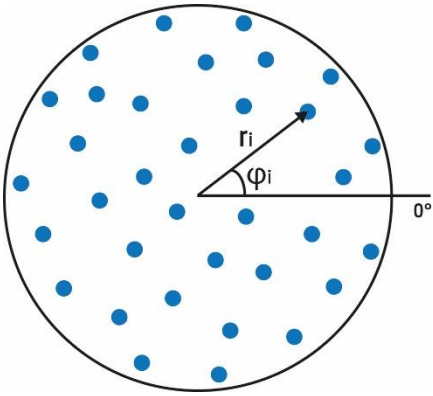

Figure 2.16: Perpendicular cross-section of a UD composite, polar coordinate system.

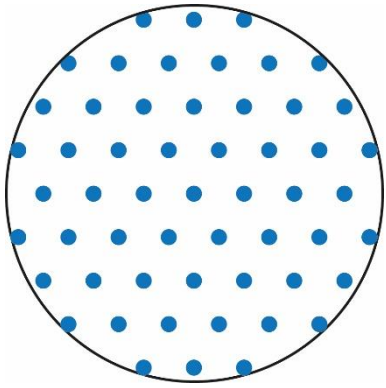

Figure 2.17: Perpendicular cross-section of a UD composite, hexagonal close packed fibres.

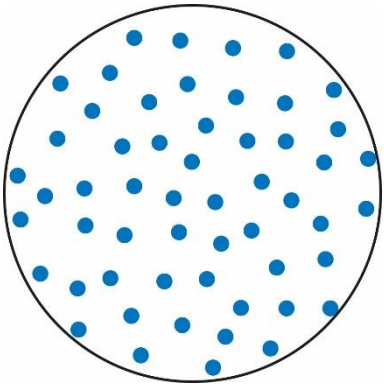

Figure 2.18: Perpendicular cross-section of a UD composite, random packed fibres.

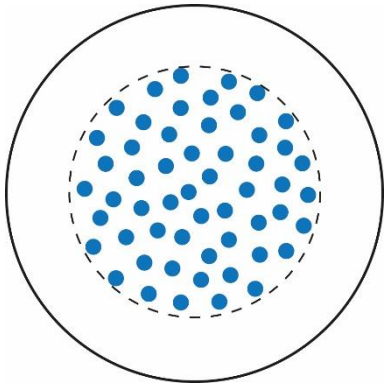

Figure 2.19: Perpendicular cross-section of a UD composite, fibre-rich core.

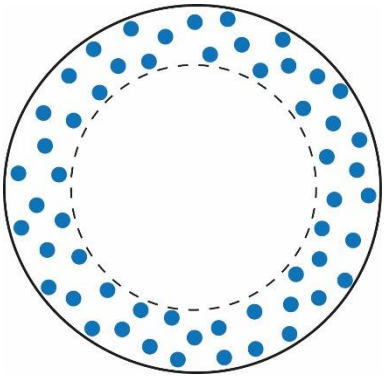

Figure 2.20: Perpendicular cross-section of a UD composite, fibre-rich mantle.

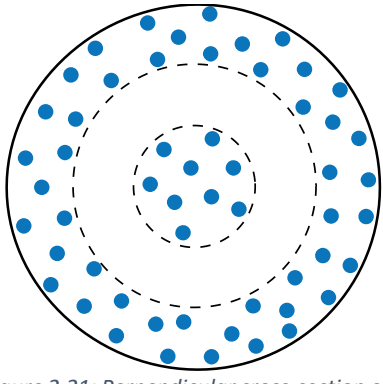

Figure 2.21: Perpendicular cross-section of a UD composite, fibre-rich core and mantle.

2.9.2 Results and discussion

2.9.2.1 Matrix mass fraction determination results

Table 2.3 shows the mean values and 95% confidence intervals of the M_m for the three produced composites and mean D_i. A statistically significant difference in M_m was measured for Pultrusion, PassivePin and ActivePin as determined by one-way variance analysis ($F(2,57) = 163.46$, $p = 0.000$). It is concluded that the use of a passive or an active impregnation pin drastically improves the M_m compared to the pultrusion production technique. The use of an active impregnation pin rather than a passive spreader pin further improves M_m and related impregnation quality.

Table 2.3: Statistical analysis of M_m and D_i for three different melt impregnation techniques.

Composite material	N	Mean M_m	Conf. Int.	Mean D_i	Conf. Int.
	#	g/g	g/g	%	%
Pultrusion	20	0.217	± 0.026	74.5	± 8.8
PassivePin	20	0.269	± 0.024	92.2	± 8.3
ActivePin	20	0.285	± 0.024	98.0	± 8.3

A bar chart with the mean M_m of three composites can be found in Figure 2.22. The theoretical maximal mass fraction $M_{m,max}$ for the described machine configuration (Paragraph 2.9.1.2) was calculated by Equation 2.54, has a value of 0.291 g/g and is displayed as a horizontal line in Figure 2.22. The three mean M_m values are below this maximal value, some ActivePin M_m measurements exceeded the theoretical maximal value. Two possible explanations for this phenomenon can be found: the 1 mg error of the used Precisa balance translates in an error of ± 2% in impregnation degree. Another possibility is that there was a limited amount of polymer leaking between die walls and impregnated fibre bundle, leading to a slight overestimation of M_m and D_i. It is concluded that mass fraction measurements are a good way of showing relative differences in impregnation quality, however, they should be combined with optical tests to draw conclusions on the absolute impregnation degree and fibre distribution and dispersion in the matrix.

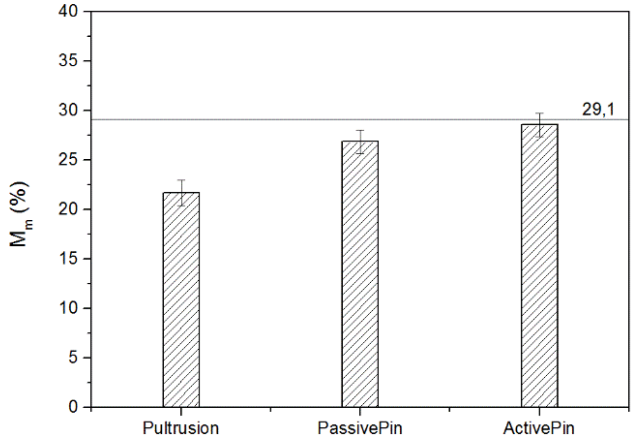

Figure 2.22: Mean matrix material mass fractions for three production techniques (1 standard deviation error bars).

2.9.2.2 Scanning electron microscopy results

Fracture surfaces of the composite material samples Pultrusion (Figure 2.23), PassivePin (Figure 2.24) and ActivePin (Figure 2.25) were visualized with SEM. Comparison of the samples learns that fracture surface topographies show important differences. The morphology within groups was very similar, so only one micrograph per sample will be discussed in this section.

A micrograph of the Pultrusion sample can be seen on Figure 2.23. Peaks of loose fibres and locations of fibre-pull out can be observed. This phenomenon is caused by axially oriented voids in between fibres that form stress concentrators in the matrix and mainly reduce shear moduli $G_{1,2}$ and $G_{1,3}$ [30]. These axially oriented voids situated between adjacent fibres initiate plastic shear while fracturing a specimen during specimen preparation. Tensile or compression forces on fibres close to voids will create high fibre stresses, since the matrix's ability for stress distribution is limited there. When individual fibre tensile strength is reached, the fibre will break, stresses will be redistributed in the specimen, which will eventually lead to a cascade effect of failing fibres. The fractured fibres will be pulled out of the matrix and cause the described topography. Further, locations without impregnation can be remarked. This result is in line with the conclusions made in the M_m analysis.

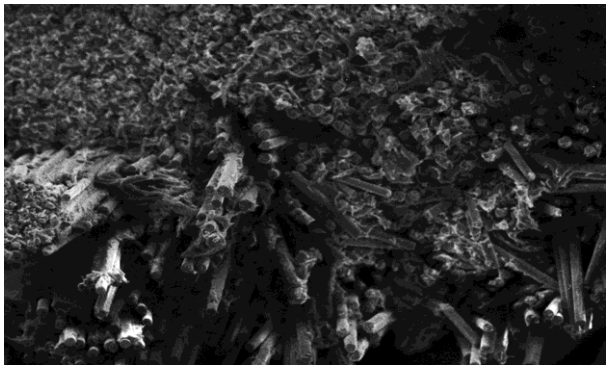

Figure 2.23: SEM image of a fractured Pultrusion specimen.

It can be seen that the PassivePin specimen has a fracture surface with peaks of loose fibres (Figure 2.24, 1, 2 and 3) and indentations where fibres were pulled out during specimen fracturing (Figure 2.24, 4 and 5). This effect is caused by the same phenomenon which occurred also at the Pultrusion specimen. Also, several dark spots can be noticed, spread on the fracture surface, which confirms the voids between adjacent fibres. It is concluded that the passive impregnation pins fail to fully impregnate the fibre bundle.

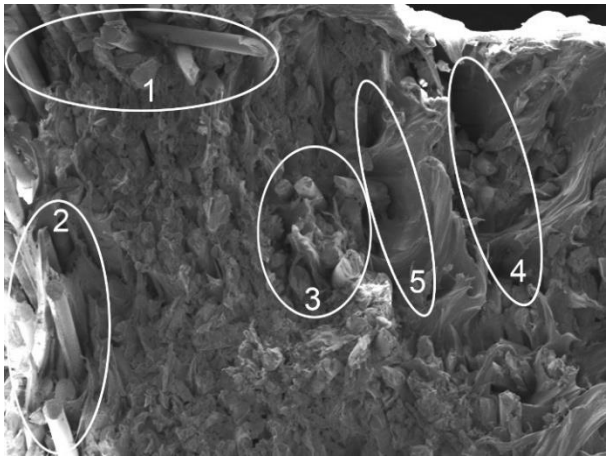

Figure 2.24: SEM image of a fractured PassivePin specimen.

The fracture surface of the ActivePin sample (Figure 2.25) shows a more even topography since there were less to no axial voids that can propagate shear cracking in planes parallel to the main fibre direction. This reduces fibre pull-out during the

fracturing of the specimen and results in a smoother fracture surface, since fibres remain firmly embedded in the matrix material after fracture.

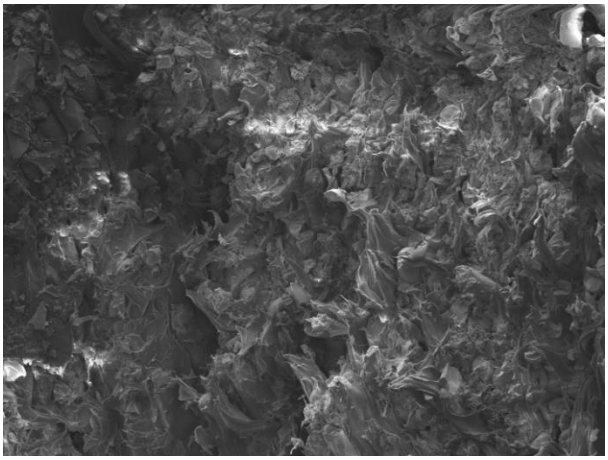

Figure 2.25: SEM image of a fractured ActivePin specimen.

Note that for the three material's surfaces, plastically deformed regions of the PA12 matrix can be seen, which implies that the used specimen preparation method fails to cause a fully brittle fracture.

2.9.2.3 Optical microscopy results

Optical microscopy showed that the obtained morphology within groups seemed to be very similar, so only one micrograph per sample will be discussed in this section. However, important differences per production method were observed and will be described.

A micrograph of composite material produced using the regular pultrusion method can be seen in Figure 2.26. After the Pultrusion process, the original tape like fibre bundle was still recognisable as it was supplied but was wrapped around a core of polymer (Figure 2.26, 1). The poor fibre dispersion is attributed to the lack of manipulation and spreading during pultrusion of the slightly coagulated fibres. This coagulation is a consequence of the coating or 'sizing' which is applied to fibre bundles during their manufacturing process. Within the fibre bundle itself, poor to moderate impregnation was observed. In Figure 2.26, 2, epoxy material from the embedding process was observed in the fibre bundle, which means it was a void area before embedding. It is concluded that despite the moderate M_m of the composite,

the inferior fibre distribution and dispersion renders the composite unsuitable for applications which require high mechanical properties.

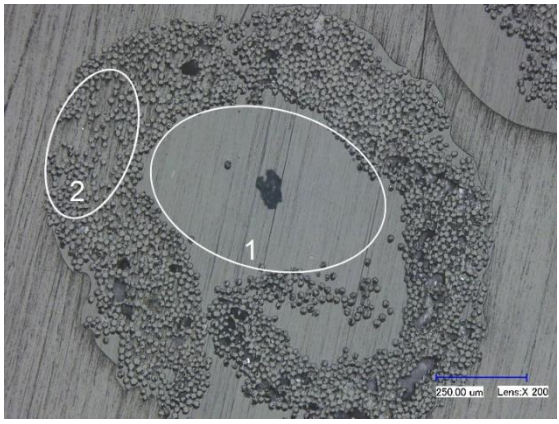

Figure 2.26: Optical microscopy image of a Pultrusion specimen.

When comparing composites produced using Pultrusion (Figure 2.26) and PassivePin (Figure 2.27), a clear difference in fibre dispersion and degree of impregnation can be seen. A passive spreader pin is able to disintegrate the coagulated fibre bundles, enhance the fibre's permeability and impregnate the voids between them. Nonetheless, some zones within the fibres were not impregnated with PA12 during production, some clear voids can be seen in the micrograph. It is concluded that by using a passive impregnation pin, a better quality of impregnation can be achieved, compared to a standard Pultrusion process.

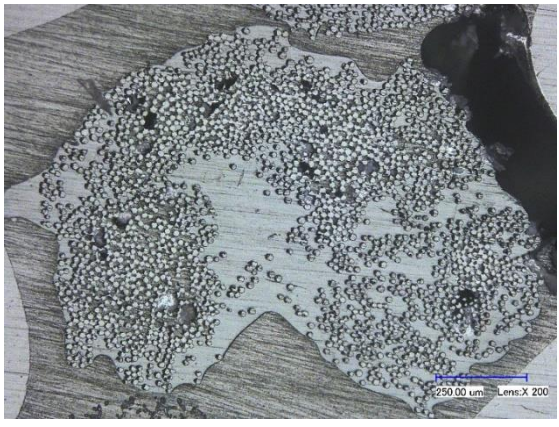

Figure 2.27: Optical microscopy image of a PassivePin specimen.

Studying the ActivePin micrograph (Figure 2.28) it can be seen that both fibre dispersion and distribution is reasonably good. Except for some smaller zones where voids occurred, degree of impregnation is sufficient. It is concluded that the ActivePin outperforms the Pultrusion and PassivePin process when it comes to impregnation quality. This result is promising and indicates that high impregnation quality of PA12 in glass fibre bundles can be achieved when using an optimised device.

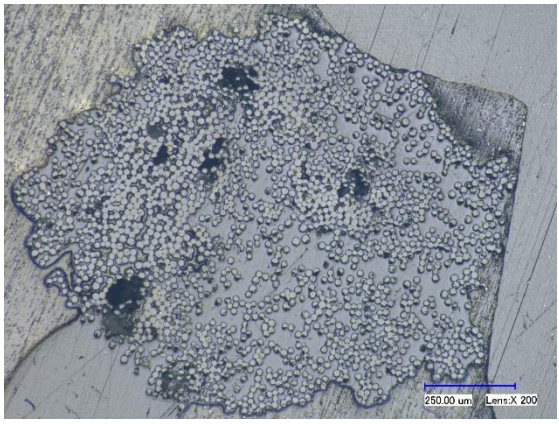

Figure 2.28: Optical microscopy image of an ActivePin specimen.

2.9.2.4 Quantifying fibre dispersion and distribution in a composite strand

In Figure 2.29, the inter-fibre distance histograms are shown for the three production methods. The histogram of the 'Pultrusion' specimen shows a clear bimodal behaviour. On the one hand, there are more very small values of inter-fibre distance than expected in an idealised situation, indicating coagulation of the fibres. On the other hand, a pronounced peak of large inter-fibre distances indicates the existence of large fibre free zones. The fibres are clearly neither distributed, nor dispersed well.

For the 'PassivePin' specimen, the histogram looks closer to a Bell shape, but is clearly positively skewed, meaning that the mass of the distribution is concentrated left and the histogram has a right tail. This shows that there is a light tendency of the fibres to coagulate, i.e. have a poor dispersion in the matrix.
The inter-fibre distance histogram of the 'ActivePin' specimen is in good accordance with the expected, ideal shape. However, a slight positive skew can be noticed,

indicating that not all fibres were dispersed well during the impregnation of the fibre bundle.

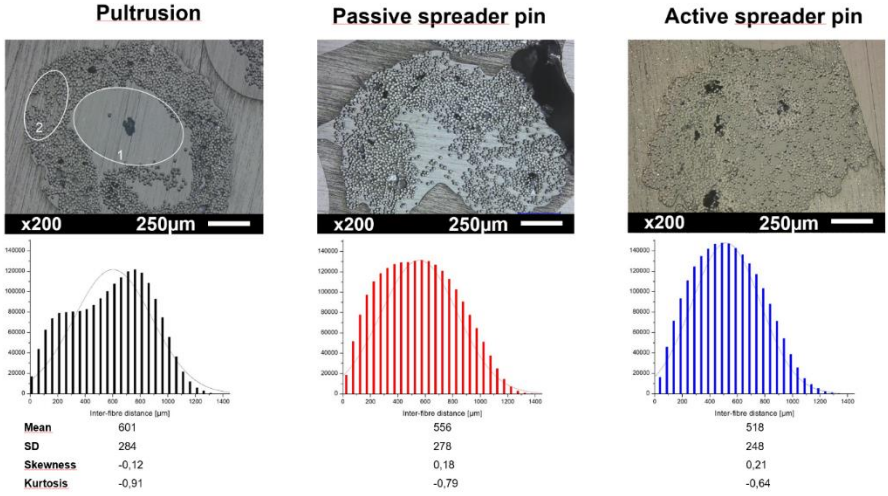

Figure 2.29: Summary of the stochastic fibre distribution and dispersion results.

2.9.3 Conclusions

This paragraph assessed three techniques for melt impregnation of continuous glass fibre bundles with PA12, with the aim of creating a high strength and modulus material for extrusion-based additive manufacturing. Therefore, three materials were produced:

i) a first material was produced using a standard pultrusion process 'Pultrusion';
ii) a second material was processed using a passive impregnation pin technique 'PassivePin',
iii) a third material was produced using the in-house developed active impregnation pin technique 'ActivePin', which injects liquid polymer between a fibre bundle and a cylindrical friction surface to enhance impregnation quality.

The impregnation quality of these samples was analysed using three methods: M_m determination, SEM of composite fracture surfaces and optical microscopy of polished composite cross-sections.

Process 'Pultrusion' resulted in a M_m of 0.217 ± 0.0255 g/g, 'PassivePin' in 0.269 ± 0.0241 g/g and the 'ActivePin' process in 0.285 ± 0.0241 g/g, where the theoretical maximal value for M_m was 0.291 g/g. It was concluded that both PassivePin and ActivePin perform significantly better than Pultrusion. Also, The ActivePin process significantly outperformed PassivePin. These results can be used as a relative comparison between the three production methods but should be combined with optical results of composite cross-sections to draw final conclusions about impregnation degree and fibre distribution and dispersion.

SEM analysis of fractured composites specimens showed that voids were predominant in Pultrusion samples and fibre pull-out was initiated by the axially oriented voids. PassivePin only showed small voids and a limited amount of fibre pull-out at the void locations. In the fracture surface of ActivePin, fibres remained firmly embedded in the matrix, there was a good stress distribution during fracturing, which lead to a smooth fracture topography.

During optical microscopy of the Pultrusion specimens, it was seen that the fibre bundle was wrapped around a polymer core and impregnation of the bundle was poor. In PassivePin specimens, the original shape of the fibre bundle was still recognizable but there was a better fibre distribution and dispersion compared to Pultrusion material. An excellent fibre dispersion of the fibres in the matrix and only a very limited of matrix voids was obtained with the ActivePin technique.

When the findings of the analyses are compared, it is clear that the results of each analysis are parallel for a certain material. Pultrusion material has an overall poor impregnation degree and fibre distribution and dispersion, the specimens lack mechanical strength and show fibre pull-out due to the excessive voids in the matrix. PassivePin material has a higher impregnation degree and a better fibre distribution, which results in less voids in the matrix and limited fibre pull-out. Finally, the ActivePin material scores significantly higher in impregnation degree and shows an excellent fibre distribution. As a consequence, very limited voids are observed and an even fracture surface without fibre pull-out is obtained.

It is clear that the ActivePin technique is suited for application in an extrusion-based AM process, since this method could allow for production of high strength and

stiffness objects. The ActivePin technique will be used throughout the further course of this research.

2.10 FINAL CONSIDERATIONS ON MELT IMPREGNATION

This chapter commenced with a theoretical approach to model melt impregnation, based on Darcy's law. Important elements of an impregnation process, such as minimal diameter of the fibre bundle inlet, minimal bending radius of a fibre and diameter of the melt chamber outlet were modelled. A friction-based model for pultrusion forces, pressures and shear rates in a spreader pin impregnation device was proposed. It was concluded that the use of spreader pins succeeds in successfully addressing most terms in Darcy's law for increasing the impregnation velocity. Firstly, a spreader pin reduces the impregnation distance due to the spreading of the fibre bundle. Also, the induced high local pressure in the liquid polymer film between fibre bundle and spreader pin is a driving force for impregnation. Within this thin polymer film, high shear rates occur during the pultrusion process. These reduce the polymer's shear viscosity due to its shear-thinning properties and can increase the impregnation rate. The shear viscosity can be further reduced by internal heating of the spreader pins, as a consequence of the inverse viscosity-temperature dependence, as described by an Arrhenius equation.

Based on previously mentioned theoretical considerations, three different techniques for melt impregnation were proposed: 'Pultrusion', 'PassivePin' and 'ActivePin'. The techniques using spreader pins (PassivePin and ActivePin) significantly outperformed the Pultrusion technique regarding the impregnation degree. The ActivePin technique, continuously injecting liquid polymer to maintain a melt film between the fibre bundle and the spreader pin resulted in the highest impregnation degree and will be used throughout the further course of this research, albeit in a completely automated form. In Figure 2.29 and 2.30, this fully automated EFAM composite deposition head is presented. A fibre bundle enters the thermally insulated liquid polymer chamber (Figure 2.30, blue) and polymer is supplied to it by a micro extruder (Figure 2.29, yellow). The conception of this extruder was at the basis for the development of a conical extruder with axial displacement. This work

resulted in a patent: 'An extruder with axial displacement' [31]. The puller system (Figure 2.29 and 2.30, white) is mounted onto the polymer chamber and the heated deposition nozzle (Figure 2.29 and 2.30, green) is mounted to it. Due to confidentiality reasons, an elaborate technical description of the design is beyond the scope of this work.

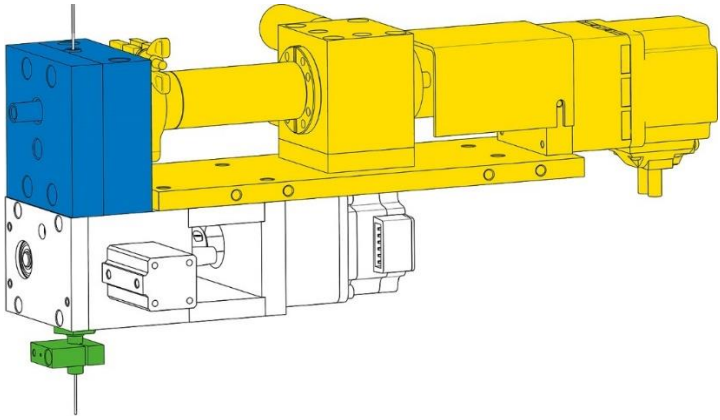

Figure 2.30: Automated EFAM impregnation device: insulated liquid polymer chamber (blue), single-screw extruder (yellow), puller system (white) and heated deposition nozzle (green).

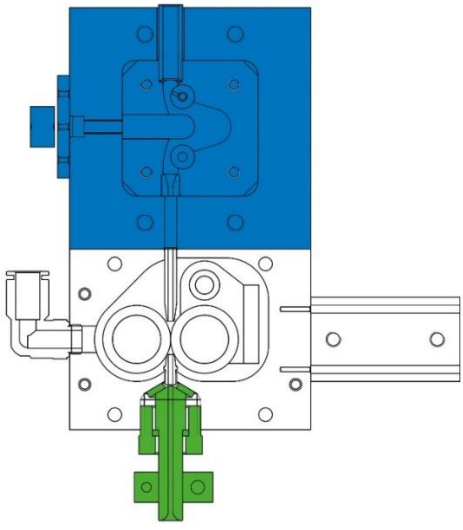

Figure 2.31: Cross-section of an EFAM impregnation device: insulated liquid polymer chamber (blue), puller system (white) and heated deposition nozzle (green).

2.11 REFERENCES

[1] W. Van De Steene, J. Verstockt, J. Degrieck, K. Ragaert, and L. Cardon, "An Evaluation of Three Different Techniques for Melt Impregnation of Glass Fiber Bundles With Polyamide 12," *Polym. Eng. Sci.*, 2018.

[2] A. Du Plessis, I. Yadroitsev, I. Yadroitsava, and S. G. Le Roux, "X-Ray Microcomputed Tomography in Additive Manufacturing: A Review of the Current Technology and Applications," *3D Print. Addit. Manuf.*, vol. 5, no. 3, pp. 227–247, 2018.

[3] S. Petersmann *et al.*, "Mechanical properties of polymeric implant materials produced by extrusion-based additive manufacturing.," *J. Mech. Behav. Biomed. Mater.*, vol. 104, no. December 2019, p. 103611, 2019.

[4] T. A. K. Sadiq, S. G. Advani, and R. S. Parnas, "Experimental investigation of transverse flow through aligned cylinders," *Int. J. Multiph. Flow*, vol. 21, no. 5, pp. 755–774, 1995.

[5] B. R. Gebart, "Permeability of Unidirectional Reinforcements for RTM," *J. Compos. Mater.*, 1991.

[6] A. M. Choi, H. M. Lee, J. Chang, and J. S. Lee, "Permeability modeling of fibrous media in composite processing," vol. 79, pp. 585–598, 1998.

[7] T. G. Gutowski, T. Morigaki, and Z. Cai, "The Consolidation of Laminate Composites," *J. Compos. Mater.*, vol. 21, no. 2, pp. 172–188, 1987.

[8] P. Nygård and C. G. Gustafson, "Continuous Glass Fiber-Polypropylene Composites Made by Melt Impregnation: Influence of Processing Method," *J. Thermoplast. Compos. Mater.*, vol. 17, no. 2, pp. 167–184, 2004.

[9] M. V. Bruschke and S. G. Advani, "Flow of generalized Newtonian fluids across a periodic array of cylinders," *J. Rheol. (N. Y. N. Y).*, vol. 37, no. 3, pp. 479–498, 1993.

[10] T. Ozgumus, M. Mobedi, and U. Ozkol, "Determination of Kozeny constant based on porosity and pore to pore throat size ratio in porous medium with rectangular rods," vol. 8, no. 2, pp. 308–318, 2014.

[11] C. Chmielewski, C. A. Petty, and K. Jayaraman, "Crossflow of elastic liquids through arrays of cylinders," *J. Nonnewton. Fluid Mech.*, vol. 35, no. 2–3, pp. 309–325, 1990.

[12] J. Yang, Y. Jia, S. Sun, D. Ma, T. Shi, and L. An, "Mesoscopic simulation of the impregnating process of unidirectional fibrous preform in resin transfer molding," vol. 436, pp. 515–520, 2006.

[13] R. Gennaro, A. Greco, and A. Maffezzoli, "Numerical Simulation of the Microscale Impregnation in Commingled Thermoplastic Composite Yarns," vol. 29, no. 2, pp. 122–130, 2010.

[14] G. Bechtold and L. Ye, "Influence of fibre distribution on the transverse flow permeability in fibre bundles," vol. 63, no. 2003, pp. 2069–2079, 2006.

[15] J. G. Williams, C. E. M. Morris, and B. C. Ennis, "Liquid flow through aligned fiber beds," *Polym. Eng. Sci.*, vol. 14, no. 6, pp. 413–419, 1974.

[16] V. Michaud and A. Mortensen, "Infiltration processing of fibre reinforced composites : governing phenomena," vol. 32, 2001.

[17] H. Pascal, "Rheological behaviour effect of non-newtonian fluids on steady and unsteady flow through a porous medium," *Int. J. Numer. Anal. Methods Geomech.*, vol. 7, no. 3, pp. 289–303, 1983.

[18] R. P. Chhabra, J. Comiti, and I. Machač, "Flow of non-Newtonian fluids in fixed and fluidised beds," *Chem. Eng. Sci.*, vol. 56, no. 1, pp. 1–27, 2001.

[19] K. Velten, A. Lutz, and K. Friedrich, "Quantitative characterization of porous materials in polymer processing," vol. 59, pp. 495–504, 1999.

[20] C. Mayer, X. Wang, and M. Neitzel, "Macro- and micro-impregnation phenomena in continuous manufacturing of fabric reinforced thermoplastic composites," *Compos. Part A Appl. Sci. Manuf.*, vol. 29, no. 7, pp. 783–793, 1998.

[21] S. Koubaa, C. Burtin, and S. Le Corre, "Investigation of capillary impregnation for permeability prediction of fibrous reinforcements," 2015.

[22] K. Ishii *et al.*, "Bending fracture rule for 3D-printed curved continuous-fiber composite," *Adv. Compos. Mater.*, vol. 28, no. 4, pp. 383–395, 2019.

[23] R. J. Gaymans and E. Wevers, “Impregnation of a glass fibre roving with a polypropylene melt in a pin assisted process,” *Compos. Part A Appl. Sci. Manuf.*, vol. 29, no. 5–6, pp. 663–670, 1998.

[24] M. Unger, “Method and apparatus for manufacturing fibre-reinforcing material,” 5,158,806, 1992.

[25] P. J. Bates, J. Kendall, D. Taylor, and M. Cunningham, “Pressure build-up during melt impregnation,” *Compos. Sci. Technol.*, vol. 62, no. 3, pp. 379–384, 2002.

[26] P. J. Bates, “Effects of Process Parameters on Melt Impregnation of Glass Roving,” *J. Thermoplast. Compos. Mater.*, vol. 12, pp. 276–296, 1999.

[27] R. Marissen, L. T. Van Der Drift, and J. Sterk, “Technology for rapid impregnation of fibre bundles with a molten thermoplastic polymer,” *Compos. Sci. Technol.*, vol. 60, no. 10, pp. 2029–2034, 2000.

[28] H. Bijsterbosch and R. J. Gaymans, “Impregnation of glass rovings with a polyamide melt. Part 2: Wipe-off die,” *Compos. Manuf.*, vol. 4, no. 3, pp. 133–137, 1993.

[29] R. G. Wang, F. Yang, L. F. Hao, G. Du, and W. C. Jiao, “Optimizing processing parameters of pin-assisted-melt impregnation of fiber-reinforced plastics by numerical simulation,” *J. Reinf. Plast. Compos.*, vol. 31, no. 11, pp. 731–737, 2012.

[30] H. Huang and R. Talreja, “Effects of void geometry on elastic properties of unidirectional fiber reinforced composites,” *Compos. Sci. Technol.*, vol. 65, no. 13, pp. 1964–1981, 2005.

[31] L. Cardon, D. D’Hooge, K. Ragaert, W. Van De Steene, M. Erkoç, and M. Moerman, “An extruder with axial displacement,” WO2019141606A1, 2019.

3 ENDLESS FIBRE ADDITIVE MANUFACTURING: PROCESS WORKFLOW AND COMPOSITE MORPHOLOGY

3.1 INTRODUCTION

In Chapter 1, the workflow of the complete EFAM process was explained as a three-stage process within the EFAM deposition head. Chapter 2 focused on the first stage of the EFAM process, i.e. the impregnation procedure. A fully automated impregnation device, as described in Paragraph 2.10, can be mounted on an AM platform to be able to perform automated lay-up of thermoplastic composite material. The first part of this chapter will discuss the main characteristics of this AM platform, which was developed within this doctoral research. However, an elaborate technical description of the design, construction, calibration, validation and optimisation of this platform is beyond the scope of this dissertation. In addition, all necessary conditions of both hard- and software to successfully perform the second stage will be discussed, i.e. i) to pull the composite through the first stage and to push it through the heated nozzle, and ii) the third stage: to deposit the composite strand. In the second part of this chapter, there will be a strong focus on the relation between processing parameters and the resulting morphology of the composite sample production. The main goal is to find the optimal settings to deposit multiple layers of composite material with a limited amount of voids, including a decent fibre distribution and dispersion. The stochastic fibre model, as described in Chapter 2, will be used for this purpose.

3.2 ENDLESS FIBRE ADDITIVE MANUFACTURING: PROCESS WORKFLOW

3.2.1 Development of an AM platform for EFAM

A custom AM platform that is able to handle the composite lay-up forces was developed. It exists of a cartesian system with a build platform moving in X, Y and Z

direction and a stationary deposition unit (Figure 3.1). This configuration allows the use of heavy endless fibre composite or pellet extruders, which can be mounted on a static frame. The added value of a stationary deposition system is the fixed position of cooling, pneumatic and electrical lines for driving, heating and sensing routed to it. Using this configuration, the supply of polymer pellets and fragile, dry fibre bundles is simplified.

The build platform has X and Y dimensions of 264 x 220 mm and exists of a 10 mm thick aluminium plate with high thermal conductivity, resulting in limited temperature gradients in it. The platform has a glued-on 1 mm thick polyetherimide coating and can be operated at temperatures up to 180°C to avoid uneven shrinkage, internal stresses and/or delamination of the extruded composite material. The available build volume in X, Y and Z directions is 250 x 200 x 145 mm.

The build chamber is a thermally insulated, enclosed box to prevent draft or contaminations (Figure 3.2), which can be held at elevated temperatures up to 150°C. The temperature of the build chamber is controlled by radiation and convective heat from the temperature-controlled build platform. This build chamber can eliminate internal stresses in produced parts and improves the interdiffusion between different deposited strands can be improved by deposition at a higher build chamber temperature due to a higher annealing effect, as described by Spoerk et al. [1]. The inner chamber X, Y and Z dimensions are 526 x 513 x 298 mm. The X, Y and Z motors are installed outside the heated chamber, since they have a maximum operating temperature of 75°C. The connection between these motors and their respective driving spindles is achieved by slotted holes (Figure 3.2) in the build chamber wall. Polytetrafluorethylene strips and a silicone rubber membrane are used to seal the build chamber from the environment. An illustration of the complete machine, including its housing and motion/temperature controller systems, can be found in Appendix 4.

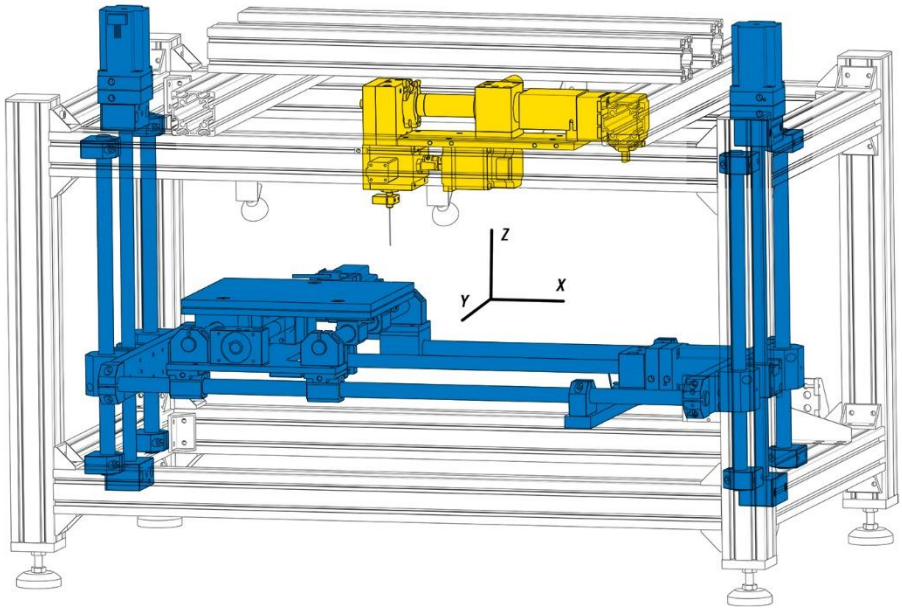

Figure 3.1: Cartesian axes system (blue), allowing movements of the build platform in X, Y and Z direction. An EFAM deposition head (yellow) is mounted on a static machine frame (translucent). Electrical, pneumatic and cooling lines are not shown.

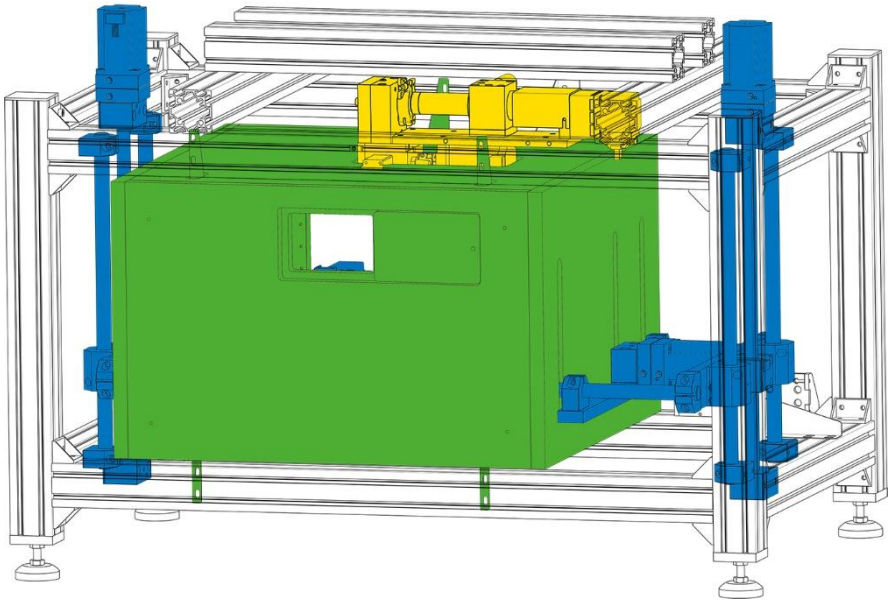

Figure 3.2: Insulated build chamber (green), encapsulating the build platform. X, Y and Z-axis motor drives (blue) can be situated outside the build chamber due to the use of slotted holes (build chamber's right wall).

3.2.2 Requirements for the EFAM puller system

The second stage of the EFAM process exists of a puller mechanism. This unit pulls the fibre bundle through the liquid polymer chamber. The puller system exists of two identical wheels, driven at the same angular velocity ω_w, yet in opposite direction (Figure 3.3). The composite strand is pinched between these wheels by a constant clamping force F_c to provide a frictional force $F_{pul,N}$ (determined in Paragraph 2.7.3) large enough to drag the fibre bundle through the polymer chamber. The wheels' contact surfaces are knurled (Figure 3.4) in order to increase their grip by mechanical interlocking of the serrations on the composite strand.

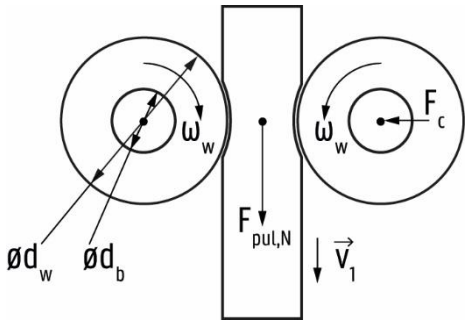

Figure 3.3: Schematic representation of the EFAM puller system, cross-section.

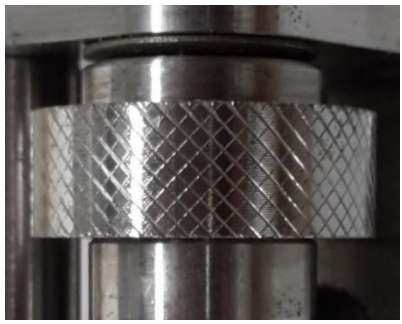

Figure 3.4: Knurled wheel of the puller system of the EFAM deposition head, top view.

The puller mechanism also feeds the pultruded composite material through the heated nozzle, before its deposition. It is assumed that no significant frictional forces are involved in this stage, since the nozzle bore is designed slightly larger than the composites strand's diameter. The required clamping force F_c, pressing the two driving wheels together can be calculated using Equation 3.1. The torque and power required to start up deposition from $v = 0$ up to a pultrusion velocity v_1, at a maximal acceleration rate of a_1, can be calculated by Equation 3.2. The calculations of F_c, P_{min}, T_{min} and ω_w enable the selection of the complete drive system of the puller mechanism.

$$\begin{cases} F_c = \dfrac{F_{pul,N} \; + \; m \, a_1}{f_{c,w}} \\ a_1 = \dfrac{dv_1}{dt} \end{cases} \tag{3.1}$$

$$\begin{cases} T_{min} = \dfrac{F_c}{2 \, \eta_{tr}} \left(d_w \, f_{c,w} + d_b \, f_{b,s} + 2 \, c \right) \; + J \, \alpha \\ \alpha = \dfrac{2 \, a_1}{d_w} \\ P_{min} = \; T_{min} \, \omega_w \\ \omega_w = \dfrac{2 \, v_1}{d_w} \end{cases} \tag{3.2}$$

α	Angular acceleration of the puller wheel	[rad/s²]
a_1	Maximal acceleration of the composite strand	[m/s²]
c	Coefficient of rolling friction between puller wheel and composite strand	[/]
d_b	Equivalent bearing diameter	[m]
d_w	Puller wheel diameter	[m]
F_c	Required clamping force for the pultrusion process	[N]
$F_{pul,N}$	Tensile force required for the impregnation process with N pins. $F_{pul,N}$ is a function of v_1	[N]
η_{tr}	Efficiency of the drive train	[/]
$f_{c,w}$	Dynamic coefficient of friction between the composite strand and puller wheels	[/]
$f_{b,s}$	Equivalent dynamic coefficient of friction of the wheel bearings	[/]
J	Moment of inertia of all rotating components in the EFAM system, reduced to the puller wheel shaft	[kgm²]
m	Total mass of the linearly accelerating objects	[kg]
P_{min}	Minimal power required for the pultrusion process	[W]
T_{min}	Minimal torque required for the pultrusion process	[Nm]
v_1	Nominal linear velocity of the composite strand	[m/s]
ω_w	Angular velocity of the puller wheels	[rad/s]

3.2.3 Kinematics of the EFAM process

In an **EAM process**, such as Fused Deposition Modeling [2]-[3], or in its open-source counterpart Fused Filament Fabrication, a thermoplastic based filament with a circular cross-section with diameter d_1 is fed through a heated nozzle with an internal diameter d_2, which is often a factor 5 to 7 smaller than d_1 (Figure 3.5). This implies that the filament feeding velocity $v_{1,FFF}$ is typically a factor 25 to 50 lower than the polymer's velocity in the nozzle tip, $v_{2,FFF}$. Also, the relative movement of the printhead to the build platform, $v_{3,FFF}$, is significantly higher than $v_{1,FFF}$. This difference in velocity is only possible because of the very limited strength of the liquified thermoplastic polymers used in the process. In the liquid phase, they can be easily deformed, even when they are filled with particles or short fibres.

In an **EFAM process**, the velocity v_1 (Figure 3.6) at which the endless fibre composite is pulled through the liquid polymer chamber should be equal to the velocity of the composite in the nozzle v_2 and to the deposition velocity v_3 (Equation 3.3). The main reason for this is the high Young's modulus of a typical fibre material, which remains in solid phase during processing. During preliminary testing of the EFAM equipment, pultrusion and deposition velocities v_1 and v_3 were matched during the iterative printing of a straight line onto the build platform. In the case that $v_1 < v_3$, the deposited strand was pulled loose from the build platform. In the case of puller wheel slip on the composite strand, the same effect would occur. In the case that $v_1 > v_3$, the unwanted effect of composite strand buckling was noticed, either within the nozzle (causing obstructions) or after deposition (causing an instable composite deposition). The latter effect, where over-deposition leads to a certain of waviness of the deposited fibres was also described by Melenka et al. [4] and can lead to strength and stiffness reduction of the composite [5]. Downstream of the puller system, tensile stresses on the composite strand are limited, provided that the velocities v_1, v_2 and v_3 are properly matched.

$$v_1 = v_2 = v_3 \tag{3.3}$$

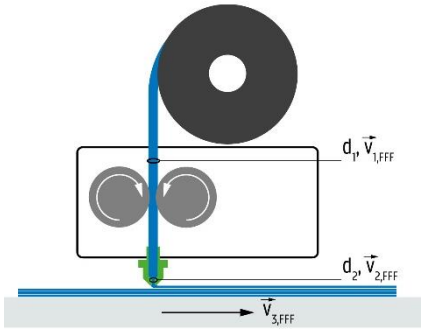

Figure 3.5: Schematic representation of an FDM/FFF process, cross-section.

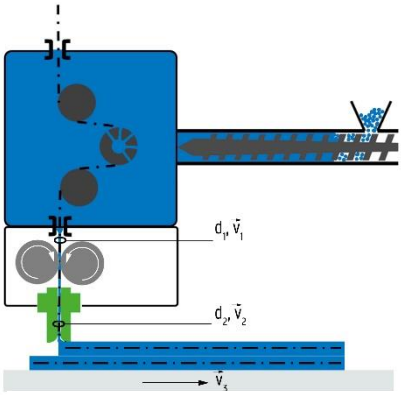

Figure 3.6: Schematic representation of an EFAM process, cross-section.

3.2.4 Composite strand smear out

The third stage of the EFAM process encompasses the liquifying of the matrix material within the composite strand and its deposition. For this purpose, the composite strand has to be guided from an orientation normal to the build platform in the puller system, into an orientation parallel to the build platform after deposition. Therefore, it is important for the deposition nozzle to have a rounded transition to gently guide and smear out the wetted fibre bundle without the occurrence of fibre failure (Figure 3.6). A strength based criterium for a fibre's minimal bending radius to avoid failure of an isotropic fibre such as glass-based fibre was proposed in Section 2.5. The radius R_n of the transition zone of the heated nozzle should be chosen larger than the fibres' minimal bending radius. The tensile stress term σ_t in the determination of the maximum allowable stress should be limited to non-existent during the deposition step, as discussed in Paragraph 3.2.3. The case for $\sigma_{fl} > \sigma_t$ is valid, so Equation 2.35 can be used to determine the minimal value for R_n.

Next to an orientational change to the composite strand in an EFAM process, also its cross-sectional shape is being altered during deposition. It starts as a circular cross-section when being pulled through the pultrusion die and fans out into a cross-section that can be modelled as a rectangle with semi-circular ends (Figure 3.7). Based on Equation 3.3 and the law of mass conservation, it can be said that the

composite strand's cross-sectional area is constant at a given temperature. The temperature of the composite strand immediately after its passage through the pultrusion die is in good approximation equal to the strand's temperature during deposition. As a result, Equation 3.4 gives the relation between d_d, the height h and width w of a deposited composite track. In practice, d_d and h are predefined, the resulting track width is given in Equation 3.5. It must be noted that the relation between h and w is hyperbolical. By changing the inter-path distance s, i.e. the distance between the centres of two adjacent and parallel composite tracks (Figure 3.7), the global density of the resulting composite object can be adapted, as will be discussed in Paragraph 3.2.5.

$$\frac{\pi d_d^2}{4} = (w - h)\, h + \frac{\pi\, h^2}{4} \tag{3.4}$$

$$w = \frac{\pi d_d^2}{4\, h} + h\, \left(1 - \frac{\pi}{4}\right) \tag{3.5}$$

d_d	Pultrusion die diameter	[mm]
h	Layer thickness	[mm]
w	Track width	[mm]

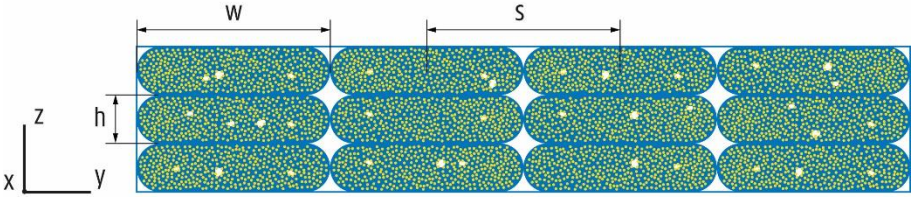

Figure 3.7: Cross-section of a unidirectional EFAM composite, perpendicular to the fibre direction, $s = w$.

3.2.5 Tool path planning

In the context of EAM and EFAM, a tool path can be defined as the relative movement of an extruder/deposition nozzle in relation to the build platform, which is necessary

to build up a three-dimensional object. The tool path for production of a unidirectional composite layer will consist of parallel tool paths with an inter-path distance s. A value for s equal to w ensures that the individual tracks are making contact (Figure 3.7, Figure 3.8), but this inherently leads to a certain macroscopic void volume fraction $V_{v,mac}$ in between the individual deposited tracks, as determined in Equation 3.6. By reducing ζ, being the ratio of layer thickness versus track width, while respecting Equation 3.5, $V_{v,mac}$ can be reduced. Note that $V_{v,mac}$ refers to the macroscopic voids in between composite tracks, not including the microscopic voids within an individual composite track after its deposition ($V_{v,mic}$). The total void fraction $V_{v,tot}$ of an EFAM composite object can be calculated using Equation 3.7. It must be noted that the void fraction V_v as determined in Section 2.9 is not necessarily equal to $V_{v,mic}$, since the deposition step might have an influence on the void fraction within the composite strand.

$$V_{v,mac} = \frac{h}{w}\left(1 - \frac{\pi}{4}\right) = \zeta\left(1 - \frac{\pi}{4}\right) \tag{3.6}$$

$$V_{v,tot} = V_{v,mac} + (1 - V_{v,mac})\, V_{v,mic} \tag{3.7}$$

h	Layer thickness	[mm]
$V_{v,mac}$	Macro-void volume fraction	[/]
$V_{v,mic}$	Micro-void volume fraction	[/]
$V_{v,tot}$	Total void volume fraction	[/]
w	Track width	[mm]
ζ	Ratio of layer thickness versus track width	[/]

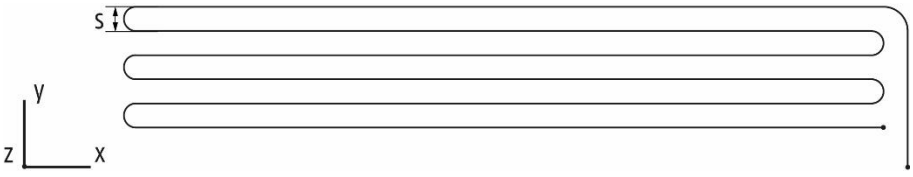

Figure 3.8:Tool path of a single layer EFAM test specimen, top view.

In theory, it is possible to reduce or even eliminate macro-voids in a composite object by depositing slightly overlapping tracks, i.e. choosing $s < w$. In practice, a macro-void filling factor ξ between 0 and 1 is determined experimentally, in order to obtain

an optimum between density and printability (Equation 3.8). In this, $\xi = 0$ corresponds to $s = w$ and a $V_{v,mac}$ as calculated in Equation 3.6, while $\xi = 1$ corresponds to $s = s_{min}$ (Equation 3.9) and $V_{v,mac} = 0$. However, due to limitations in the deformability of the strands being deposited, a situation where a track is partially deposited on top of another track in the same layer, instead of filling up the existing voids, can occur for high values of ξ (Figure 3.9). This effect leads to a reduced printability and will induce fibre failure during deposition. In practice, an ξ-value of around 0.5 is realistic. In this case the lower half of the rhombic macro-void cross-sections (Figure 3.7) are filled (Figure 3.10).

$$s = w - \xi\, h\left(1 - \frac{\pi}{4}\right) \tag{3.8}$$

$$s_{min} = w - h\left(1 - \frac{\pi}{4}\right) = \frac{\pi\, d_d^2}{4\, h} \tag{3.9}$$

d_d	Pultrusion die diameter	[mm]
h	Layer thickness	[mm]
s	Inter-path distance	[mm]
s_{min}	Theoretical inter-path distance for zero voids	[mm]
w	Track width	[mm]
ξ	Void filling factor	[/]

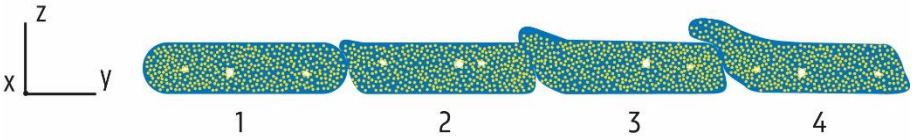

Figure 3.9: The effect of partially overlapping composite tracks, where $s \ll w$ and $\xi \approx 1$. The order of strand deposition is indicated by increasing numbers. Cross-section of a single layer composite perpendicular to the fibre direction

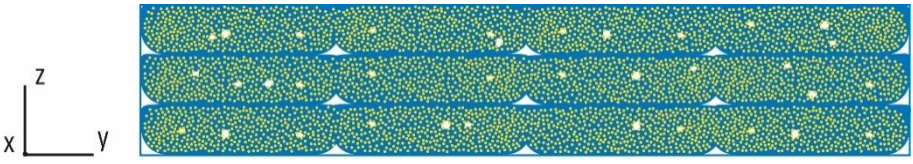

Figure 3.10: Reduction of the macro-void content by slightly overlapping the composite tracks, where $\xi = 0.5$. Cross-section of a triple layer composite perpendicular to the fibre direction.

Previously, the relation between the parameters layer thickness, track width, inter-path distance and their effect on the void volume fraction was described. These parameters completely define the tool path coordinates of linear movements during the production process. In addition, also the characteristics of bends in the tool paths and the global print strategy must be described. For EFAM production of a single layer unidirectional test specimen, a path as shown in Figure 3.8 must be followed during deposition. Preferably, endless fibres are not cut at the specimen's ends during the printing process. This entails that the fibres have to make a bend of 180° at both ends of the specimen. Similar to the minimal bending radius determined for spreader pins (Section 2.5), care should be taken to avoid fibre failure. A considerable difference is that in this situation, the fibres' degrees of freedom are not restricted by a rigid spreader pin. If the matrix material, which surrounds the fibres during the deposition of a 180° bend is in the liquid phase, fibres can migrate within this matrix and find an equilibrium with minimal fibre stresses.

For processing purposes, the diameter of the deposition nozzle d_2 is chosen slightly larger than the pultrusion die diameter d_d, and thus the composite strand's diameter. This implies that the tool path length will slightly deviate from the actual length of the extruded composite strand, when deposition on a curved path (Figure 3.11). When these small differences in travel length accumulate, a situation as described in Paragraph 3.2.3 occurs. Applying a nozzle radius compensation on the desired tool path (Figure 3.12) can solve this issue and was implemented in the tool path planning algorithm.

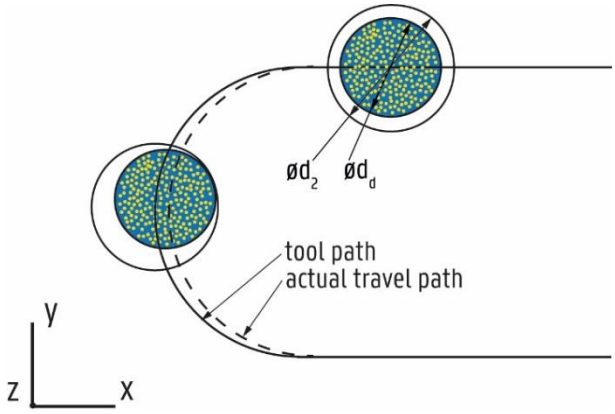

Figure 3.11: Schematic representation of the difference between the planned and actual composite track travel path during a 180° bend.

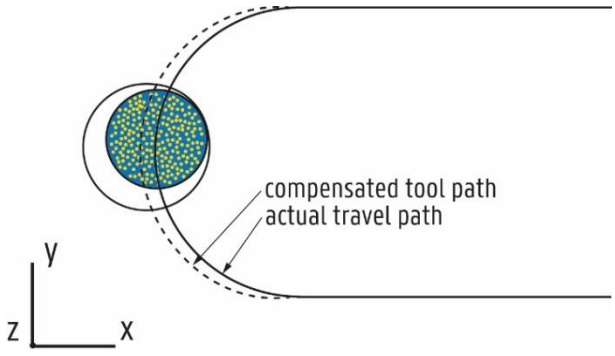

Figure 3.12: Compensated tool path in a 180° bend.

3.3 EFAM PRODUCTION PARAMETER SELECTION

This section will discuss all relevant parameters for EFAM production of a unidirectional composite, based on the glass fibre and PA12 components as described in Paragraph 2.9.1. Production will be done using the fully automated impregnation and deposition device as described in Section 2.10, mounted in an AM platform as described in Section 3.2. Parameters that will be discussed include the

pultrusion die diameter and related V_f, processing temperatures throughout the complete device, minimal bending radius to which a fibre bundle may be subjected, deposition velocity, and an 'optimal' layer thickness and inter-path distance.

3.3.1 Fibre volume fraction and pultrusion die diameter

For the sake of printability, a V_f of around 40 vol% glass fibres will be pursued throughout Chapter 3 and Chapter 4. Using Equation 2.36, the required pultrusion die diameter was calculated to be 1.2 mm.

3.3.2 Processing temperatures

The processing temperatures used in the impregnation device have an important effect on a polymer's melt viscosity, as was discussed in Section 2.3. Different temperature settings for the micro extruder's barrel, the spreader pins, the deposition nozzle and the build platform were determined by trial and error. All zones that can be temperature controlled individually throughout the EFAM process are indicated in Figure 3.13.

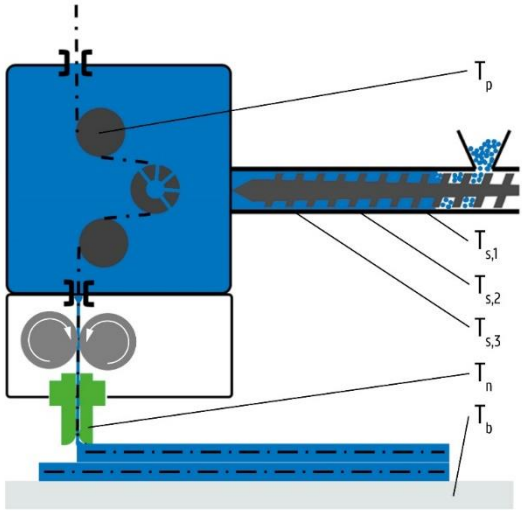

Figure 3.13: Nomenclature of all temperature controlled zones in the EFAM deposition system.

The temperature of the extruder's hopper and feed zone intake must be kept below the glass transition temperature T_g of the PA12 polymer. This guideline is required to avoid polymer pellets sticking to the hopper wall or individual pellets clumping together and causing obstructions. In this case, a feeding zone temperature $T_{s,1}$ of

30°C was chosen. This value is below the T_g of PA12, being 44°C (determined in a dynamic mechanical analysis (DMA) as the maximal loss modulus E'' at a heating rate of 1 K/min and a frequency of 1 Hz, using ISO 6721-11:2012, cf. Appendix 3.4).

Initially, the extruder was operated without the EFAM liquid polymer chamber attached to it. The temperatures along the barrel were set slightly higher than the melt peak of PA12 (determined to be 180.8 ± 0.1°C by ISO 11357-1:2016, cf. Appendix 3.5). The progressively increasing barrel temperatures were fine-tuned until a homogenous and completely liquified extrudate, with no visual discoloration of the freshly extruded PA12, was obtained. Finally, a temperature $T_{s,2}$ of 195°C was set in the compression zone, while $T_{s,3}$ was set at 215°C in the metering zone.

For a deposition velocity v_1 of 2 mm/s, a spreader pin temperature T_p of 240°C, a nozzle temperature T_n between 225°C and 235°C and a build platform temperature T_b between 100°C and 120°C resulted in a depositable composite strand. Especially the adhesion quality between the build platform and the first composite layer proved to be strongly dependent on the settings of v_1, T_n and T_b. These parameters relate to the heat flow into the composite strand, and thus its temperature during deposition.

Choosing temperature values that were too high during the trial and error-based determination of temperature settings, resulted in a colour change of the deposited PA12 matrix material, indicating chemical degradation. Degradation can be quantified by Gel Permeation Chromatography (GPC), but also a study of heat flux curves as a function of temperature, measured in Differential Scanning Calorimetry (DSC) can give a first indication of polymer degradation.

3.3.1 Minimal bending radius

Filling in the in Equation 2.35 with the characteristic values of the glass fibre being used in the EFAM process, a minimal bending radius $R_{f,min}$ of 1.3 mm was found. In the EFAM setup as described in Section 2.10, the impregnation pins have radii of 4.0 mm and the deposition nozzle a radius of 3.0 mm to avoid fibre breakage before deposition. When printing a unidirectional composite, using a toolpath similar to the one in Figure 3.8, but having 12 parallel tracks, a specimen end as shown in Figure 3.14 is being observed. It can be seen that fibres tend to slightly unbend and curve

upwards when being deposited on paths with high curvature. This phenomenon was described as 'tow pull-up' by Lukaszewicz [6].

Figure 3.14: The combined effect of partially overlapping composite tracks and tow pull-up in regions of high path curvature.

3.3.1 Deposition velocity

During preliminary testing of the EFAM technique, deposition velocities between 0.5 and 4 mm/s were used. The lowest velocities resulted in a well impregnated and smeared out composite with no fibre breakage. Highest velocities resulted in a moderately impregnated composite and some fractured fibres. Preliminary test showed that a deposition velocity of 2 mm/s led to a good trade-off between deposition velocity and composite quality.

3.3.2 Layer thickness and inter-path distance

In a preliminary test, it was found that the lay-up of a strand at a layer thickness of 0.6 mm resulted in the best adhesion to the bed and to successive deposited layers. Using Equations 3.5 and 3.8, a required strand width of around 2.2 mm was calculated in order to create a composite with a limited $V_{v,mac}$.

3.4 EFAM COMPOSITE MORPHOLOGY

3.4.1 Materials and methods

3.4.1.1 Production of single and dual layer composites

All samples were produced using the EFAM technique as described in as described in Section 2.10, with the 'Activepin' method, a pultrusion die with diameter 1.3 mm and a pultrusion speed of 1 mm/s. Temperature of the melt chamber and the deposition nozzle was set at 240°C, the build platform's temperature was chosen 110°C. h was chosen 0.6 mm and s was set at 2.2 mm.

3.4.1.2 Optical microscopy on composite cross-sections

Both single and dual layer composite samples were embedded in 'Epofix', a cold curing epoxy from Struers (Ballerup, Denmark). The embedded samples were cut perpendicular to the fibre direction and polished up to a 4000 grit silicon carbide. Micrographs were made on a Keyence (Osaka, Japan) VHX-2000 digital microscope at a magnification of 250. This magnification allows for studying fibre distribution and dispersion, processing-morphology effects and void formation in the composite.

3.4.1.3 Quantifying fibre dispersion and distribution

Fibre dispersion and distribution was quantified using the methodology in Paragraph 2.9.1.7. However, this methodology is still in preliminary phase. Another interesting method of fibre distribution and dispersion characterisation could be the methodology as proposed by Morisita [7] and used by Bechtold and Ye [8].

3.4.2 Results and discussion

3.4.2.1 Optical microscopy results

A micrograph of a single layer composite cross-section was produced and analysed (Figure 3.15, left). Visually, it can be noticed that the matrix material of the individual strands is interdiffused. However, spots with a lower fibre content can be distinguished in the weld zones between the six deposited strands. Within a single strand, fibres seem to have a decent distribution, which will be characterized in Paragraph 3.4.2.2. On the micrograph of a dual layer composite (Figure 3.15, right), it can be noticed that the interdiffusion between adjacent strands of the second layer

is limited due to larger triangular voids, as also described in Paragraph 3.2.5. Also, between the first and the second layer, a moderate adhesion can be noticed, recognised by the small (darker) voids. Both phenomena are related to each other. Due to its limited adhesion on the previous layer, a newly deposited strand can curl-up slightly during the deposition process, causing the triangular voids. In Chapter 4, these effects will be analysed and minimised by optimising layer thickness, inter-path distance and nozzle temperature settings.

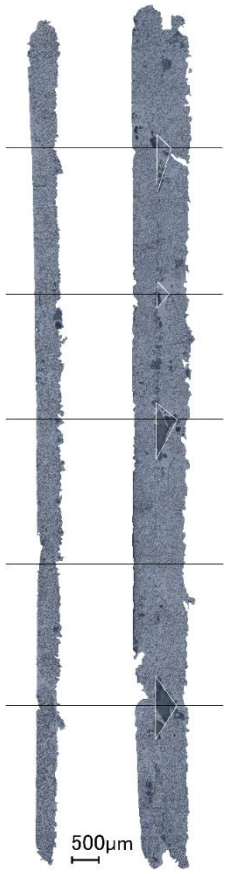

Figure 3.15: Single layer cross-section, weld zones shown as black lines (left). Dual layer cross-section with triangular voids marked in white (right). Both specimens were produced with the left side of the cross-section on the build platform.

3.4.2.2 Quantifying fibre dispersion and distribution

A circular section with a diameter of 0.5 mm in the micrograph in Figure 3.15, left and a circular section with diameter 1 mm (including the interface between the two layers) in Figure 3.15, left, were considered for the quantification of the fibre dispersion and distribution, as described in Paragraph 2.9. All inter-fibre distances d_{ij} were calculated and are shown in histograms of Figure 3.16, left and middle. For both data sets, a decent fit with an idealised distribution (Figure 3.16, right) was found. For both single layer and dual layer composites, statistical parameters such as mean inter-fibre distance and its standard deviation, skewness and kurtosis are given in Table 3.1 and are very similar, indicating similar fibre distribution behaviour.

The standard deviation of the inter-fibre distances correlates with the fibre distribution in the matrix material. When the fibres are well distributed over the complete circular section, standard deviation will be maximal. The standard deviation values in Table 3.1 have a value of about 46% of their mean inter-fibre distance, indicating a decent fibre distribution.

The positive skewness, meaning that the mass of the distribution is concentrated left and the histogram has a right tail, shows that there is a light tendency of the fibres to coagulate, i.e. have a bad dispersion. Since negative inter-fibre distances are physically impossible, the right tail is larger than the left tail. The occurrence of fibres that are packed too close to each other can cause high local stresses in the matrix material and will play an important role in failure mechanisms. For this reason, a non-skewed distribution (skewness is zero) is preferred. Results for both a single and dual layer composite are very similar, indicating similar coagulation behaviour.

It can be noticed that the excess kurtosis is negative and similar for both single and dual layer composites. Visually, it can be seen that mass of the distribution is concentrated in intermediate values than in the mean value and outliers. This parameter describes the shape of the histogram and is for that reason an important parameter to fully characterize the composite material.

After comparing the single layer and dual layer composites, it is clear that both have very similar statistical parameters, showing that the morphology of both composites is very similar (Figure 3.15). This statistical technique for characterization could be

an interesting way for quantifying fibre dispersion and distribution in a composite, especially when larger sample cross-sections can be evaluated.

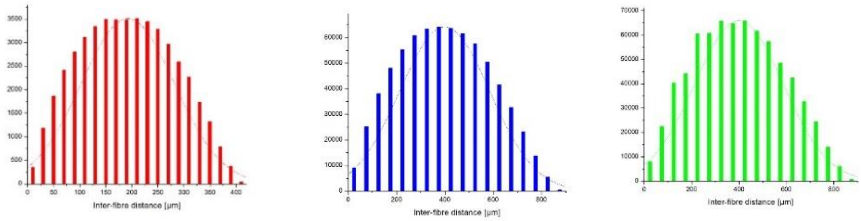

Figure 3.16: Left: inter-fibre distances histogram on a 0.5 mm circular section of a single layer composite. Middle: inter-fibre distances histogram on a 1 mm circular section of a dual layer composite. Right: inter-fibre distances histogram on a 1 mm circular section of an idealised dual layer composite with hexagonal close packed fibres.

Table 3.1: Gaussian distribution parameters characterizing fibre distribution and dispersion of a single and dual layer CFAM composite.

	Single layer	Dual layer
Mean inter-fibre distance	192	399
Standard deviation	89	187
Skewness	0.088	0.108
Excess kurtosis	-0.85	-0.80

3.4.3 Conclusions

The aim of this chapter was to evaluate the feasibility of the use of the EFAM 'ActivePin' melt impregnation technique in an AM process. Firstly, the deposition strategy was described and all relevant processing parameters were calculated using the proposed models or were determined by trial-and-error. In order to demonstrate the EFAM process, both single and dual layer unidirectional endless glass fibre – PA12 composites with six parallel composite strands and a layer thickness of 0.6 mm were successfully produced.

The morphology of the produced composite samples was analysed. The single layer composites showed a limited void content and a proper interdiffusion of the matrix material in the weld zones between the adjacent strands. In the dual layer

composites, some macroscopic triangular voids were found in between the top surface of the first layer and several adjacent strands of the second layer.

On the micrographs of the composites' perpendicular cross-section, fibre distribution and dispersion were studied. Analysis of the inter-fibre distances proved to be an interesting method to quantify the fibres' distribution and dispersion. Parameters such as mean inter-fibre distance and its standard deviation, skewness and (excess) kurtosis were used to explain effects such as coagulated fibres.

Considering the conclusions above, this preliminary research on the production of EFAM composites is deemed to be successful, however, optimisation and further research of the process will be necessary to make EFAM an industrially viable production technique. In Chapter 4, parameters such as layer thickness and deposition nozzle temperature will be analysed and - where possible - optimised to enhance the composite's quality.

3.5 REFERENCES

[1] M. Spoerk *et al.*, "Polypropylene Filled With Glass Spheres in Extrusion-Based Additive Manufacturing: Effect of Filler Size and Printing Chamber Temperature," *Macromol. Mater. Eng.*, vol. 303, no. 7, 2018.

[2] S. S. Crump, "Apparatus and method for creating three-dimensional objects," 1992.

[3] S. S. Crump, "Modeling apparatus for three-dimensional objects," no. 19, p. 20, 1994.

[4] G. W. Melenka, B. K. O. Cheung, J. S. Schofield, M. R. Dawson, and J. P. Carey, "Evaluation and prediction of the tensile properties of continuous fiber-reinforced 3D printed structures," *Compos. Struct.*, vol. 153, pp. 866–875, 2016.

[5] H. M. Hsiao and I. M. Daniel, "Effect of fiber waviness on stiffness and strength reduction of unidirectional composites under compressive loading," *Compos. Sci. Technol.*, vol. 56, no. 5, pp. 581–593, 1996.

[6] D. H. J. A. Lukaszewicz, C. Ward, and K. D. Potter, "The engineering aspects of automated prepreg layup: History, present and future," *Compos. Part B Eng.*, vol. 43, no. 3, pp. 997–1009, 2012.

[7] M. Morisita, "Iσ-Index, a measure of dispersion of individuals," *Res. Popul. Ecol. (Kyoto)*., vol. 4, no. 1, pp. 1–7, 1962.

[8] G. Bechtold and L. Ye, "Influence of fibre distribution on the transverse flow permeability in fibre bundles," *Compos. Sci. Technol.*, vol. 63, no. 14, pp. 2069–2079, 2003.

4 MECHANICAL PROPERTIES OF EFAM COMPOSITES

4.1 INTRODUCTION

In this chapter, the mechanical properties of unidirectional endless fibre reinforced composites, produced by the in-house developed EFAM technology are investigated. Due to the layer-wise building process, a relatively low strength is to be expected along a specimen's 33 direction (parallel to the z-axis of the AM platform, cf. Figure 3.1) compared to its 11 direction. Different mechanical analyses (Table 4.1) to test relevant inter-layer properties of a unidirectional EFAM composite could be performed, however due to practical considerations, not all tests are applicable within this research.

Table 4.1: Methods to determine inter-layer properties of a unidirectional EFAM composite, proposed testing standards, sample height and layer amount to be deposited, using a layer thickness of 0.6 mm.

Testing method	Standard	specimen height [mm]	Layer amount [/]
Tensile properties (33 direction)	ISO 527-5	250	417
Mode I interlaminar fracture toughness (DCB)	ASTM D5528-01	3.4 – 4.7	5 - 8
Mode II interlaminar fracture toughness (ENF)	ASTM D7905	3 - 5	5 - 9
Flexural properties	ISO 14125	2	3-4
Short beam strength	ASTM D2344	6	10

A tensile test along a specimen's 33 direction would require a prohibitively large number of layers and specimen length (Table 4.1). The deposition of more than four layers led to a higher frequency of production errors due to thermal warping effects in the current AM platform setup, which has to be avoided to obtain accurate data. Both mode I and II of interlaminar fracture toughness testing, respectively being double cantilever beam (DCB) testing and end notched flexure (ENF) testing, are adequate to characterise inter-layer behaviour. However, due to their complex

nature, requiring a notch in between successive layers to be realised during deposition, these methods are less suited for an initial determination of inter-layer behaviour. Both DCB and ENF tend to have quite some scatter in the test results, especially the ENF test is influenced by frictional forces occurring within the notch [1], [2]. This can lead to unrealistic interlaminar toughness values in the test results. It can be said that flexural and short beam tests are easier to perform and interpret on the condition that no macro-delaminations are being formed during testing. If so, frictional forces in the delaminated zone can skew the test results in a way similar to the mechanism occurring during ENF testing. For reasons of printability, printing time, accuracy and availability of the testing equipment, the focus in Chapter 4 will be on flexural testing.

In previous research, it was found that nozzle temperature and layer thickness are important AM processing parameters contributing to the quality of the interlayer adhesion in Extrusion based Additive Manufacturing (EAM) and thus, influence mechanical properties of EAM end-products. In this chapter, the main effects of layer thickness, nozzle temperature, and their interactional effects on the flexural properties and deformation and fracture mechanisms of unidirectional EFAM composites will be evaluated and related to the material's morphology.

4.2 MATERIALS AND METHODS

4.2.1 Materials

Rilsamid AMN O TLD, as described in Paragraph 2.9.1.1 was used as the matrix material. For reference, its flexural properties were determined according to ISO 178:2010. The flexural modulus was found to be 1034.6 ± 29.2 MPa, the flexural strength to be 45.6 ± 0.6 MPa. Stress-strain curves in flexural mode can be found in Appendix 3.2. Aditionally, the polymer's tensile properties were determined according to ISO 527-1:2012 and ISO 527-2:2012. The tensile modulus was found to be 1291.2 ± 282.8 MPa and tensile strength 43.8 ± 4.5 MPa. Stress-strain curves in tensile mode can be found in Appendix 3.3. The density of the material was determined using the immersion method described in ISO 1183-1:2004 and has a value of 1009.2

± 8.8 kg/m³. This data is useful to estimate the final composite's mechanical properties, based on the rule of mixtures.

StarRov LFTplus Direct Roving 853, as described in Paragraph 2.9.1.1 was used as the reinforcing material in the flexural specimens. The tensile modulus of the glass fibre was determined to be 57098.3 ± 2443.2 MPa, tensile strength to be 1632.6 ± 269.7 MPa. The density of the fibre material is 2540.0 kg/m³.

4.2.2 Printing parameters and sample preparation

For each sample, bars with a length of 230 mm, a height of three layers and a width of six parallel tracks per layer were produced using the tool-path, as shown in Figure 4.1. The track was deposited starting at the rightmost path end, following the complete trajectory anticlockwise as a continuous path and finishing the layer at the other end. Two additional layers were deposited using the same trajectory and an identical layer thickness. Two specimens were cut from each bar's centre. The outer sections of the produced bars were discarded to avoid edge effects due to the 180° turns in the composite tracks and acceleration effects particular for this additive manufacturing process.

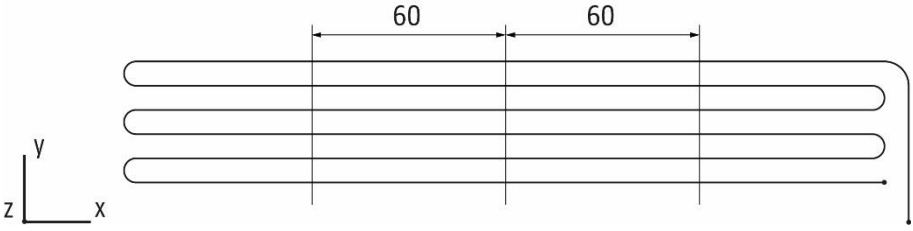

Figure 4.1: Top view of the deposition trajectory.

During pretests, the optimal processing parameters for obtaining a decent volumetric filling with limited intra-layer and inter-layer voids were determined (cf. Chapter 3). Parameters of paramount importance with respect to this are layer thickness h, the inter-path distance s and the void filing factor ξ.

In pretests, depositing a 1.2 mm diameter strand into a layer thicknesses of 0.8 mm resulted in limited to no build platform and inter-layer adhesion, regardless of the value of s, therefore making the deposition process unstable. On the other hand, layer thicknesses of 0.5 mm, regardless of the value of s, resulted in excessive fibre failure during lay-up, resulting in a higher surface roughness and reduced

mechanical properties. Taking into account these technical boundaries, two levels of layer thickness will be tested: 0.6 mm as a 'low' level and 0.7 mm as a 'high' level. The width of an individual track can be calculated as a function of the chosen layer thickness h and the wipe-off die diameter d_d, using Equation 3.5. For each value of h, the corresponding value of s was calculated using Equation 3.8. The same void filling factor ξ was used for every sample, resulting in equal sample densities.

4.2.3 Experimental design

Flexural samples were produced with two different nozzle temperatures: 225.0°C as a 'low' and 235.0°C as a 'high' level, and this both for two levels of layer thickness: 0.6 mm as a 'low' and 0.7 mm as a 'high' level. The relevant processing parameters for the four resulting samples are listed in Table 4.2. They are labelled as XT - YH, wherein both X and Y can be 'high' (H) or 'low' (L), respectively for temperature (T) and layer thickness (h).

Table 4.2: Relevant processing parameters for the four different composite samples.

	LT-Lh	LT-Hh	HT-Lh	HT-Hh
T_n [°C]	225.0	225.0	235.0	235.0
T_b [°C]	110.0	110.0	110.0	110.0
h [mm]	0.6	0.7	0.6	0.7
s [mm]	2.2	1.9	2.2	1.9
v_1 [mm/s]	2.0	2.0	2.0	2.0

Three important criteria should be fulfilled before conclusions can be drawn from flexural test results of the four different samples:

i) The amount of deposited composite material should be equal for all samples. Theoretically, this requirement should be met since all samples contain three layers of six parallel identical strands, which have identical lengths. Nonetheless, this will be validated in a two-way variance analysis, comparing the mean mass of each sample.

ii) Also the samples' fibre and matrix mass fractions should be equal to be able to make a fair comparison of their flexural properties. Since fibre and matrix mass fractions are linearly dependent, only one of these two

conditions should be checked. The fibre mass fraction criterium will be tested for in a two-way variance analysis.

iii) The fibre distribution and dispersion should be similar and homogenous at best for a fair comparison of the samples. Both characteristics can be checked visually or quantified by statistical analysis of the inter-fibre distance, as described in Paragraph 4.2.6.

4.2.4 Specimen mass determination

Five produced flexural specimens per sample were weighted using a Precisa XR 205SM-DR apparatus (Dietikon, Switserland). Mass comparison of all specimens within a sample was used as quality control and to exclude differences in matrix or fibre flow during specimen production. A two-way variance analysis will comparing the mean mass of each sample.

4.2.5 Fibre mass fraction determination

For each sample, three specimens were incinerated to determine the fibre mass fraction, as described in Section 2.2. All specimens were weighted using a Precisa XR 205SM-DR scale before and after incineration in a Nabertherm LT 6/11/R7 (Lilienthaal, Germany) oven for two hours at a temperature of 600°C. The values for V_f were calculated using Equation 2.10. A two-way variance analysis will comparing the mean V_f of each sample.

4.2.6 Composite morphology evaluation

A specimen of each sample was embedded in an Epofix epoxy from Stuers (Ballerup, Denmark) and two cross-sections perpendicular to the specimen's fibre orientation were polished using progressively finer SiC sanding paper up to grade P4000. All micrographs were made on a Keyence (Osaka, Japan) VHX-2000 optical microscope with a VH-Z250R lens at a magnification of x250.

The fibre distribution and dispersion of a circular cross-section within the specimens could be quantified using the methodology described in Paragraph 2.9.1.7, or visually analysed. Due to the large cross-sectional area of a complete composite specimen, a full stochastic quantification proved to be very computationally intensive, so a visual analysis was preferred.

4.2.7 Flexural testing

The protocol for three-point flexural testing is based on the ISO 14125:1998 standard, for the material class III in the 0° principal direction. Nominal sample sizes recommended by the standard are 60 x 15 x 2 mm, due to the discrete nature of fixed track widths and layer heights in EFAM, slight deviations from this nominal dimensions are possible.

The specimens were conditioned and prepared according to the abovementioned standard. All flexural tests were performed on an Instron 4464 machine with a 2 kN load cell, a test velocity of 1 mm/min and a span length of 40 mm. The face of the specimen which was in contact with the build platform during processing is typically smooth and is put onto the two supports during the three-point flexural test (Figure 4.2). This means that the indenter comes down on the 'top surface' of the specimen, thus compressing any surface roughness that may exist during the begin of the flexural test, rather than this roughness being able to introduce artefacts into the measurements, by initiating tear in the tensile-loaded bottom half of the flexural specimen. Eight specimens per sample were tested, which is more than the minimum of five specimens required by the standard. Data that will be gathered from the flexural tests include flexural modulus E_{flex}, flexural strength σ_{flex} and strain at flexural strength ε_{flex}.

Failures initiated by interlaminar shear are not acceptable by the standard. However, since the distinction between tensile, compressive and interlaminar shear failure modes is useful to get an insight into layer thickness and/or nozzle temperature dependent fracture mechanisms, interlaminar shear initiated failure specimens were taken into account in the flexural properties results of this research.

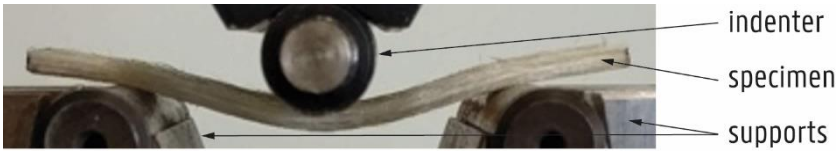

Figure 4.2: Setup of a flexural test, the specimen being under a flexural load.

4.3 RESULTS AND DISCUSSION

4.3.1 Specimen mass results

Comparison of the four different samples' mean mass (Figure 4.3) in a two-way variance analysis shows that neither layer thickness nor nozzle temperature has a significant effect on the specimens' mass at a 0.95 significance level (Appendix 5.1). Therefore, processing parameter related flow variations of the composite material can be excluded. This means that criterium i), mentioned in Section 4.2.3 is met. Also, there was no significant variation in the specimen mass within all samples, indicating that the process is reproducible for all tested samples.

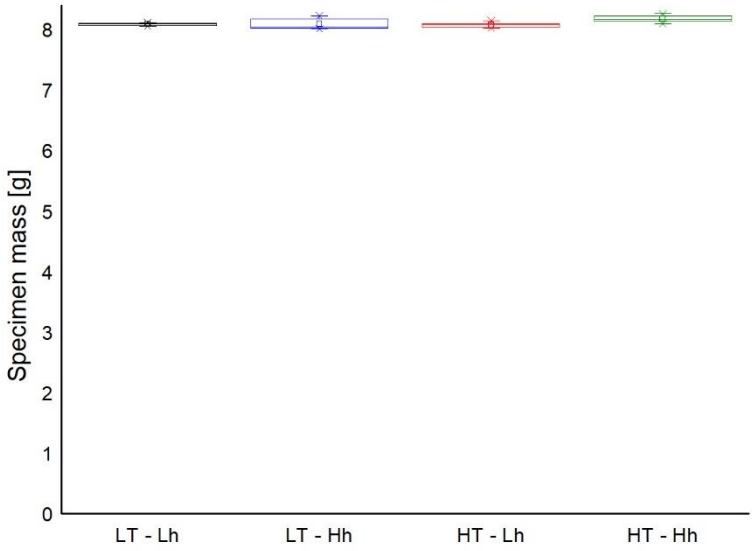

Figure 4.3: Box and whisker plot of each sample's specimen mass.

4.3.2 Sample fibre volume fraction results

Comparison of the four different samples' mean V_f (Figure 4.4) in a two-way variance analysis shows that neither layer thickness nor nozzle temperature has a significant effect on the specimens' matrix volume fraction at a 0.95 significance level (Appendix 5.2). Therefore, processing parameter related flow variations of the composite material can be excluded and criterium ii), mentioned in Section 4.2.3 is fulfilled.

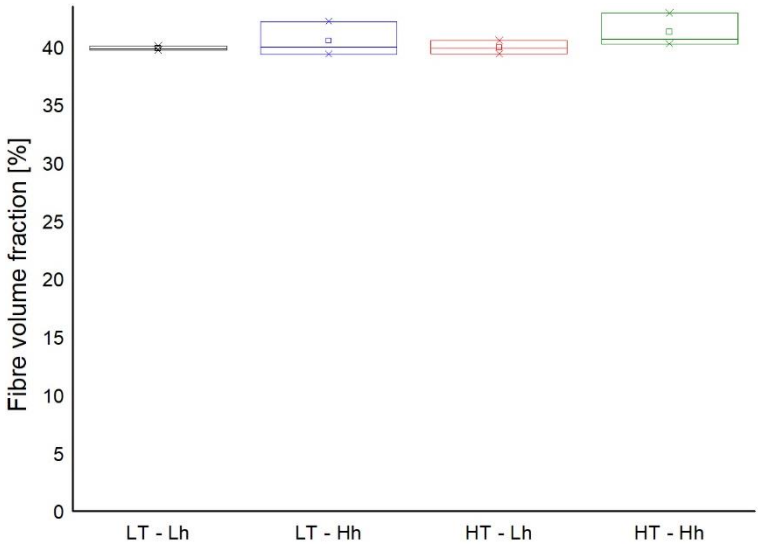

Figure 4.4: Box and whisker plot of each sample's fibre volume fraction.

4.3.3 Sample morphology evaluation results

In Table 4.3, micrographs of all samples are given. For all specimens, the intra-layer adhesion, i.e. the adhesion between the different tracks within one layer, looks decent. However, clear differences in the inter-layer adhesion were observed. The Lh specimens show a decent inter-layer adhesion and have a matrix rich zone in between two successive deposited layers, whereas the Hh specimens show large macroscopic inter-layer voids and large regions with limited to no connection between successive layers. Due to their smaller layer thickness, the overall thickness of the Lh specimens is smaller, however, their specimen width looks visually very similar to the width of the Hh specimens. This can be explained by the higher void volume fraction in the Hh specimens.

There was no clear difference observed between the LT and HT specimens, mechanical analyses will be necessary to map the effects of nozzle temperature on the quality of the deposition process.

Table 4.3: Micrographs of the different produced samples. Specimens were produced with the right side of the cross-section on the build platform.

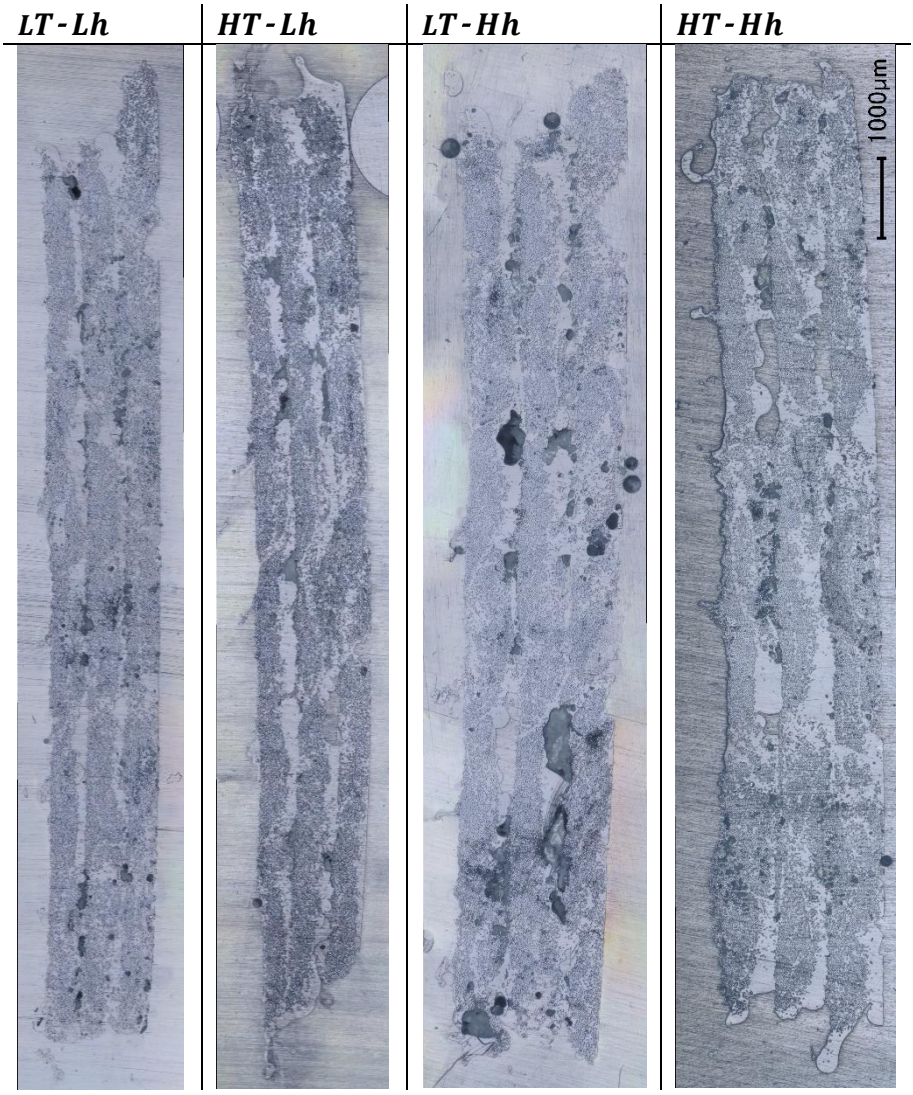

4.3.4 Flexural testing results

A representative flexural curve for every sample is depicted in Figure 4.5, which shows that at least the elastic section is quite reproducible for specimens within a single XT - Yh type. The figure also shows that for all Lh specimens, the curves fall to zero-load, consistent with cracking, while the Hh specimens maintain a certain load bearing capacity after delamination. The observation is made that the Lh specimens are fully fractured after flexural testing, whereas the Hh samples tended to delaminate. This enabled all three layers to deform independently (but with the occurrence of frictional forces in between the successive layers) during flexural testing, mainly resulting in elastic deformations within the individual layers. A full analysis of the failure behaviour was performed in Paragraph 4.3.4.1. The complete sets of flexural stress-strain curves of all four samples are shown in Appendix 6.1 to 6.4.

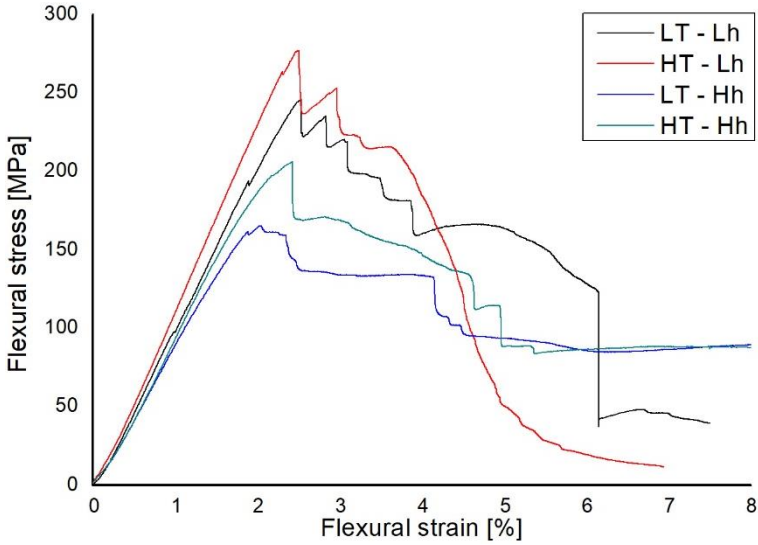

Figure 4.5: Representative flexural stress-strain curve for the four tested samples.

4.3.4.1 Fracture mechanisms

Table 4.4 summarizes the different fracture mechanisms that where observed for the samples after the flexural test. This table describes which layers were cracked (= a brittle break across the layer) or delaminated (= separation of at least one fibre strand of a layer from another layer, noted as 'DL' in Table 4.4) from one another. 'crack 1+2+3' can be considered a complete crack mode of failure, implying continued

adhesion between matrix and fibre throughout the complete flexural test, as well as a good interlaminar adhesion. The composite fails as a whole, and not on the layered aspect of being 3D printed. This is a best-case result for the printing methodology. 'DL 1-2 + 2-3' can be considered a complete delamination mode of failure, implying insufficient adhesion between all layers. This is a worst-case result for the printing methodology, as the part fails below the stress and strain levels of the composite material, but rather due to geometric inadequacy.

In Table 4.4, the most common failure mode per sample is highlighted in yellow. It is immediately evident that:

- the Lh specimens tend to fail in full crack mode
- the Hh specimens tend to fail in full delamination mode.

This is the case for 7 out of 8 HT - Lh and LT - Hh specimens respectively. The LT - Lh and HT - Hh have more variation in their failure mode, but still the trend remains. None of the Lh specimens delaminate on both interlayer adhesions and none of the Hh specimens crack in all three layers. These results are in line with the morphology evaluation, made in Section 4.3.3: the larger layer thickness (Hh) results in poor inter-layer adhesion, shifting the failure mechanism to delamination.

Table 4.4: Fracture mechanisms observed for the four samples, by amount of fractures and/or delaminations.

	LT-Lh	LT-Hh	HT-Lh	HT-Hh
Crack 1 + 2 + 3	4	0	7	0
Crack 1 + 2 + 3 DL 1 - 2	2	0	1	0
Crack 1 + 2 + 3 DL 1 - 2 and 2 - 3	0	1	0	0
Crack 2 + 3 DL 1 - 2	2	0	0	1
Crack 2 + 3 DL 1 - 2 and 2 - 3	0	0	0	1
Crack 3 DL 1 - 2 and 2 - 3	0	0	0	1
DL 1 - 2 and 2 - 3	0	7	0	5

Another trend is the higher crack mode of the HT - Lh specimens compared to the LT - Lh specimens. This is reflected in the faster decrease in flexural stress level during the flexural tests. A similar but smaller trend was seen between HT - Hh and LT - Hh, but the layer thickness seems the predominant factor for the Hh specimens.

Already, analysis of the failure mode would imply that the larger spread-out of the matrix material which is achieved by using a smaller layer thickness, ensures a much better adhesion between the layers and prevents the composite parts from delamination. On the other hand, the used nozzle temperatures do not seem to have an equally large effect on this difference in failure mode, even though they do make the results more diffuse. Larger nozzle temperatures with the 'poor' Hh parts seem to mitigate the full delamination mode, allowing for some cracking instead.

4.3.4.2 General observations

In general, some flexural curves (Figure 4.5) have a low-sloped onset. This is attributed to the evening out of surface roughness by the indenter roll during approach to the specimen, as discussed earlier. Therefore, modulus values are calculated as segment values in the clearly linear section and not via an 'automatic' calculation.

All curves have a clear linear section, leading up to a maximum between 2 and 3 % strain. In some curves, a small localized shoulder peak can be observed prior to reaching the maximum stress σ_{flex}. This is attributed to either a localized microcrack, the breakage of individual fibres or a partial delamination.

After σ_{flex} (which occurs at strain ε_{flex}), all samples undergo a sharp drop: these represent either the cracking of one of the layers or a significant delamination between layers. There is a stepwise decrease in stress levels afterwards, in accordance with further cracking and/or delamination.

The flexural properties are summarized in Table 4.5. These calculations average all results and do not discriminate between cracked and delaminated specimens, which may lead to quite to variation for some values (reported as mean value ± standard deviation). Indeed, standard deviations are significantly higher for the Hh specimens, which mostly delaminated. These same properties are visualised in the box and whisker plots in Figures 4.6 to 4.8.

When comparing the flexural properties to existing research with prepreg based endless fibre AM (Table 1.1), a fair comparison can be made with the results of Goh et al. [3]. They produced a 35 vol% glass fibre - PA6 composite and obtained a flexural modulus of 14.7 GPa and a flexural strength of 149 MPa. Even the worst Lh sample outperformed the flexural strength as measured by Goh et al., however they measured a slightly higher flexural modulus. These differences might be caused by both differences in materials used or in the production process. No other current research researched flexural properties of a similar composite material.

Table 4.5: Flexural properties of the four produced EFAM samples.

	$LT-Lh$	$HT-Lh$	$LT-Hh$	$HT-Hh$
E_{flex} [MPa]	12544 ± 981	12653 ± 2171	9153 ± 1571	9706 ± 2726
σ_{flex} [MPa]	271 ± 34	264 ± 29	159 ± 32	172 ± 38
ε_{flex} [%]	3.0 ± 0.2	2.9 ± 0.1	2.4 ± 0.5	2.6 ± 0.6

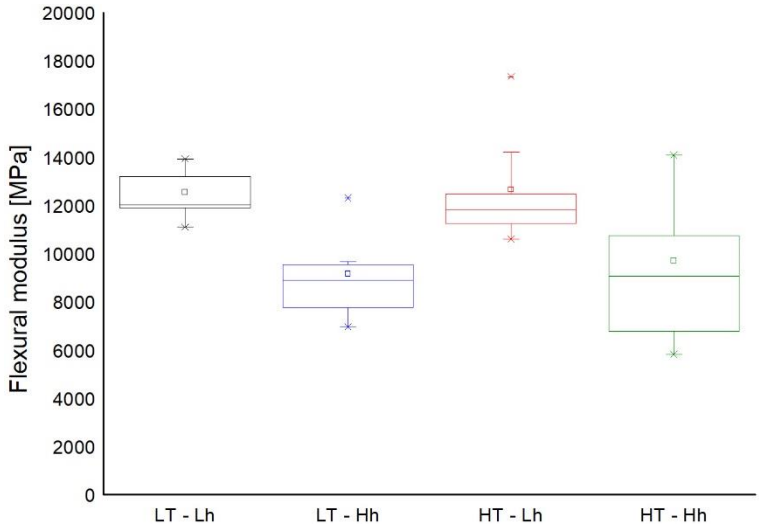

Figure 4.6: Flexural modulus of the four produced EFAM samples, box and whisker plot.

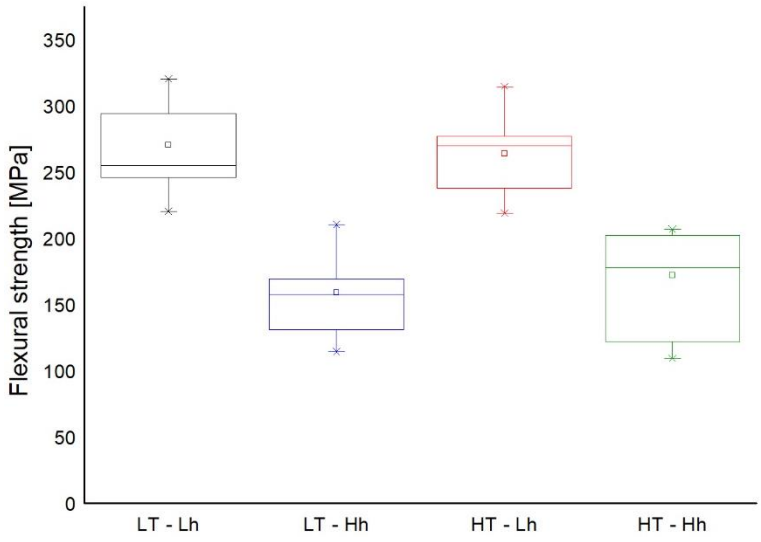

Figure 4.7: Flexural strength of the four produced EFAM samples, box and whisker plot.

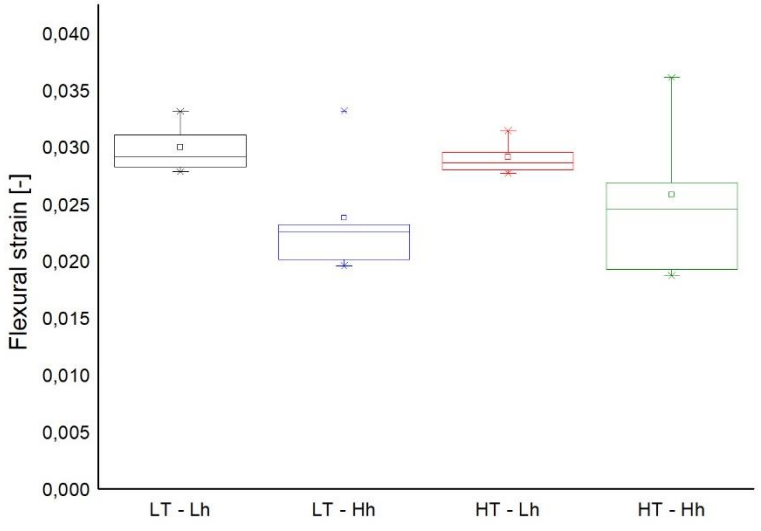

Figure 4.8: Flexural strain of the four produced EFAM samples, box and whisker plot.

4.3.4.3 Influence of layer thickness h

The layer thickness h has a significant effect on the mechanical deformation behaviour of the composites. Reduced h leads to a significantly higher stiffness and

strength, as well as higher strain-at-maximum ε_{flex} (Table 4.5), indicating that matrix and fibre can better deform in isostrain condition (i.e. acting as a solid composite with a proper fibre-matrix adhesion), thus reaching both higher strength and higher elastic deformability. Two-way variance analyses were performed to consolidate these claims, results are shown in Annex 5.3 to 5.5.

As the comparison of sample mass has shown, this cannot be attributed to densification of the composite, all samples had similar mass. Likewise, DSC analysis of the material in the interface between two deposited layers was conducted to check the crystallinity levels of the matrix and these also were alike for all samples (cf. Appendix 7). Therefore, the effect of the reduced h must be in the compressing and spreading of the polymer material and the increased overlay which is realised between layer by effectively pressing the semi-molten material of different layers into one another, as well as onto the fibres. All of this results in a composite wherein all layers contribute to the load bearing, as evidenced by the fact that the Lh samples fail in a crack mode, while the Hh samples fail in a delamination mode.

Selecting an optimal h value thus allows us to compensate for the additive build-up of the part and mitigates the weakness induced by such a layered construction, typically prone to delamination.

4.3.4.4 Influence of nozzle temperature T

Based on the results in Table 4.5, nozzle temperature only seems to be of a secondary relevance, if at all. From visual interpretation of the curves (Figure 4.5), it would seem that – within a series of the same h – higher T is able to increase strength and stiffness levels, but statistical analysis shows that variations are too large for these to be statistically relevant. With higher T, the polymer matrix would be expected to flow better, which would result in a spontaneous spreading of the material, otherwise achieved by reducing h. However, further experiments would be required to provide the accuracy of these observations. DSC analysis of the material in the interface between two deposited layers was conducted to check the crystallinity levels of the matrix and these also, were alike for all samples (cf. Appendix 7), so no further conclusions can be drawn. Two-way variance analyses were performed to consolidate these claims, results are shown in Annex 5.3 to 5.5.

4.3.4.5 Influence of h and T interactions

From the two-way variance analyses results, shown in Annex 5.3 to 5.5, can be concluded that no significant combined effects of changing h and T occur during the EFAM process.

4.4 CONCLUSIONS

During the analysis of the fracture mechanisms in different samples, it became clear that the Lh specimens tend to fail in full crack mode, whereas the Hh specimens tend to fail in full delamination mode.

The layer thickness h has a significant effect on the mechanical deformation behaviour of the composites. A reduced h leads to a significantly higher stiffness and strength, as well as higher strain-at-maximum ε_{flex}, indicating that the matrix and fibre can better deform in isostrain condition, i.e. the condition with adequate intra-layer, inter-layer and matrix-fibre adhesion, thus reaching both higher strength and higher elastic deformability. This result corresponds with the fracture mechanisms analysis. The strengthening and stiffening effect of the reduced h must be attributed to the increased compressing and spreading of the polymer material and the increased overlay, realised between layer by effectively pressing the semi-molten material of different layers into one another, as well as onto the fibres. All of this results are supported by the fact that the Lh samples fail in a crack mode, whereas the Hh samples fail in a delamination mode. Choosing an optimal h value thus allows us to compensate for the additive build-up of the part and mitigates the weakness induced by such a layered construction.

No significant effect on the flexural properties of the composite can be attributed to tested change in nozzle temperature. However, from the failure mechanism analysis, one can deduce that printing at a higher temperature can shift a delamination failure mode towards a cracking failure mode. Also the steeper decrease in flexural stress level for the HT samples supports this assumption.

Finally, no significant combined effects of changing the nozzle temperature and layer thickness on the flexural properties were observed.

4.5 REFERENCES

[1] X. Sun and B. D. Davidson, "Numerical evaluation of the effects of friction and geometric nonlinearities on the energy release rate in three- and four-point bend end-notched flexure tests," *Eng. Fract. Mech.*, vol. 73, no. 10, pp. 1343–1361, 2006.

[2] B. D. Davidson, X. Sun, and A. J. Vinciquerra, "Influences of friction, geometric nonlinearities, and fixture compliance on experimentally observed toughnesses from three and four-point bend end-notched flexure tests," *J. Compos. Mater.*, vol. 41, no. 10, pp. 1177–1196, 2007.

[3] G. D. Goh *et al.*, "Characterization of mechanical properties and fracture mode of additively manufactured carbon fiber and glass fiber reinforced thermoplastics," *Mater. Des.*, vol. 137, pp. 79–89, 2018.

5 CONCLUSIONS AND OUTLOOK

5.1 CONCLUSIONS

The main purpose of this research was the development of an automated process for producing three-dimensional composite parts, existing of a thermoplastic matrix material, reinforced with endless fibres. This process, called Endless Fibre Additive Manufacturing (EFAM), can be seen as a series of three distinctive sub-processes. The first stage consists of the impregnation of an endless fibre bundle with a thermoplastic polymer in the liquid phase. The second stage pulls the newly formed composite strand through the wipe-off die of the impregnation stage and feeds it to the third and final stage: a heated deposition nozzle, which liquifies the matrix material within the composite strand and deposits it in an additive manufacturing (AM) process, laying-up the composite selectively and layer-by-layer into a three dimensional object.

Chapter 2 assessed the impregnation quality of composite materials produced with three different melt impregnation techniques. Therefore, three material samples were produced. A first material was produced using a standard pultrusion process 'Pultrusion'. A second material was processed using a passive impregnation pin technique 'PassivePin' and a third material using the in-house developed active impregnation pin technique 'ActivePin', which injects liquid polymer between a fibre bundle and a cylindrical friction surface to enhance the impregnation quality. There was aimed at a fibre volume fraction V_f of around 50 vol%. The matrix mass fractions M_m of the three different composite samples were determined as an estimator for degree of impregnation. Process 'Pultrusion' resulted in a M_m of 0.217 ± 0.0255 g/g, 'PassivePin' in 0.269 ± 0.0241 g/g and the 'ActivePin' process in 0.285 ± 0.0241 g/g, where the theoretical maximum value for M_m was 0.291 g/g. It was concluded that both the PassivePin and ActivePin techniques perform significantly better than the Pultrusion technique. Also, the ActivePin process outperformed PassivePin in impregnation degree. Further, a stochastic method for quantifying the fibre distribution and dispersion during optical microscopy was proposed. When the findings of the morphology and fracture analyses were compared, it was clear that

all results of each analysis supported the conclusions made. Pultrusion material had an overall poor impregnation degree and fibre distribution and dispersion, the specimens lacked mechanical strength and showed fibre pull-out due to the excessive axial voids in the matrix. PassivePin material showed a higher impregnation degree and a better fibre distribution, which resulted in less voids in the matrix and a limited fibre pull-out. Finally, the ActivePin material scored significantly higher in impregnation degree and showed an excellent fibre distribution. As a consequence, very limited voids were observed and an even fracture surface without fibre pull-out was obtained. **It is concluded that the ActivePin technique fulfilled main challenge i), as described in Section 1.6, enabling the production of a composite strand, having a fibre volume fraction of at least 40 vol% and having a decent fibre distribution and dispersion within the matrix.** Through the course of this study, there was a strong focus on the ActivePin technique due to its decent performance.

In Chapter 3, the process parameters to successfully deposit a composite object were determined. A fully automated impregnation device was mounted on an AM platform to be able to perform automated lay-up of thermoplastic composite material. This chapter discussed the main characteristics of this platform and all necessary conditions of both hard- and software to successfully perform the second stage, i.e. to pull the composite through the first stage, to push it through the heated nozzle and to deposit it during the third stage. Important technical difficulties which were encountered during the process development during this research were documented. Solutions and possible ways for process optimisation were proposed, and in different cases also implemented and tested. **It is concluded that challenge ii), as described in Section 1.6, being able to successfully process and deposit a composite strand in a fully automated AM process, is met.**

The goal of the deposition tests was to verify the 'printability' of a 40 vol% glass fibre – PA12 unidirectional composite. **By the successful and consistent printing of several triple layer test specimens, it was proven that the adhesion of the composite strands on the build platform was adequate and that the cohesion between the different printed tracks and layers was sufficient to make a specimen behave as one. It can be concluded that main challenge iii), mentioned in Section 1.6, is met.** By fine-tuning processing parameters such as layer thickness and path width, the void

fraction in the composite material could be reduced to a minimum. An optical microscopy study showed the effects of the processing parameters on the composite's morphology and the similarities and differences of the morphology of an EFAM produced composite compared to a theoretical composite with a perfectly homogeneous fibre distribution and dispersion. The influence of the deposition stage on the fibre distribution and dispersion was mapped using the developed stochastic model for fibre distribution and dispersion.

Chapter 4 tested the effect of processing parameters such as the nozzle temperature, layer thickness and path width on the flexural properties of the resulting composite. It was found that sample production with a 0.6 mm layer thickness resulted in a higher flexural modulus, strain at yield and strength and a more consistent failure behaviour than production with a 0.7 mm layer thickness and an identical material density. The effect of a nozzle temperature increase from 225°C to 235°C was found to be insignificant on the flexural modulus, strain at yield and strength, but played an important role in the specimens' failure modes. Deposition at a higher nozzle temperature shifted the predominant failure mechanism from pure delamination by interlaminar shear, towards a complete break of the specimen. There were no significant interactional effects of simultaneous changes in layer thickness and nozzle temperature.

In summary, it can be said that this research succeeded in producing unidirectional, endless fibre reinforced thermoplastic composite objects, starting from a dry fibre bundle and thermoplastic polymer in pellet form. The obtained material properties were repeatable and the resulting EFAM composites proved to be having a high strength and modulus, however, their failure mechanisms proved to be different from conventionally produced composites. Techniques to mitigate or eliminate these differences were proposed but these differences should not necessarily be regarded as a disadvantage. Even more, these new properties could lead to a range of new applications (e.g. in health-care, sports, transportation, applications for controlled energy absorption and deformation through crumple zones) and are an interesting base for further research.

5.2 OUTLOOK

In future research, an optimisation of the complete EFAM process could be performed. This includes testing the influence of nozzle temperature, build platform and build chamber temperature and the use of infrared radiant heaters on the prevalence of warping effects. Other than a stiffness and strength study, as performed in Chapter 4 of this work, a thorough analysis of the interlaminar toughness of the EFAM material would be beneficial. The use of ultrasound [1] and microwaves [2] also shows potential in further improvement of the produced composite material. Also, it would be interesting to study whether the findings of this research can be extrapolated to other fibre and matrix materials. Further, it has to be tested whether above findings also correspond with the mechanical properties of other additively manufactured continuous fibre reinforced materials, and how these properties relate to the ones of conventionally produced thermoplastic composites.

Topology optimisation, as performed by for example Brooks et al. [3], Li et al. [4], Zhang et al. [5] and Dickson et al. [6] enables the tailoring of the produced composites' strength and stiffness of the part within a single deposited layer. Within this research, the focus was on 2.5D deposition of the composite material. However, the adaptation of the EFAM technology to full 3D deposition could improve the industrial relevance of the technique, enabling full strength and stiffness tailoring of the produced composite objects. This adaptation to full 3D deposition could be made by means of robotic arms or 5-axis systems (Figure 5.1) with an EFAM deposition head mounted as its end effector. This full 3D approach is currently being used in the industry-adopted ATL and AFP techniques [7] and by Eichenhofer [8] and Liu [9], who produced lattice structures for light-weight structures.

Finally, the ability of deposition of both an endless fibre composite and the composite's pure matrix material in a separate dispensing head within the same AM platform would enable the printing of composite objects with a mere polymer shell. This outer layer is perfect to have as an 'impermeable' layer, protecting the fibres from the environment and reducing the part's surface roughness. This addition can be implemented fast and would increase the industrial applicability of the EFAM technology.

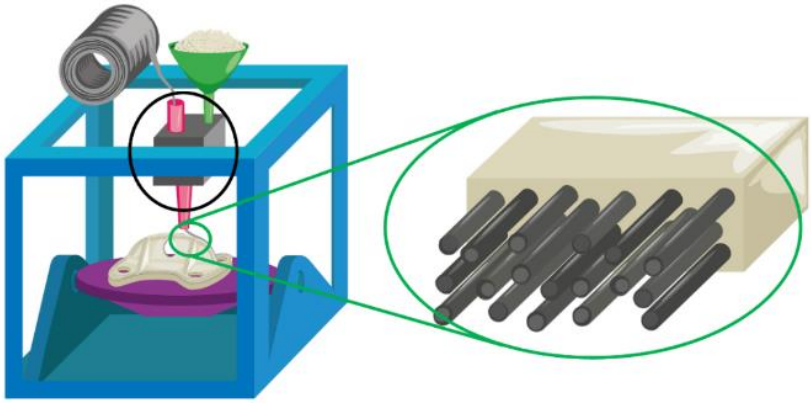

Figure 5.1: Schematic representation of a 5-axis EFAM deposition system, enabling full 3D composite lay-up.

5.3 REFERENCES

[1] J. Qiao, Y. Li, and L. Li, 'Ultrasound-assisted 3D printing of continuous fi ber-reinforced thermoplastic (FRTP) composites,' *Addit. Manuf.*, vol. 30, no. July, p. 100926, 2019.

[2] N. Li, G. Link, and J. Jelonnek, '3D microwave printing temperature control of continuous carbon fiber reinforced composites,' *Compos. Sci. Technol.*, vol. 187, no. August 2019, p. 107939, 2020.

[3] H. Brooks and S. Molony, 'Design and evaluation of additively manufactured parts with three dimensional continuous fi bre reinforcement,' *JMADE*, vol. 90, pp. 276–283, 2016.

[4] N. Li *et al.*, 'Path-designed 3D printing for topological optimized continuous carbon fibre reinforced composite structures,' *Compos. Part B*, vol. 182, no. July 2019, p. 107612, 2020.

[5] H. Zhang, D. Yang, and Y. Sheng, 'Performance-driven 3D printing of continuous curved carbon fibre reinforced polymer composites: A preliminary numerical study,' *Compos. Part B Eng.*, vol. 151, no. June, pp. 256–264, 2018.

[6] A. N. Dickson and D. P. Dowling, 'Enhancing the bearing strength of woven carbon fibre thermoplastic composites through additive manufacturing,' *Compos. Struct.*, vol. 212, no. January, pp. 381–388, 2019.

[7] H. Prüß and T. Vietor, 'Design for Fiber-Reinforced Additive Manufacturing,' *J. Mech. Des. Trans. ASME*, vol. 137, no. 11, pp. 1–7, 2015.

[8] M. Eichenhofer, J. C. H. Wong, and P. Ermanni, 'Continuous lattice fabrication of ultra-lightweight composite structures,' *Addit. Manuf.*, vol. 18, pp. 48–57, 2017.

[9] S. Liu, Y. Li, and N. Li, 'A novel free-hanging 3D printing method for continuous carbon fiber reinforced thermoplastic lattice truss core structures,' *Mater. Des.*, vol. 137, pp. 235–244, 2018.

APPENDIX

1. Relevant mechanical properties of some widespread polymers

		Young's modulus [GPa]	Yield strength [MPa]	Impact strength [kJ/m²], 23°C, notched
Thermoplastics	HDPE	0,6 - 1,1	18 - 31	6 - 84
	PP	0,8 - 1,6	19 - 36	2,5 - 25
	PA6	0,8 - 2,0	33 - 64	8 - 221
	PPS	3,2 - 3,4	64 - 67	1,3 - 2,6
	PEI	2,9 - 3,0	74 - 81	3,8 - 4,2
	PEEK	2,7 - 4,0	70 - 95	6 - 10
	PEKK	3,4 - 4,5	135 - 145	4,3 - 7,3
Thermosets	UP	2,1 - 4,4	33 - 40	1 - 48
	PF	2,8 - 4,8	28 - 50	1,3 - 2,1
	EP	1,0 - 3,1	36 - 72	1 - 26
	VE	2,9 - 3,8	63 - 95	3,3 - 17
	PUR	4,1 - 4,3	55 - 61	2
Elastomers	SBR	2.10^{-3} - 1.10^{-2}	1,4 - 3	590 - 600
	NR	1.10^{-3} - 2.10^{-3}	21 - 28	590 - 600
	IR	2.10^{-3} - 2.10^{-3}	23 - 26	590 - 600

2. Relevant mechanical properties of some widespread fibre fillers

Fibre type		Young's modulus [GPa]	Tensile strength [MPa]	Density [kg/m³]	Specific modulus [Nm/kg]	Fibre diameter [µm]
Ceramic	Al_2O_3	378	1380	3950	96	15 - 25
	B	400	2500	2500	160	100 - 200
	Basalt	70 - 110	1400 - 4900	2500 - 2900	26 - 41	7 - 22
	Carbon, High Strength (HS)	160 - 270	4400 - 4900	1800	90 - 150	7
	Carbon, Intermediate Modulus (IM)	270 - 325	5300 - 7000	1800	150 - 180	4 - 6
	Carbon, High Modulus (HM)	325 - 440	4750 - 5850	1800	180 - 240	5 - 8
	Carbon, Ultra High Modulus (UHM)	> 440	2000	1800	> 200	6,5
	E-glass	70 - 85	2000 - 3800	2540	28 - 33	1 - 25
	S-glass	86 - 93	4800	2500	35 - 37	1 - 25
	R-glass	86	4150	2500	34	1 - 25
	quartz glass	70	3700	2200	32	1 - 25
	SiC	180 - 430	2000 - 4000	2500 - 3300	70 - 130	10 - 140
	TiB_2	480	1000	4500	107	100
Metal	Al	72	400	2700	27	> 10
	B	395 - 420	2000 - 3400	2550	155 - 165	100 - 200
	Mild steel	210	450	7800	27	>= 8
	High strength steel	200	1250	7800	26	>= 8
	Stainless steel	196	800	7800	25	>= 8
	Ti	110	950	4800	23	20 – 120
Natural	Jute	13 - 60	250 - 850	1400	9 - 43	4 - 20
	Flax	25 - 100	350 - 1500	1450	19 - 70	10 - 25
Polymer	Aramide LM	60	3600	1450	40	12
	Aramide HM	120	3100	1450	80	12
	Aramide UHM	180	3400	1470	120	12
	HDPE	120	3200	970	125	40

3.1 General material data Rilsamid AMN O TLD by producer

Producer	Arkema	
Product	Rilsamid AMN O TLD – PA12	
Tensile modulus	1170 MPa	ISO 527-1/-2
Yield stress	38 MPa	ISO 527-1/-2
Yield strain	7 %	ISO 527-1/-2
Charpy notched impact strength, +23°C	9 J/m²	ISO 179

3.2 Flexural stress-strain curves of Rilsamid AMNO TLD

Measured according to ISO 178:2019.

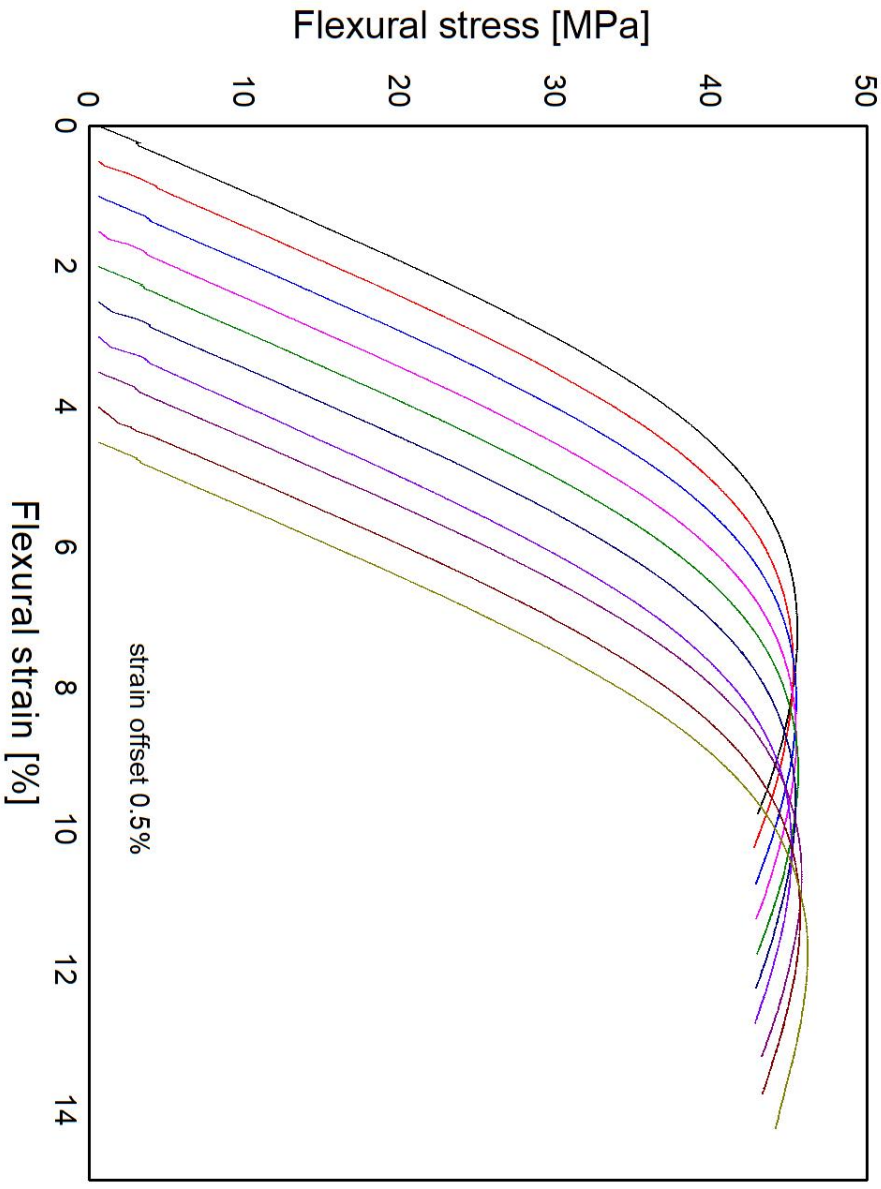

3.3 Tensile stress-strain curves of Rilsamid AMNO TLD

Measured according to ISO 527-1:2019.

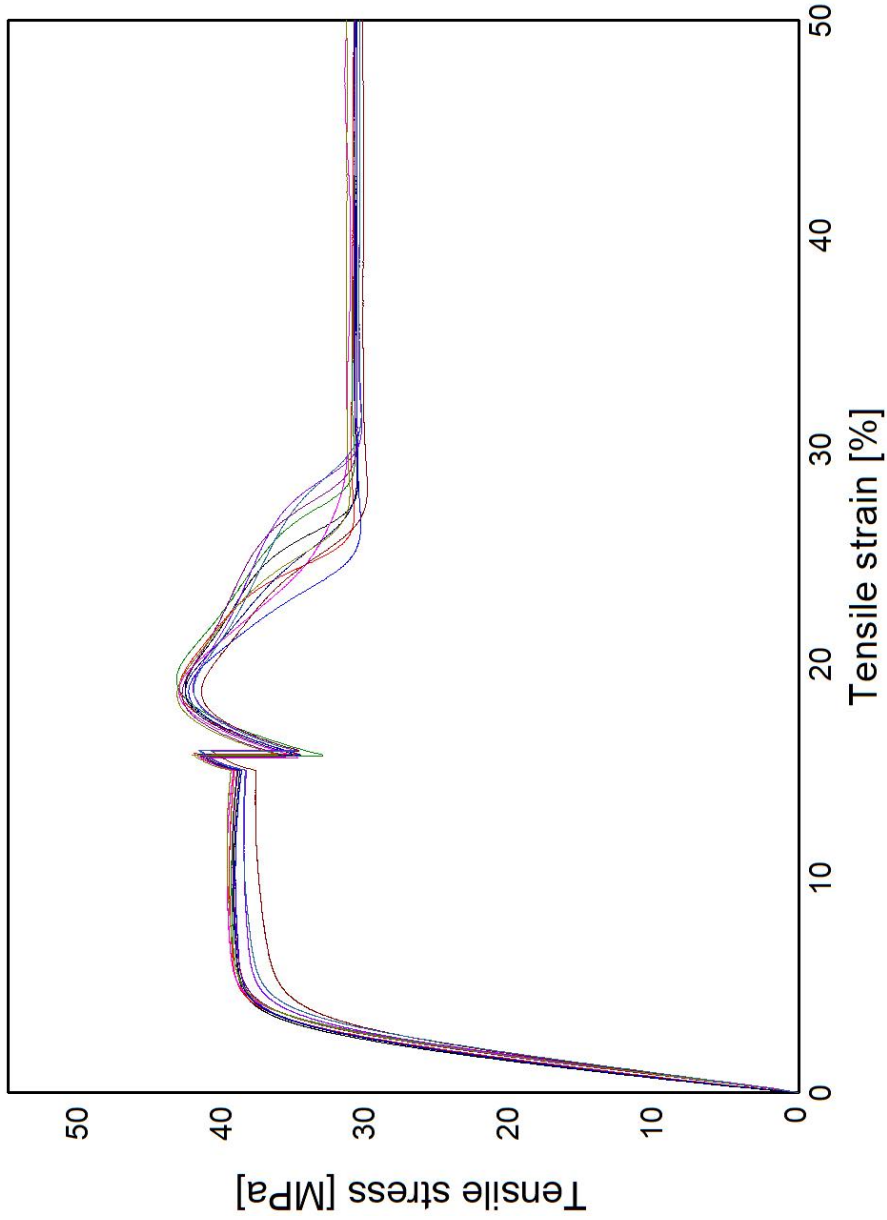

3.4 Dynamic mechanical analysis of Rilsamid AMN O TLD

Measured according to ISO 6721-11:2012, at a linear temperature increase of 1 K/min.

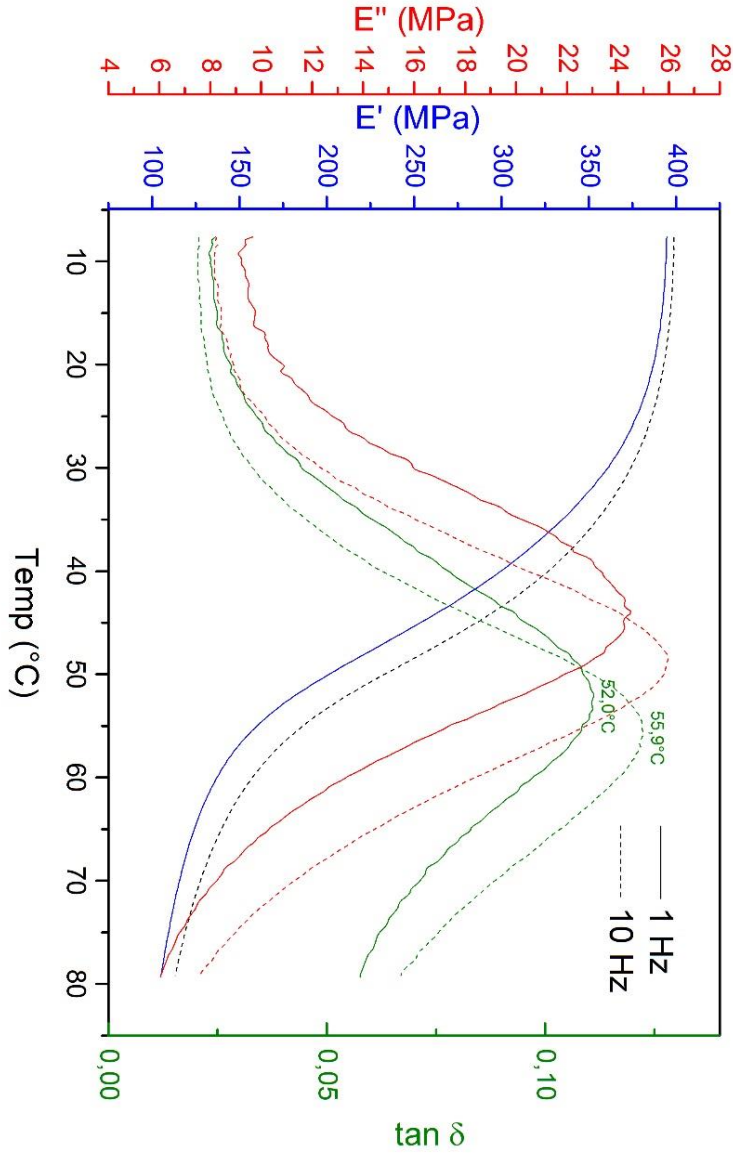

3.5 Differential scanning calorimetry analysis of Rilsamid AMN O TLD

Measured according to ISO 11357-1:2016, at a linear temperature increase of 10 K/min.

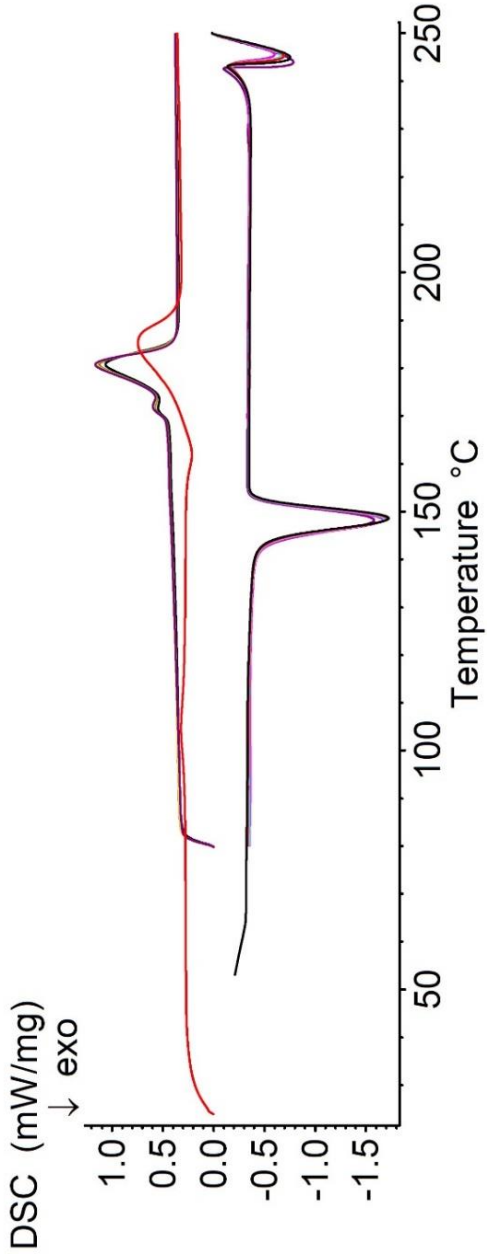

3. General material data StarRov 853 by producer

Producer	Johns Manville
Product	StarRov®LFTplus Direct Roving 853
Glass type	E
Sizing designation	853
Loss on incineration	0.50 mass%
Linear density	1200 tex
Single fibre diameter	16 µm

4. Technical drawings of AM platform

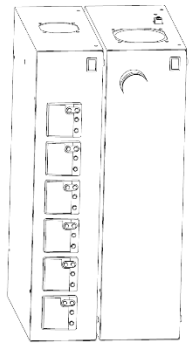

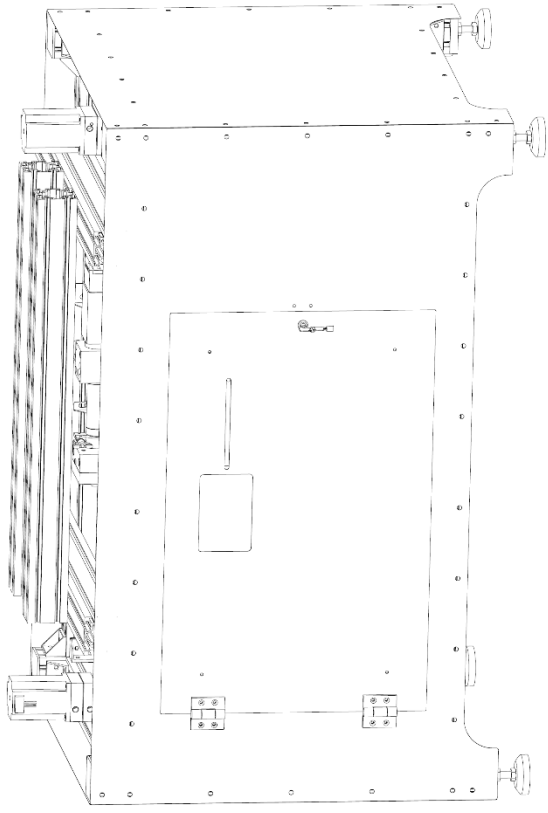

5.1 Two-way variance analysis results of the four samples' flexural specimen mass

Source of variation	SS	df	MS	F	P	F_{crit}
h	0,006069	1	0,006069	1,399251	0,254129	4,493998
T	0,014548	1	0,014548	3,353985	0,085727	4,493998
Interaction	0,01131	1	0,01131	2,607492	0,125905	4,493998
Within	0,069399	16	0,004337			

5.2 Two-way variance analysis results of the four samples' fibre volume fraction

Source of variation	SS	df	MS	F	P	F_{crit}
h	2,968673	1	2,968673	2,611913	0,144726	5,317655
T	0,521079	1	0,521079	0,458458	0,517442	5,317655
Interaction	0,339003	1	0,339003	0,298264	0,599868	5,317655
Within	9,092716	8	1,13659			

5.3 Two-way variance analysis results of the four samples' E_{flex}

Source of variation	SS	df	MS	F	P	F_{crit}
h	80354727	1	80354727	20,63396	9,68E-05	4,195972
T	877332,6	1	877332,6	0,225287	0,638722	4,195972
Interaction	393776,4	1	393776,4	0,101116	0,752854	4,195972
Within	1,09E+08	28	3894295			

5.4 Two-way variance analysis results of the four samples' σ_{flex}

Source of variation	SS	df	MS	F	P	F_{crit}
h	82784,27	1	82784,27	73,89781	2,43E-09	4,195972
T	85,78918	1	85,78918	0,07658	0,784019	4,195972
Interaction	779,8501	1	779,8501	0,696137	0,411147	4,195972
Within	31367,1	28	1120,253			

5.5 Two-way variance analysis results of the four samples' ε_{flex}

Source of variation	SS	df	MS	F	P	F_{crit}
h	0,00018	1	0,00018	11,62829	0,00199	4,195972
T	2,73E-06	1	2,73E-06	0,176588	0,677529	4,195972
Interaction	1,68E-05	1	1,68E-05	1,085197	0,306449	4,195972
Within	0,000433	28	1,54E-05			

6.1 Flexural stress – strain diagram for specimens produced at 225°C – 0.6 mm

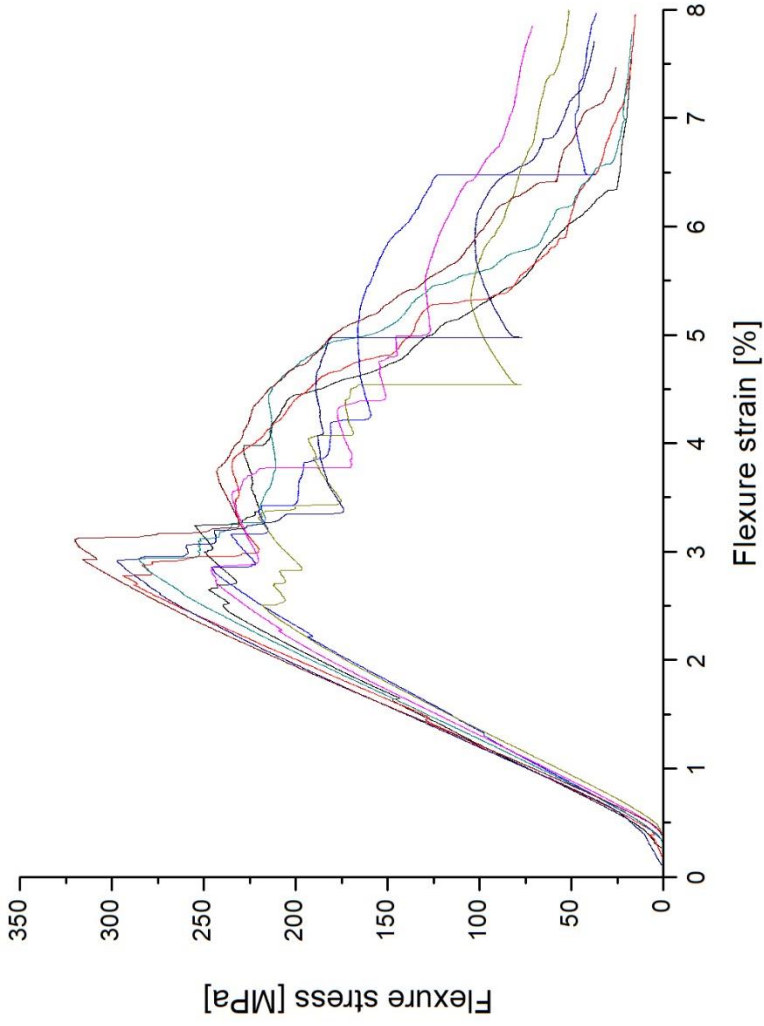

6.2 Flexural stress – strain diagram for samples produced at 225°C – 0.7 mm

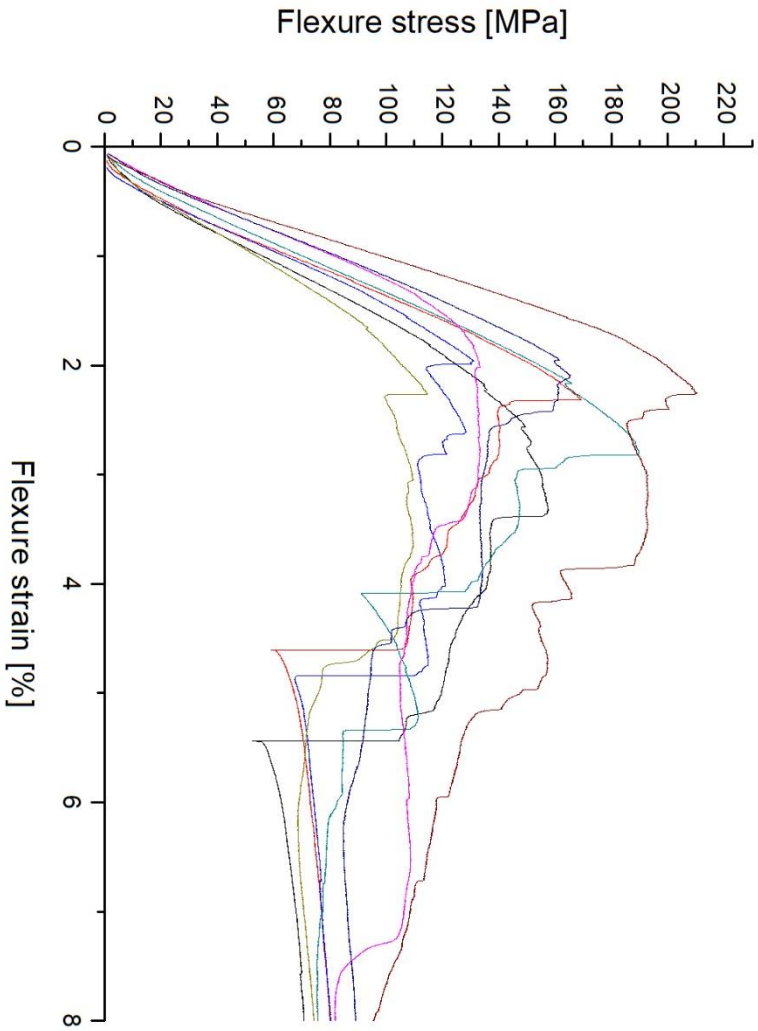

6.3 Flexural stress – strain diagram for samples produced at 235°C – 0.6 mm

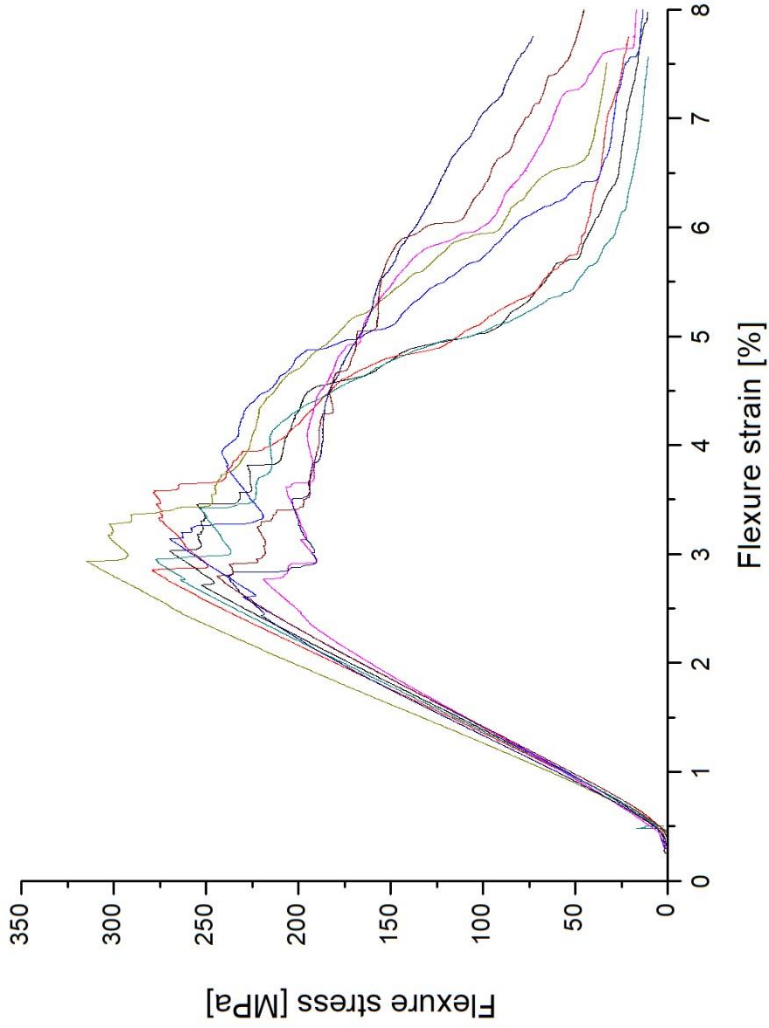

6.4 Flexural stress – strain diagram for samples produced at 235°C – 0.7 mm